Applications of Photo-Active Thin Film Semiconductors in Environmental Remediation

By
Ramsey G. Kropp

A dissertation submitted in partial fulfillment of
the requirements for the degree of

Doctor of Philosophy
(Environmental Chemistry and Technology)

at the
UNIVERSITY OF WISCONSIN-MADISON
2014

Date of final oral examination: 5 December, 2013

The dissertation is approved by the following members of the Final Oral Committee:
Marc A. Anderson, Professor, Environmental Chemistry and Technology, CEE
James J. Schauer, Professor, Environmental Chemistry and Technology, CEE
Joel Pederson, Professor, Environmental Chemistry and Technology, CEE
Mat Ginder-Vogel, Assistant Professor, Environmental Chemistry and Technology, CEE
Isabel Tejedor, Senior Scientist, Environmental Chemistry and Technology, CEE

ACKNOWLEDGEMENTS

Marc Anderson, for his advice and encouragement in achieving this goal, as well as serving as a living model of what a talented generalist can accomplish in a specialized field. Thank you for making me part of a laboratory that feels like a family, constantly giving me interesting ideas to explore, and for teaching me that ideas come from everywhere in life.

Jamie Schauer, for keeping me grounded in reality and focused on producing results instead of chasing every passing interest, as well as serving as a model of what a talented specialist can accomplish in a general world. Thank you for reminders that experiments and data are just as necessary for science as ideas, that publications matter, and that the simplest solution is usually the best.

Joel Pederson, for teaching me that all science is approximate, and that 30% error is a significant improvement over not having any idea whatsoever.

Isabel Tejedor, for advising me on instruments and methods for testing every property I could imagine. Thank you for your incredible memory and broad knowledge set. A few minutes spent in her office were worth a week spent in a book.

Steve Cramer, for supporting me through times of thin funding and thick concrete.

Ken Walz, for instruction, guidance, advice, and friendship all the way from technical college to graduate school. You have changed the trajectory of my life more than you could know.

Jennifer Jackowski, Jesse Wouters, Rachel Moss, Kevin Leonard, the twins San Fillipo, and all of the other graduate students and lab mates of the Environmental Chemistry and Technology Program. Without such interesting and pleasant peers the long slog through classes, securing funding, research, writing, and presenting might have seemed like work.

The faculty and staff of the Water Chemistry program, the faculty, students, and staff of the Civil and Environmental Engineering department and the Structural Materials program,

the faculty, students, and staff of the Materials Science program and Chemical Engineering program

Dean Tompkins, for giving me the confidence to try to tackle any problem, even if I had no idea what I was doing. For a degree focused on chemistry I learned an awful lot of practical electronics, computer programming, fluid dynamics, mechanical design, machining, systems integration, thermodynamics, fabrication, materials selection, parts sourcing, contractor interaction, and instrumentation. I wish more of our collaborations panned out.

The teachers in my life, for giving me the gift of a love of learning, even when it seemed like I didn't care about the knowledge you provided.

ASHRAE, the Wisconsin Department of Transportation, the Wisconsin Concrete Pavement Association, AquaMost, Desiccant Rotors International, and Triatomic UV for funding and supporting me through my research.

My parents, for their unflagging love and patience. My mother taught me to: read, write, design and craft jewelry, provide emergency veterinary care, operate a computer, ride and train horses, and raise a child. My mother is the most educated woman I know, even if there is no diploma to prove it, and any autodidacity I possess I owe to her. She taught me to look at the world as a series of problems to solve, and gave me the tools to figure out how to work on them. My father taught me how to raise a barn, fix a truck, drive a manual, walk proud, dress a deer, wire a switch, track an animal, enjoy solitude, and adapt to any environment. He taught me what a man should be, and showed me what a man can be. Our years together might not have always been perfect, but I would take interesting over perfect a thousand to one.

My wife Patricia, for more than a decade of love, patience, and support. Thick and thin, easy and hard, in the same room or across continents, we have been together. Thank you for keeping me focused and motivated, your patience when I was tired and frustrated, for keeping our home when I was away, and for the comfort and warmth your presence has always provided. You are as responsible for this degree as I am, and I appreciate everything you do.

To my children Rowan and Linaya, I hope I can provide the life of adventure, adversity overcome, wonderment, magic, love, and delight that you deserve. The thought of your future was the strength I needed to finish this degree. Thank you for being

TABLE OF CONTENTS

ABSTRACT:

This dissertation presents an overview of the current theoretical and experimental understanding of the photophysical, photochemical, and photoelectrochemical behavior of photoactive thin film materials and a survey of their current application as well as the results of several experimental studies of photo-active semiconductor thin film materials in environmentally relevant applications: oxidation of ammonia to nitrogen gas by photoelectrocatalysis, the oxidation of low concentration volatile organic compounds from indoor air, and an inorganic photocatalytic curing compound for use on concrete. Finally, there is a section devoted to detection of gas phase organic contaminants by chemical ionization mass spectrometry, including a brief description of the instrument employed for a portion of this research.

SECTION 1: INTRODUCTION

1. PHOTOCATALYZED HETEROGENEOUS CHEMISTRY

Increasing global competition for energy resources, regulatory limits on industrial emissions, and increasing public pressure have ignited demand for alternative chemical reaction technology. There is currently a great deal of interest among researchers and industry regarding the study and

application of heterogeneously photocatalyzed chemical reactions: those reactions in which an adsorbed species is chemically changed by a photoactivated catalyst surface. The catalyst material absorbs energy either from direct illumination or from an excited adsorbed molecule and transfers that energy into the reacting species or solvent molecule. This transferred energy results in oxidative or reductive reactions that can be utilized in several processes: i.e. hydrogen production, artificial photosynthesis, oxidative deactivation of microbes, oxidative conversion or mineralization of aqueous organic or mineral contamination, oxidative conversion or mineralization of organic or mineral contamination in air, reductive conversion or removal of metal ions in aqueous systems, and chemical synthesis.

These reactions can all be accomplished absent photocatalysis; the need for illumination of the catalyst surface dramatically increases the difficulty of reactor design, reactor cost, and implementation complexity. The reactor must be designed with provisions for illumination of the catalyst surface, materials are required which are transparent to and unaffected by the wavelengths necessary to activate the catalyst. Isolation of chemical reactions to only the illuminated catalyst surface decreases reactor volumetric efficiency. Photocatalytic reactions are typically slower than thermally catalyzed heterogeneous reactions, which also serves to increase the necessary reactor volume to achieve sufficient residence time for complete conversion. An

additional difficulty in commercial implementation of photocatalysis is the potential high cost or availability of light sources with suitable wavelengths and sufficient intensities.

Given an appropriate reactor design there is still a need to optimize catalyst systems to ensure high quantum (per photon) efficiency, high selectivity, and rapid kinetics. Intelligent catalyst design requires a fundamental understanding of how semiconductor properties: i.e. crystal structure, size, and orientation; doping; surface functionalization; and interactions with the catalyst support affect reaction parameters; an understanding which is still incomplete. Informed reactor design also requires a detailed knowledge of the chemical mechanisms and reaction rates involved: these mechanisms are still being investigated and remain uncertain, particularly in complex natural systems. Reaction mechanisms vary with the properties of the catalyst and reactants, but also reactant concentrations and environmental parameters like humidity, temperature, illumination intensity and wavelength, and solvents as well as competing solutes present. Published reaction mechanisms should only be considered valid in a narrow environmental window: reactors that yield identical final products may utilize entirely different mechanisms depending on the conditions within the reactor.[1–10] Commercial and industrial adoption of photocatalytic processes has been limited largely due to the difficulty in fully characterizing such a complex system for kinetic analysis and by-product formation.[11]

Cognizant of these limitations, the effort being expended in pursuit of fundamental mechanistic research, catalyst improvement, and successful commercial implementation of devices harnessing this phenomenon appears somewhat quixotic. Irrespective of difficulties in design and implementation, research efforts continue and commercial sales continue to grow. Several compelling features recommend heterogeneous photocatalysis over other methods for environmental remediation. Perhaps the most compelling is the ability to harness solar radiation for chemistry that otherwise requires thermal, electrical, or chemical energy inputs. Reactions that require potentially harmful reactants, extreme reacting conditions, expensive or toxic catalysts are readily performed with simple illumination by a suitable light source.[12–21]

Given correct reacting conditions, photocatalysis is capable of direct conversion of solar energy into chemical energy. Honda and Fujishima's initial discovery of the photocatalytic effect of generating hydrogen gas at the surface of an illuminated electrode surface by splitting water, and the conversion of solar energy directly into chemical energy remains one of the most active areas of research in photocatalysis.[22] Hydrogen generated by photocatalytic processes can be used in fuel cells, internal combustion engines, or as chemical feedstocks.[23–27] Carbon dioxide can be transformed into methanol and similar simple molecules photocatalytically under reducing conditions, a process chemically analogous to photosynthesis. Solar energy can therefore be stored as carbon neutral liquid or solid fuels, a format with greater energy and power density than

thermal or electrical storage that is easily integrated with current infrastructure. Photocatalysis under reducing conditions is under investigation for chemical synthesis or modification: i.e. dehydrogenation, polymerization, dehydration, and carbon chain extension.[19,20,28] Well controlled sub-stoichiometric oxidative conditions prevent complete oxidation for the production of alcohols, aldehydes, ketones, carboxylates, and epoxides.

Photocatalysis is also widely researched for use in disinfecting water, air, and surfaces. The antimicrobial effects of directly applying ultraviolet (UV) light are well known and widely employed but face several shortcomings. Inactivation occurs due to penetration of high-energy photons leading to damage of microbial genetic structures. This requires significant exposure to short wavelength ultraviolet light, especially for hardened spores and dirty surfaces.[29–31] Solar radiation is largely deficient in antimicrobial wavelengths due to atmospheric absorption and entirely unavailable in many indoor settings.[32,33] Light with sufficiently short wavelengths and high intensities are hazardous to macrobiota as well as microbes. UV emitters require safety interlocks and other exposure controls to protect occupants from radiation burns, increased risk of skin cancer, and eye injury.[29] Low cost germicidal UV emitters typically employ unfiltered emission from low-pressure mercury vapor fluorescent lamps which, along with traditional fluorescent lighting in which a phosphor is used to shift UV wavelengths into the visible spectrum, constitute a large, disperse reservoir of mercury in the environment.[34,35]

Photocatalytic inactivation of microbes occurs via different, primarily radical mediated, oxidative mechanisms that can be initiated by low energy UV or even visible light. This lower energy light has significantly fewer exposure hazards and can largely eliminate the need for mercury vapor emitters.[36–42] Solid-state lighting products that emit in the near-UV region offer significant gains in efficiency and emitter life and are already widely available. The use of doped photocatalyst surfaces with band gaps in the visible light spectrum admits the possibility of continuously self-disinfecting surfaces, which can increase occupancy factors as disinfection will no longer require a space to be vacated and protected by personnel protecting interlock devices.

Photocatalytic oxidation is capable of degrading chemical species that are highly resistant to alternative remediation treatments. Interactions between photogenerated charge carriers and molecular oxygen or water result in the formation of powerful oxidative radicals. Many of these radicals possess greater oxidative power than fluorine or chlorine and have application in the treatment of organic and elemental metallic contamination in air and water systems. The high oxidative power of the generated oxidative radicals allows for treatment of even highly halogenated environmentally persistent species, including fluoro- and chlorofluorocarbon species. These reactions result in complete mineralization or oxidation given sufficient contact time.[2,43–46]

Volumetric conversion rates are typical low in photocatalytic reactors but photocatalysis and photoelectrocatalysis have applications even in highly contaminated solutions and low reactor

residence times when complete conversion is not required: i.e. viscosity modification of polymer solutions, bleaching of textile dye, deactivation of pesticides, herbicides, and chemical weapons, or photoelectrocoagulation.[47–59] In addition to the more widely employed oxidative photocatalytic reactions, reductive photocatalytic chemistry also has application in environmental remediation and industrial chemistry. Heavy metal ions present in contaminated water can be reduced upon reaction with a photogenerated electron, decreasing toxicity.[60,61]

Modification of the chemical and physical structure of the photocatalyst surface can provide improved selectivity in chemical reactions,[16,18–20,28,62,63] allow for the use of longer wavelength light,[63–68] and increase efficiency.[69,70] Catalyst materials can be employed in a number of reactor designs and in many forms. Reactors that employ finely divided or powdered catalyst provide maximum surface area and contact time with the mobile phase but separation of the solid catalyst from the treated or product stream presents significant technical challenges. A monolithic catalyst is dimensionally stable and immobile, but is difficult to fabricate and provides moderate surface area. When applied as a membrane on a substrate photocatalysts can be immobilized in a reactor or easily separated from product streams, with highly porous membranes providing significantly more surface area than dense films.

1.1. SEMICONDUCTOR-PHOTON INTERACTIONS

A photon of sufficient energy can impart that energy to an electron to promote that electron from the valence band to the conduction band of the semiconductor. An electron in the conduction band is highly mobile and will migrate through the semiconductor due to random thermal motion or in response to an applied electromagnetic field. Motion of the negatively-charged electron results in an imbalance of charge: the small region of positive charge remaining can be conceptually treated as the creation of a second mobile charge carrier, a quasi-particle with positive charge equal to the magnitude of the charge on the electron, commonly referred to as a "hole". These mobile charges possess opposing charge and at low thermal energies electrostatic attraction binds them into an exciton: a short lived, mobile, weakly bound electron/hole pair capable of carrying energy without net charge transfer.[71,71–77] The excitonic state is short lived in the presence of an applied voltage field or at environmentally relevant thermal energies. At normal environmental temperatures the thermal energy of the semiconductor dramatically exceeds the binding energy of the exciton and the electron/hole pair dissociates with the electron and hole migrating independently.

Disassociated electrons and holes are mobile and interact with other charge carriers, bulk crystal defects, surface crystal defects, dopants, inter-crystalline interfaces, or adsorbed species at the crystal surface.[71,75,78–81] When an electron and hole recombine (more correctly, the electron returns to the valence band and charge balance is restored) the energy (equal to the band gap) is

emitted (i.e. photon emission) or converted to thermal energy. In the semiconductor, bulk charge carriers can become trapped at crystal dislocations or heteroatoms from doping and material impurity. Charge carriers that travel to a semiconductor grain boundary can become trapped at surface defects, transfer to an interfacing crystal, or interact with an adsorbed species. Heterogeneous catalysis occurs at exposed interfaces and involves interaction of a photogenerated charge carrier with an adsorbed species. Therefore, any interaction that results in either recombination or bulk trapping decreases the quantum (per photon) efficiency of the system.[66,67,82] Electrons or holes that interact with an adsorbed species result in reduction or oxidation, respectively. These reactions can be used for direct synthesis, modification, or decomposition of adsorbed species or to generate radicals for subsequent reaction (Figure 1).[44]

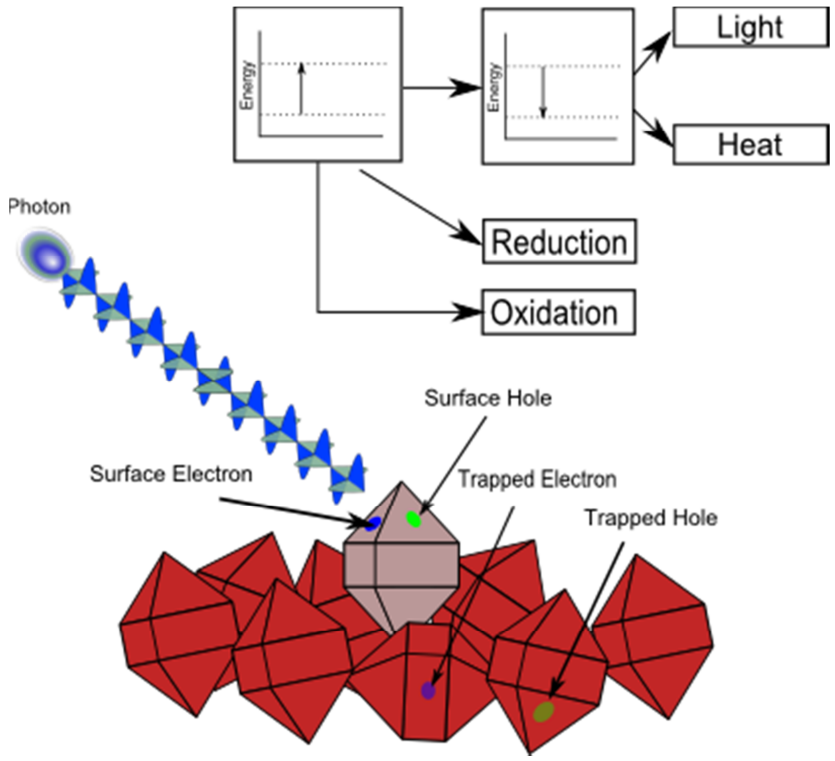

Figure 1: Photoexcitation, recombination, and charge carrier migration in semiconductor crystal

1.2. Oxidative Photocatalytic Chemistry

Electrons or holes at the catalyst surface can react with any adsorbed species, resulting in the formation of charged species or radicals. Both reductive and oxidative reactions occur and result in the formation of powerful reactive species. Holes that react with water or molecular oxygen result in the formation of several reactive oxygen species, primarily the hydroxyl radical. Systems in which the hydroxyl radical is the primary oxidizing species are similar to those utilizing the Fenton or photo-Fenton chemistries.[83] A generalized reaction scheme highlighting the similarities is presented in Equation 1:

Equation 1: Generalized Photocatalytic and Fenton chemistry overview. Only the mechanism by which the iron is reduced differs between the Fenton and photo-Fenton reactions.

Radical Mediated Photocatalytic Oxidation

$$TiO_2 + h\nu \rightarrow h^+ + e^-$$

$$h^+ + OH^- \rightarrow OH\cdot$$

$$e^- + O_2 \rightarrow O_2^-$$

Fenton Chemistry (Low pH)

$$H_2O_2 + Fe^{2+} \rightarrow Fe(OH)^{2+} + OH\cdot$$

$$Fe^{3+} + H_2O_2 \rightarrow Fe^{2+} + OOH\cdot + H+$$

Photo- and Electro-Fenton Chemistry

$$H_2O_2 + Fe^{2+} \rightarrow Fe(OH)^{2+} + OH\cdot$$

$$Fe(OH)^{2+} + h\nu \rightarrow Fe^{2+} + OH\cdot \quad \text{Photo-Fenton}$$

$$Fe^{3+} + e^- \rightarrow Fe^{2+} \quad \text{Electro-Fenton}$$

These radicals are powerful oxidizers and are of potential use in removal or deactivation of organic or biological contaminants from liquid or gas phases. They are also capable of preventing adherence of solid contaminants to a treated surface provided that the contaminants permit

sufficient irradiance to activate the catalyst (e.g. self-cleaning glass). Oxidation can be either partial or complete depending on the contaminant of interest, reactor conditions, and reactor residence time. The fate of reaction by-products depends on the properties of the by-product, the physicochemical conditions of the catalyst interface, and the presence of other species. By-products with low surface affinity desorb from the surface and reenter the fluid phase. If the reactor is of a batch configuration or the space-time within the reactor is sufficiently large the by-product may subsequently mineralize completely while undersized reactors can emit the by=products in the treated stream. By-products with large surface affinity or unfavorable reaction kinetics occupy adsorption sites and block competing species, serving to poison the catalyst. Complete mineralization of large compounds progresses through multiple reaction pathways involving multiple intermediate conversion products.[2]

Photocatalytic oxidation is being investigated for the inactivation or removal of contaminants resistant to other treatment methods. The high oxidizing potential of the holes and other reactive species formed at the photocatalyst surface results in the conversion of even highly halogenated organic compounds, such as fire retardants, refrigerants, PCBs, and propellants, that are typically resistant to other remediation techniques or biological conversion.[84–92] Personal care products (PCPs) and pharmaceuticals that are present as microcontaminants are readily deactivated or converted to less harmful forms by photocatalysis.[55,56,93,94] Photocatalytic treatment

is not confined to organic species: gaseous elemental mercury has been shown to photocatalytically oxidize to non-volatile mercury oxide even at high concentrations (1-2ppm). The extreme hydrophillicity of activated photocatalysts results in significant mercury conversion even at extremely low relative humidity (5-20ppm water vapor).[43]

Some environmental applications do not require complete oxidation for remediation. There are significant opportunities for the use of photocatalytic oxidative chemistry even in systems in which complete mineralization is impractical. Significant studies on chain scission and crosslinking in photocatalytic and photoelectrocatalytic reactions of aqueous polymers suggest that this technology is suitable for solution viscosity modification without a significant decrease in total organic carbon content.[47,95–97] Aqueous solutions with pronounced coloration due to dye loading, particularly by-products of textile and paper processing, lose their color upon treatment with oxidative photocatalytic processes; organic dye removal is often used as a probe of photocatalytic activity due to the ease of measuring concentrations colorimetrically.[52,53,57–59,98–100]

Biological deactivation by radical oxidation occurs via multiple pathways but rarely results in complete mineralization.[42] Cellular membranes can be directly damaged by contact with photoactivated surfaces while internal structures are damaged through the actions of primary (directly generated) or secondary oxidative species in the microbe. Oxidative damage can result in physical destruction, interference with metabolic processes, or inability to

regenerate.[38,101].Deactivation mechanisms will not be treated in this document other than for a brief mention that physical processes are capable of deactivating microbes in their dormant state (i.e. bacterial spores or cysts) that are typically more resilient than the active forms[36,38,39].

1.3. Reductive Photocatalytic Chemistry

The large oxidative potential of most natural systems limits the use of reductive photocatalysis for environmental remediation *in situ*. A more common application is "green chemistry", in which activated photocatalysts replace traditional reagents or extreme reactor conditions. The earliest reports of photocatalysis noted the formation of H_2 gas at the surface of an illuminated electrode in water, and hydrogen production from hydrolysis of water is still an area of primary interest to researchers. Solar radiation induced direct hydrolysis on solid-state catalysts provides a potential pathway to energy conversion other than photovoltaic, photothermal, or biological. Research on optimizing the catalyst, reactants, reactor design, and light management has dramatically improved conversion kinetics, but personal and grid scale energy conversion has not yet become practical. In addition to hydrogen production, it is possible to reduce carbon dioxide into alcohols and other species for energy storage or the production of chemical feedstocks for further processes, a process analogous to photosynthesis.[12] A key requirement for applying these reductive reactions is eliminating molecular oxygen from the system to reduce the formation of hydroxyl radicals and other oxidative species.

Given suitable reactor conditions, reductive photocatalysis allows the use of photonic energy for converting environmentally troublesome highly oxidized species to less harmful reduced forms. Wu et al report reduction of nitric oxide to nitrogen and oxygen gas in an atmosphere of He or N_2 with an inlet concentration of 100ppm NO_x using an oxygen deficient Fe doped TiO_2 catalyst.[102] Metal ions also undergo photocatalytic reduction: Chen et al report reduction of Hg^{2+} and Cu^{2+} in aqueous solutions utilizing TiO_2 catalyst and methanol as a hole scavenger,[60] while Chakrabarti et al report photoreduction of Cr^{6+} in aqueous solutions using ZnO catalyst, again with methanol as a hole scavenger.[61]

2. PHOTOCATALYTIC MATERIALS

Photocatalysis occurs on semiconductors in which the energy separation between the valence band and conduction band is similar to that of photonic energy within the infrared to ultraviolet range. Semiconductor choice, surface modification, and doping determine the band gap and therefore the necessary photon energy of the reactor system. In order for reactions to occur, the generated charge carriers must interact with reactants or solvent molecules adsorbed onto the catalyst surface. Rapid conversion requires adsorbed species to be present in appreciable quantity, either by having thermodynamically and kinetically favorable adsorption characteristics (large site density) or by increasing surface area. Adsorption occurs when the free species interacts with a site on the surface with sufficient surface energy in which to bind to the particle. Physisorption

refers to interactions resulting from weak interactions, i.e. van der Waals forces, which are readily reversible. Chemisorption refers to adsorption involving ionic or covalent interactions that strongly bind the adsorbed species. The surface energy of the catalyst material strongly affects how chemical species adsorb, but changes dramatically for illuminated photocatalysts. Normal adsorbance measurement techniques are performed under minimal or incidental ambient illumination, and the values obtained likely differ from the actual system of interest. Adsorption behavior is also influenced by changing catalyst surface functionality or morphology and environmental conditions within the reactor.

The band-gap energy of a semiconductor is an intrinsic property of the material but can be tuned by doping the material with a chromophore, either as an atomic substituent in the crystalline material or as an adsorbed species. The chromophore absorbs the lower energy photon and transfers the charge carriers into the semiconductor, as in dye-sensitized solar cells, and allows the use of light with wavelengths longer than light with the band gap energy.[75,103–105] The design and application of catalysts activated by visible light, particularly solar wavelengths, is an area of active research.[28,63,65,67,68]

Early research on photocatalysis focused on metal oxide and sulfide semiconductors. Several semiconductors have energies corresponding to light in the near UV or visible spectrum, e.g. titanium dioxide, cadmium sulfide, zinc sulfide, zinc oxide, molybdenum sulfide, tin oxide,

tungsten oxide. The photocatalyst most widely studied and currently employed is titanium dioxide, which occurs in anatase, rutile, and rarely in the brookite crystalline forms at environmentally relevant conditions. Titanium dioxide has a band-gap energy near 3.2eV, corresponding to a wavelength of *ca.* 380nm, although crystal structure and particle size affects the activation energy. Titania is favored because it is inexpensive, stable, environmentally benign, and widely available. The electron structure of titanium dioxide results in the formation of charge carriers capable of reducing protons and oxidizing water simultaneously under illumination. Generally, anatase titanium dioxide is reported to have higher photocatalytic activity than the rutile phase, but several studies have identified increased performance from rutile or biphasic materials.[106]

2.1. MIXED SEMICONDUCTOR SYSTEMS

The high band gap potential of most photocatalysts and deficiency of solar radiation in short wavelength light limits their use to reactors employing artificial illumination. Several techniques have been employed for modifying the catalyst electron structure to harness longer wavelength light. These methods rely on modifying the semiconductor material by controlling particle size, the addition of heteroatoms (doping), or by forming junctions between different semiconductor materials (composite catalysts).[28,63,66,107] Dye sensitized photocatalysts and dye sensitized solar cells employ redox cycling of a chromophore as the source of charge carriers and the

semiconductor serves only to carry current. This eliminates the need for photon energies exceeding the band gap of the semiconductor material but requires regenerating the oxidized sensitizer. The excited chromophore must have a conduction band energy exceeding that of the substrate to enable electron injection in to the semiconductor. Further reaction requires reduction of the oxidized chromophore via electrochemical reaction or reaction with a sacrificial electron donor.[103,108]

In a crystal at equilibrium all atoms are arranged such that the energy of the crystal is at a minimum. Defects within the crystal structure, the presence of heteroatoms, and discontinuities at crystal surfaces are all higher energy deviations from this ideal. Variations in electron density occur in atoms present at crystal faces, near heteroatoms, or near crystal defects and result in differences in the electrochemical potential (Fermi level) of electrons near the point of isentropy. These differences result in a surface energy greater than the bulk, typically expressed as excess Gibbs free energy per unit area.[109,110] Discontinuities in energy across the interface result in system evolution to minimize the difference. This implies that there is an isentropic chemical potential near the interface in both materials comprising the interface. In photocatalysts, the semiconductor Fermi level is shifted towards that of the bulk mobile phase, and the chemical potential of the mobile phase is shifted towards that of the solid, with the energy of the interface intermediate. This “band bending” can result in redox chemistry even if the redox potential of

the photogenerated charge carrier in the bulk semiconductor is lower than required to perform the desired reaction.[111,112]

3. THIN FILM CATALYST/SUBSTRATE SYSTEMS

Heterogeneous photocatalytic processes occur only at the interface between the catalyst and the mobile phase. Photons absorbed in the catalyst bulk must migrate farther to reach the working surface, are more likely to recombine, and are less likely to result in useful chemical work. Heterogeneous catalysis occurs only when reagents are adsorbed onto the surface, and the amount of reactant adsorbed is proportional to the surface area exposed. Reactor efficiency (volumetric, photometric, and economic as in the case of expensive catalysts) is maximized when the catalyst surface area to mass ratio is high. Micro and nano-particulate dispersions of photocatalyst in the mobile phase provide exceptional surface ratios, but separating the particulates from the treated stream or reaction products requires significant effort, i.e. nanofiltration, centrifugation, reverse osmosis, or long settling times. Additionally, particle settling or clustering can result in rapid loss of surface area or significant catalyst bypass without careful design consideration.[11]

Thin films of catalysts on suitable substrates avoid these problems. Porous thin films provide surface areas approaching that of activated carbon (*ca.* 600m^2/g) on a per mass basis, but can be

applied to large particles, textiles, reactor internal surfaces, or monolithic substrates.[11,113–119] These thin films can be prepared and applied by several techniques.

The most widely used and economically viable techniques rely on application of suspensions of catalyst particles to supporting surfaces to form thin membranes. Suspensions of particles, either suspended powders or sols, are typically deposited by dip coating, slip casting, spin coating, spray coating, or by electrophoresis. The deposited membrane has a smaller surface area than the particulate precursors; so starting materials are typically finely divided to ensure high membrane areas for use in heterogeneous catalysis. Commercial catalyst particle powders are typically suspended as slurry and are stabilized by controlling electrostatic repulsion or the use of steric stabilizers. Alternatively, sol gel chemistry is used to generate stable suspensions of nanoparticles from a solution, typically by hydrolysis of suitable precursor compounds. Semiconductor precursor choice and control of reaction conditions allows for the production of numerous particle shapes, precise control of particle size, and solution mass loading. Reaction by-products from hydrolysis of the precursor are easily removed by dialysis using osmotic membranes. Similar to slurries of powders, stability is improved through electrostatic and steric manipulations, with some sols stable for several years.

In addition to wet deposition techniques, dry powders can be applied to a substrate. An adhesive agent applied to the substrate surface will bond catalyst powder. Subsequent treatment

(i.e. pyrolysis) can remove the adhesive agent or chemically alter it to become a co-catalytic material. Electrostatically charging the dry powder and spraying it at an oppositely charged substrate, akin to the powder coating employed for applying durable paints, can provide precise control of membrane density and very thick coatings. As many photocatalysts are ceramic materials, physical operations like burnishing can press the particles into the support matrix, producing small "islands" of catalyst as opposed to continuous membranes. These techniques generate highly porous coatings and largely maintain the high surface area of the starting material.[105,120–125]

Alternative catalyst preparation techniques combine the steps of catalyst formation and deposition. Flame pyrolysis of precursor material is often used to deposit very fine catalyst particles at high rates, but requires a heat-resistant substrate material. Precision industrial coating techniques (physical vapor deposition, chemical vapor deposition, sputtering, pulsed laser deposition, etc.) result in the formation of highly consolidated, dense membranes but provide precise control of chemical composition and thickness. Electrochemical and oxidizing atmospheric techniques (anodizing, plasma electrolytic oxidation, thermal passivation, etc.) are useful when the desired catalyst is an oxidation product of a suitable substrate, with titanium oxides on titanium metal being a common example.[126,126–134]

One of the primary benefits of using supported photocatalytic thin films as opposed to particles is the ability to easily separate treated streams or chemical products from the catalyst. Photocatalytic films can be applied to almost any material, but an ideal substrate has to meet several important requirements. Photocatalysts require sufficient illumination to provide acceptable conversion rates, so the support should be largely transparent to those wavelengths that will activate the catalyst and be provided by the emitter technology employed. Illuminated photocatalyst is powerfully oxidizing and the substrate should be resistant to oxidation under reactor conditions or protected by an intermediate layer. The supporting material should be resistant to conditions in the reactor beyond oxidation by the catalyst (i.e. strongly basic solutions dissolve silica glass and fluoride ions attack titanium metal). The choice of a catalyst support strongly affects catalyst surface area. Materials with high intrinsic surface area like inorganic wools and textiles, raschig rings, thin waveguides, spun polymers, or small spheres increase reactor volumetric efficiency by accepting relatively high mass loadings of catalyst for a given volume of support.

After the catalyst is deposited on the surface, subsequent steps may be necessary to consolidate the catalyst. Several sintering techniques have been employed, with the most common being thermal treatment, although irradiance has been shown to modify the surface as

well.[135–137] Doping, oxidation, reduction, and alteration of the crystalline structure can also occur during the firing process.

SECTION 2: EXPERIMENTAL APPLICATIONS OF PHOTOACTIVE THIN FILM MEMBRANES

Photocatalytic oxidation of contaminated air by commercially available air cleaners was tested at environmentally relevant concentrations with single contaminants. Although the phenomenon of photocatalytic oxidation has been known for several decades widespread commercial adoption is a recent trend. There is currently limited literature regarding generalized reaction mechanisms, kinetics, and by-product formation for oxidative remediation; especially at low contaminant concentrations, at different levels of humidity, and especially among mixtures of contaminants. By-product formation during photocatalytic oxidation is of particular import to improving the indoor air environment, as long-lived intermediates may have increased human health hazards respective to their parent compounds. Gas phase removal kinetics and by-product formation patterns for several compounds were monitored by chemical ionization mass spectrometry.

Photoelectrocatalytic oxidation of aqueous ammonium to nitrogen was investigated and tested for suitability in aquacultural and aquarium applications. Ammonium is a by-product of biological conversion of nitrogenous feeds, is toxic at sufficient concentration, and accumulates in closed systems. Both bacteriological denitrification and dilution are used to maintain low ammonia levels but result in accumulation of nitrate ions or excessive water consumption and

waste emissions. Photoelectrocatalytic oxidation was found to remove ammonia without nitrite or nitrate accumulation and was significantly faster in water containing chloride ions, but resulted in formation of hypochlorite ion. Activated carbon was found to adequately remove hypochlorite ion and was used in construction of a hybrid system combining ammonia removal and hypochlorite removal.

The effectiveness of photoactive inorganic thin films as membrane forming curing compounds (IMFCCs) was also investigated. Concrete treated with IMFCCs was found to be resistant to scaling damage associated with freeze/thaw cycling while providing several other benefits. Increased evaporation rates through inorganic membranes was observed during testing, which is attributed to premature application and the formation of a highly porous xerogel upon contact with concrete bleed water of high pH and ionic strength.

1. Photocatalytic Remediation of Indoor Air Contaminants

Indoor air contamination can dramatically impact the health of occupants but is significantly less regulated than contamination occurring in outdoor air. Within the developed economies, the average person spends 70-90% of their day indoors, where they are exposed to constant, low-level, and potentially harmful emissions from a variety of sources. The cumulative effect of this exposure can result in a variety of health impacts, including chronic inflammation, increased

incidences of the immunologic disorders (*e.g.* asthma and allergies), the generalized sick building syndrome, and even premature death.[138] Recent efforts to improve the energy efficiency of constructed environments have resulted in building practices that focus on the construction of "tight" buildings, buildings with envelopes designed to limit uncontrolled air exchange and decrease fresh air turnover rates in HVAC systems. These construction practices can result in increased levels of volatile organic compounds (VOCs) when inadequate or poorly performing ventilation equipment is used. Several remediation technologies exist to remove these compounds without increasing the fresh air turnover rate including the use of adsorbents, non-catalytic oxidants, ozone and negative ion generation, and photocatalytic oxidation. Of these technologies, only photocatalytic oxidation does not require periodic replacement of media or result in the formation of potentially harmful concentrations of ozone gas.

A number of commercially available products seeking to capitalize on this promise are available, and the number of devices is increasing. These devices are designed to serve as stand-alone unit rooms, in-duct systems for treating buildings, as portable devices for use in automobiles and other vehicles. These devices embody a photoactive semiconductor catalyst (typically the anatase form of titanium dioxide) and a light source (typically low pressure mercury vapor fluorescent lighting) to oxidize the contaminant, as well as any required catalyst support or air handling equipment. Past research has shown that simple volatile organic chemicals (VOCs) like ethylene are oxidized directly

to carbon dioxide and water, but the reaction pathways of the more complex larger VOCs typically found in an indoor air environment are complex and can involve potentially harmful reaction intermediates. The formation rate of intermediate generation, and therefore the peak concentration attained, is a function not only of the catalyst surface but also several and other environmental variables, including temperature, humidity, surface irradiance intensity and wavelength, and the presence of other reaction variables. Reaction rates and mechanisms elucidated under one set of experimental conditions are likely valid only for those conditions. If these intermediates are present at dosages sufficient to cause a greater impact to human health and the parent compound, the use of PCO-based air cleaners is contraindicated.

Primary compound concentrations low enough to mimic that of indoor air are difficult to generate or detect, and intermediate concentrations are expected to be substantially lower. Therefore, the substantial majority of past research into by-product formation has been performed at concentrations substantially larger than those representative of the indoor air environment. Photocatalytic oxidation performed at these artificially high concentrations is typically modeled as having simple pseudo-first-order kinetics, as this model provides a reasonable fit to experimental data and rate constants are easily obtained. At more realistic concentrations, this simple model may fail to account for mass transfer rates or absorption kinetics limiting reaction rates, which suggests that more complex kinetic models may be required.

This research aims to provide an analysis of gas phase by-products from photocatalytically oxidative indoor air cleaning devices at realistic concentration levels of contamination. This information can be used to develop improved air treatment devices, a better modeling of the time and spatial evolution of contaminant profiles and concentrations, and equipment sizing guidelines.

1.1. MATERIALS AND METHODS

1.1.1. Tested Devices

A total of five commercially available air treatment devices were obtained as samples from vendors, or purchased on the open market. Table 1 provides a list of these devices and a brief description of their general form factor.

Device designation	Device description
Q	An in-duct device consisting of monolithic carbon blocks coated with photocatalytic material illuminated by a low-pressure mercury vapor germicidal lamp
G	An in-duct device consisting of a photocatalyst supported on nonwoven media
B	An induct device consisting of photocatalyst supported on perforated sheet metal surrounding an ozone generating low-pressure mercury vapor lamp
X	A stand-alone device consisting of 8 low-pressure mercury vapor lamps within a chamber, with the remaining chamber volume filled with quartz Raschig rings coated with photocatalyst and an axial blower fan to move air through the chamber
O	A stand-alone device consisting of a low-pressure mercury vapor germicidal lamp within a chamber, with the remaining chamber volume filled with quartz rushing rings coated with photocatalyst and an axial fan to pull air through the chamber

Table 1: Description of the commercially available devices tested during the score scope of this research.

Whenever possible, any additional filtration or absorbing elements were removed from the device prior to testing in order to isolate the effect of the photocatalytically active component and limit contamination between experiments.

1.1.2. Challenge Gasses

The tested devices were challenged with a suite of six compounds, representative of classes of compounds present in indoor air environments (Table 2). The compounds were chosen based upon the results of two large studies, one measuring contaminants in single-family homes, and the other a nationwide survey of schools (not published/proprietary). Challenge concentrations were chosen as the median value reported in these studies, and are in line with the published literature. Liquid samples of each contaminant were obtained from a large chemical supply vendor, and used in their as provided state.

Chemical Family	Chemical Name	Molecular Formula	MW	Representative concentration in indoor air (µg/m^3)
Aldehyde	Acetaldehyde	C2H4O	44.1	16
Alcohol	Ethanol	C2H6O	46.07	89
Ketone	2-Propanone (Acetone)	C3H6O	58.08	66.5
Aromatic HC	Toluene	C7H8	92.1	32
Chlorinated HC	1,2-Dichlorobenzene	C6H4Cl2	147	1.3
Terpene	d-Limonene	C10H16	136.2	3.7

Table 2: Challenge gasses and concentrations used during this experiment

1.1.3. Environmental test chamber

Each tested device was inserted into an electropolished 580L stainless steel chamber. The test chamber was outfitted with equipment for purging with purified air between experiments, humidity adjustment, and generation of the perquisite challenge gas concentration. The purge

system consisted of two packed beds of activated carbon and potassium permanganate ($KMnO_4$) impregnated zeolite prills. A centrifugal blower was used to pull air through this adsorbent bed and purge the chamber at a flow rate of approximately 30 SCFM. Humidity adjustment was performed through the use of a water sparging column or direct addition of water to the chamber. Challenge gases addition was accomplished through the use of a boiling chamber consisting of a 1L Erlenmeyer flask on a temperature controlled hotplate. An appropriately sized rubber stopper was fitted with a septum to allow injection of liquid contaminant using a microliter syringe. A small positive displacement pump was used to withdraw air from the environmental test chamber and pass it through the boiling chamber, whereupon it was returned to the environmental test chamber with the contaminant vapor. An axial fan capable of providing linear wind velocities of *ca.* 200 ft/min was used to mix the air within the chamber. A schematic of this test system is provided in Figure 2

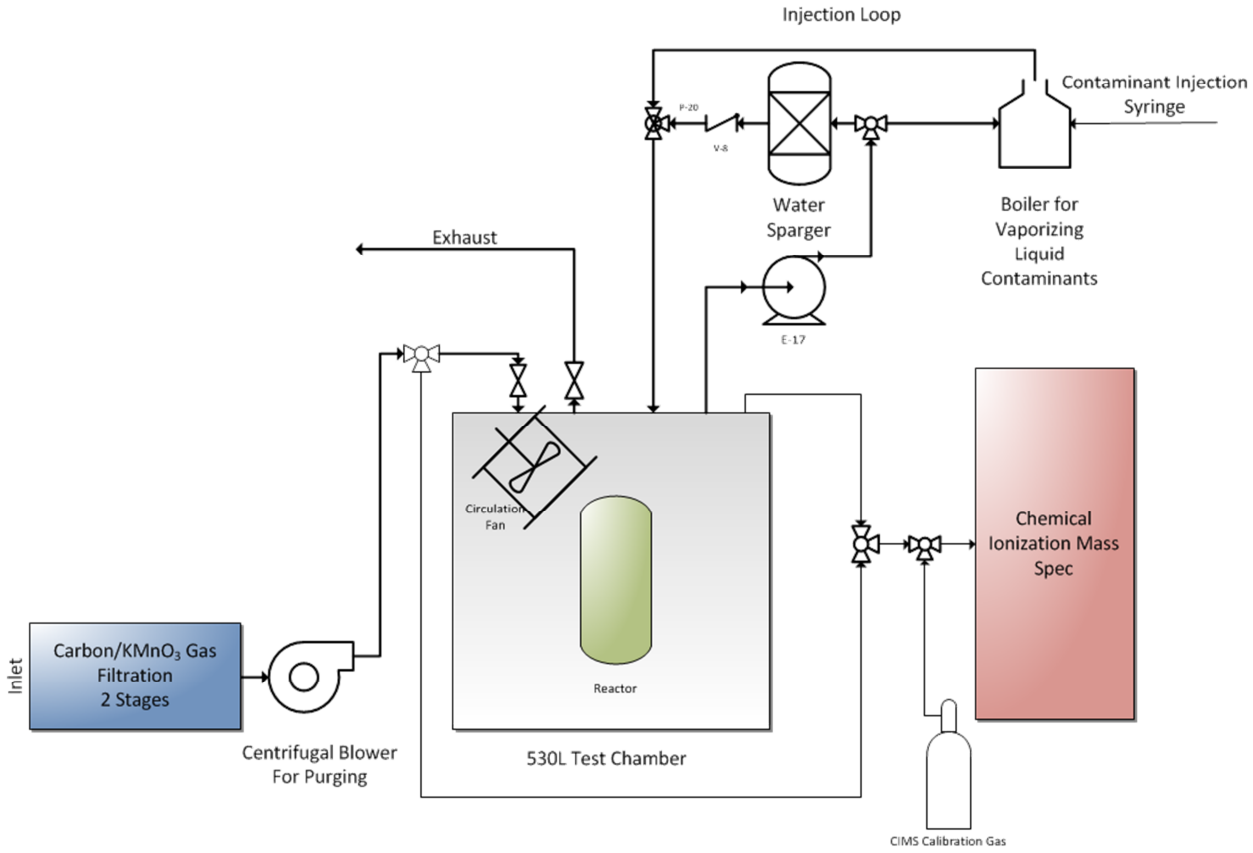

Figure 2: Schematic of environmental test chamber and apparatus

1.1.4. Primary compound and reaction intermediate detection

Detection of gas phase contaminants and reaction intermediates was performed using proton transfer resonance mass spectrometry (PTR-MS), a subtype of the techniques more generally known as chemical ionization mass spectrometry (CIMS). This instrument uses a glow discharge chamber to generate protonated water molecules that serve as a chemical ion source to gently ionize any gaseous molecule with a proton affinity greater than that of water. The ions and ion fragments are then separated by mass to charge ratio using a radio frequency quadrupole mass

analyzer. This technique allows for the near real time detection of a wide variety of gas phase compounds at low concentration with little fragmentation and no sample pretreatment.

The chamber was also instrumented with an ozone detector sensitive to part per billion mixing ratio (PPB_V) concentrations. This detector is based on the molecular absorbance of ozone at 254nm and is capable of measuring concentrations between sub-single PPB_V to several hundred PPM_V depending on calibration.

1.1.5. Experimental protocol

The device to be tested was inserted into the environmental test chamber and energized for a period of two hours while the purge system was activated to remove any contamination of the catalyst surface due to manufacturing or storage. The device was then powered down and the chamber was purged until all gas concentrations were constant. The humidity within the chamber was adjusted to 50±5% RH with either direct addition (followed by subsequent evaporation) of water to the chamber or through the use of a sparging column. The test chamber was in thermal equilibrium with the laboratory (23±2°C). An appropriate volume of the liquid contaminant or an aqueous solution of the liquid contaminant was injected into the heated boiling chamber using a gas tight microliter syringe. Gas phase contaminant concentration was monitored until the concentration was constant within a relative standard error of the mean of 5% over a 1 hour period, at which point the experiment began.

The equipment was energized (or an airtight cover was raised in the case of the adsorbent containing device) and the concentration of the primary daughter ions was logged once every 2 seconds. Every two minutes a mass scan covering the range from 20 to 150 amu was performed to detect the formation of reaction intermediates.

1.2. Results and Discussion

1.2.1. Contaminant removal

Of the devices tested, 3 were found to be ineffective at removing indoor air contaminants from the 580 L test chamber during a one-hour experiment (Figure 3). Product B utilized an ozone-generating lamp system and rapidly increased the chamber ozone concentration, reaching 173PPB$_v$ within 90 seconds. This level of ozone would have substantial implications for human health. No other tested device generated detectable ozone.

It is unknown why these devices failed to perform; photocatalytic conversion only requires that there is catalyst and adequate UV light present. These commercial devices all used light sources with sufficiently short wavelengths to generate electron-hole pairs in titanium dioxide and had an obvious catalyst coating. Possible explanations for this lack of efficacy are that the reactor geometry resulted in insufficient illumination, that the UV source(s) were insufficiently powerful, or that the catalyst used was deficient in some way.

There is still some debate in the literature as to the ideal crystalline structure of titanium dioxide for use in photocatalytic oxidation, but it is generally accepted that the anatase form is most effective and that amorphous material is largely non-oxidative. Commercially, catalysts are applied as either slurries of prepared powder or as stable suspensions derived from sol-gel chemistry. Slurry coatings are typically prepared from commercially available powders, but these powders might have large particle sizes that result in low surface areas, unknown crystalline structure, little adsorption, and low quantum (per photon) efficiency. Sol-gel coatings are often sintered at high temperature to provide mechanical strength and convert between crystalline structures, but coatings on substrates with low temperature stability cannot be treated in this way and might be largely amorphous.

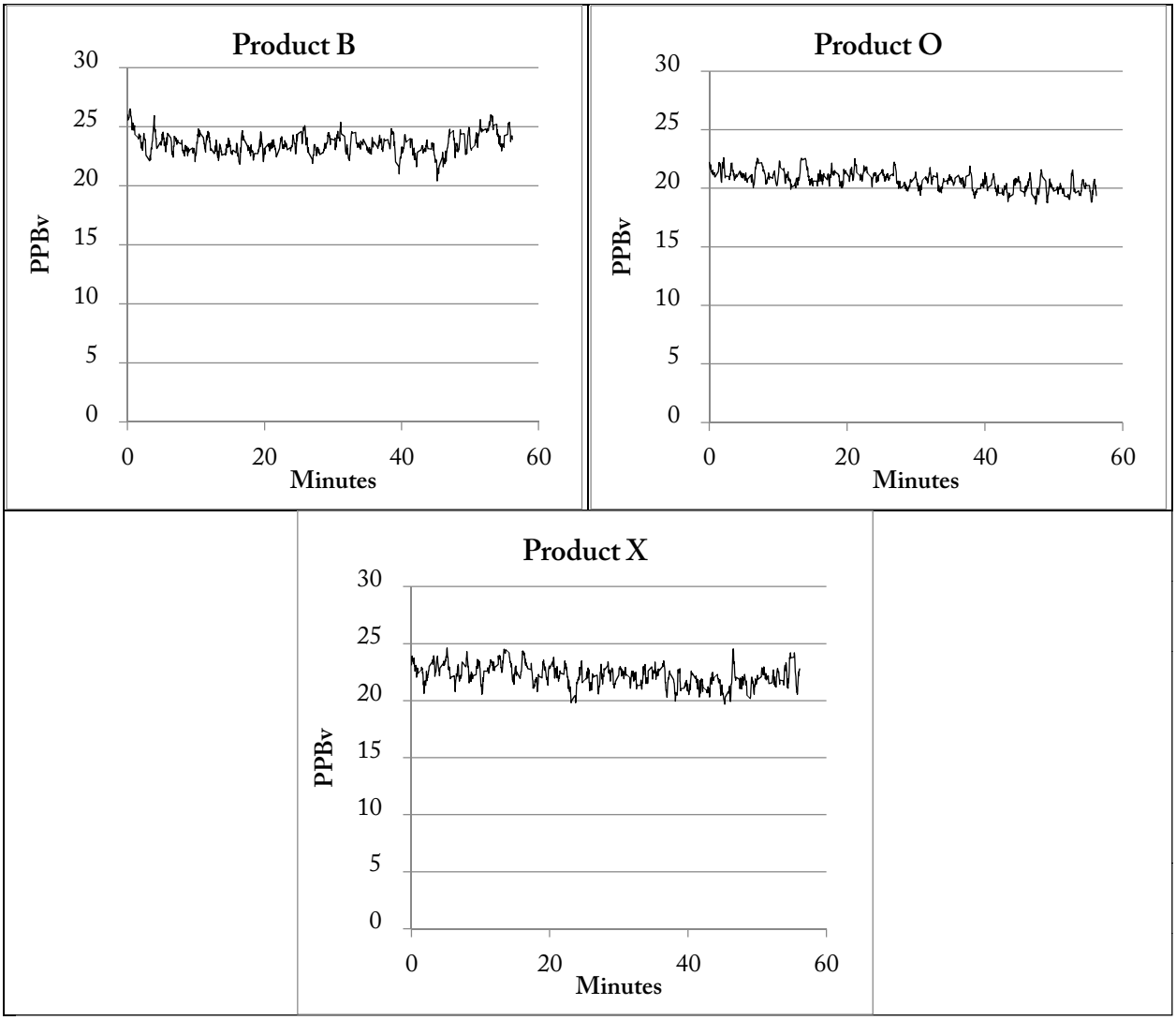

Figure 3: Ethanol concentrations during 1 hour operation in 580L chamber, other species not shown

Only products G and Q were found to impact concentrations sufficiently to serve as an air cleaning device. Product Q consisted of a photocatalytic component on an adsorbing substrate, so studies were performed with and without UV irradiation of the photoactive surface to determine the relative effect of each component. There was no significant difference in ethanol removal between operation with and without UV illumination of the catalyst surface (Figure 4)

(p=0.05, n=3). It is possible that there was catalytic activity masked by the effectiveness of the adsorbent component.

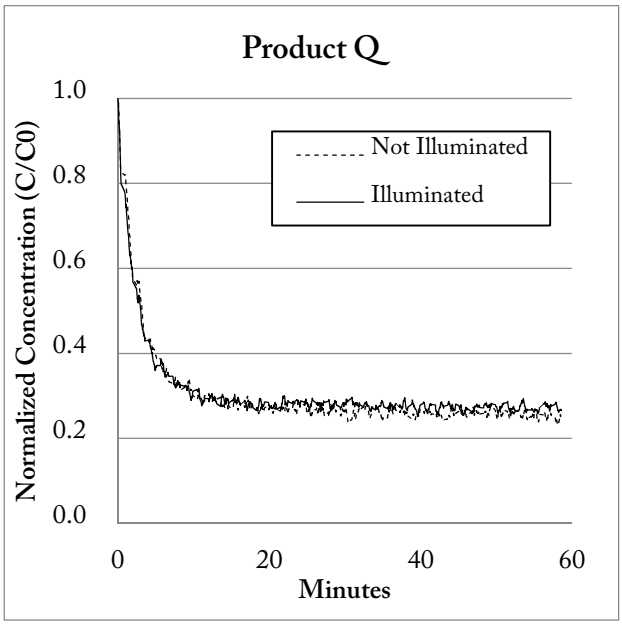

Figure 4: Ethanol concentration during one hour operation in 580 leader chamber. Removal efficiency was not affected by UV illumination of the catalyst surface.

Product G was found to effectively remove indoor air contamination (Figure 5). Most research into photocatalytic conversion of gaseous species models the system as having pseudo-first order kinetics, presumably due to the ease of determination of kinetic rate constants and reasonable fit to the data, especially at high concentrations. This model did not adequately fit the data collected during this study. The use of environmentally relevant concentrations increases the likelihood that there is a rate-limiting diffusion component not accounted for in first order kinetic models. Additionally, even with the use of UHP air and a gas adsorbing media there were several other gas-phase species present in the purge gas supplying the reaction chamber. A more

realistic kinetic model (Michaelis-Menton, Langmuir-Hinshelwood, *etc.*) that accounts for diffusive control and competition for adsorptive and reacting sites on the photocatalyst surface is likely to better fit these results. Application of these models will require additional analytic methods not utilized during this experiment, particularly techniques capable of measuring adsorption isotherms under UV illumination, identification of strongly adsorbed (non-volatile) reaction intermediates, and for generating highly pure (sub PPB_V) air in the chamber.

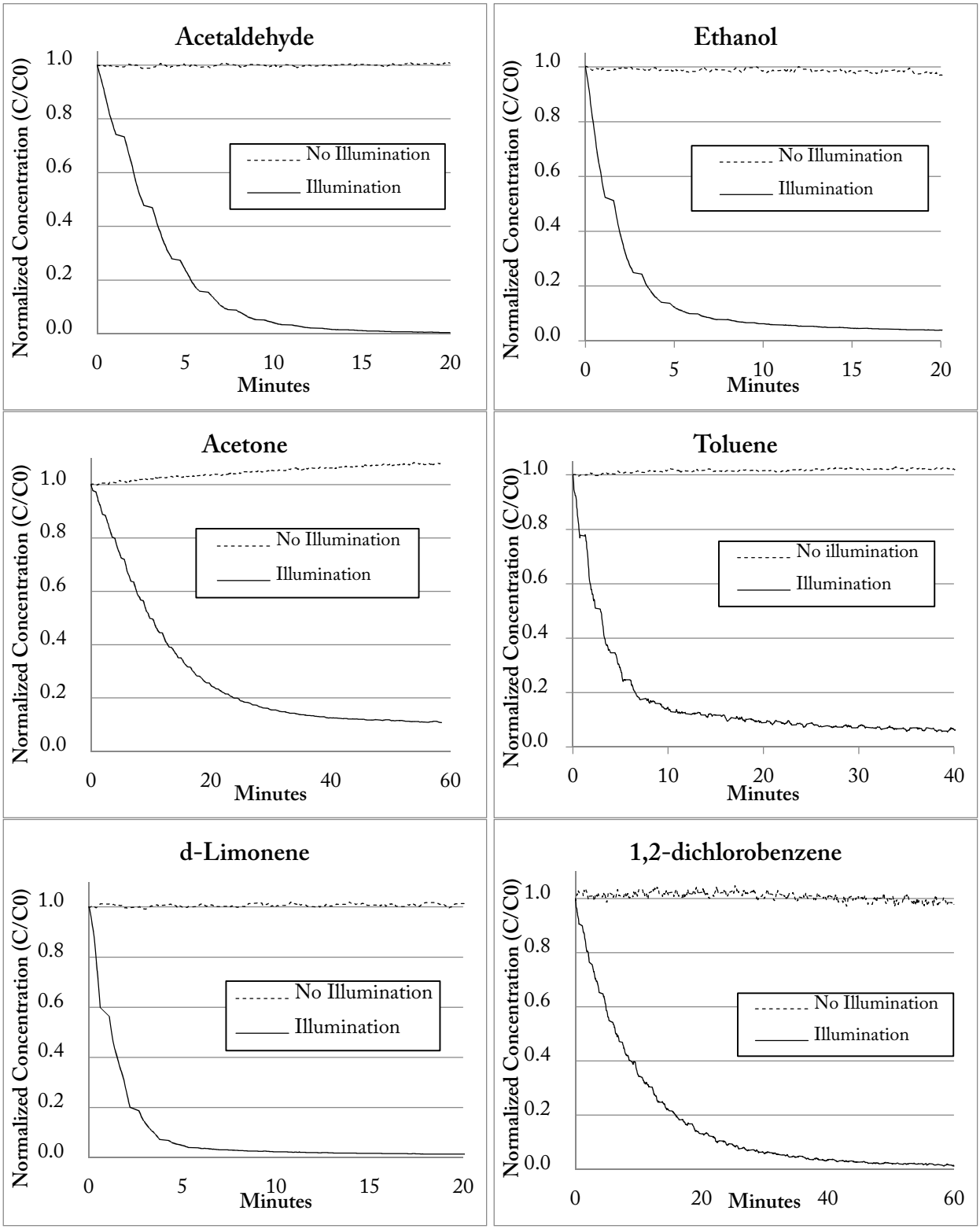

Figure 5: Contaminant removal by Product G

1.2.2. By-product Formation

The use of chemical ionization mass spectroscopy not only enabled measurement of contaminant concentrations at environmentally relevant concentration but also detection of volatile gaseous reaction intermediates. Photocatalytic oxidation primarily occurs through reaction pathways involving oxidative radicals that are generated at finite rates, which results in reaction mechanisms that involve multiple pathways (the strongly oxidizing radical is non-selective) and stepwise conversion to the final product (ideally CO_2). Each of these intermediates will have a different affinity for the catalyst surface: strongly adhering species can poison the catalyst or oxidize further to products that desorb. Weakly adhering species can desorb without reaction and appear in the gas phase. The presence of multiple species in the chamber further complicates modeling relevant reactions. Water adsorbed on the surface is often the source of these radicals being photogenerated, so reaction mechanisms are often humidity dependent.

1.2.2.1. Acetaldehyde

Acetaldehyde was the lightest compound tested during this study and has the smallest likelihood of by-product formation. There was evidence of some slight formation of formaldehyde that was rapidly oxidized (Figure 6).

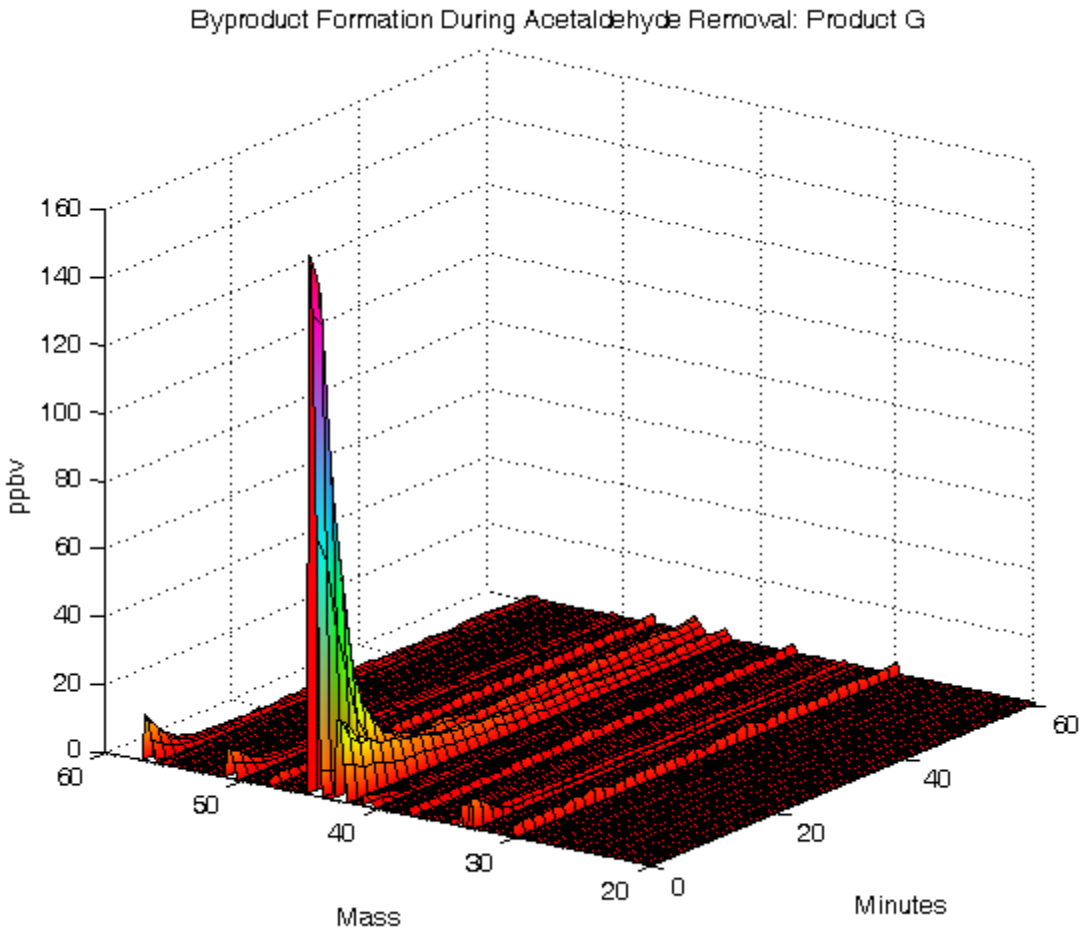

Figure 6: Surface plot of mass spectra during photocatalytic oxidation of acetaldehyde

1.2.2.2. Ethanol

Photocatalytic oxidation of ethanol has been reported to result in the formation of acetaldehyde, and is supported by this research as seen in the small peak at m/z=45 (Figure 7). This reaction by-product appears to oxidize more easily than ethanol, and is rapidly further oxidized. There is a large peak of formaldehyde present at the beginning of this experiment, but

no evidence of formaldehyde generation was found. The source of this compound is unknown, but contamination of the liquid ethanol used during this study appears to be most likely.

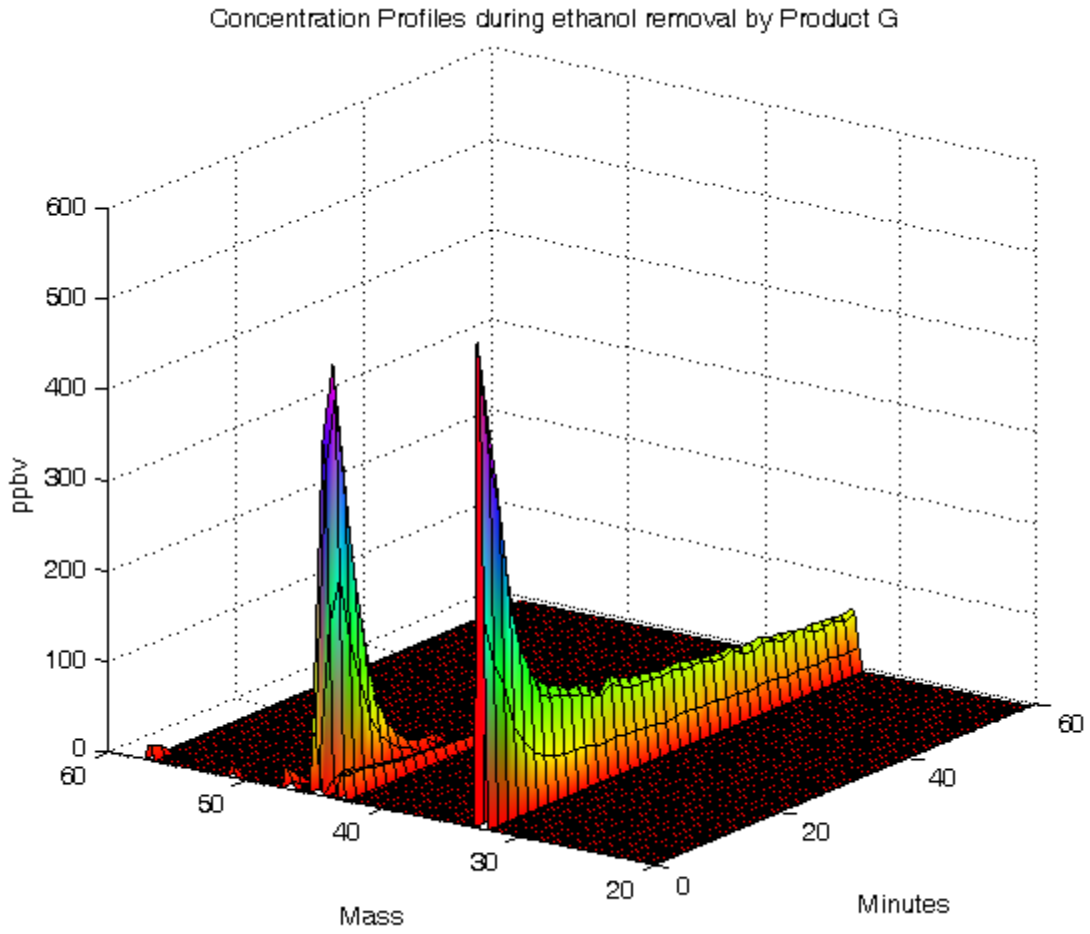

Figure 7: Surface plot of mass spectra during photocatalytic oxidation of ethanol

1.2.2.3. Acetone

Acetaldehyde was generated at a significant rate during oxidation of acetone, but was rapidly further oxidized (Figure 8). The small peak at 43 amu is an artifact of PTR-MS measurement of acetone.

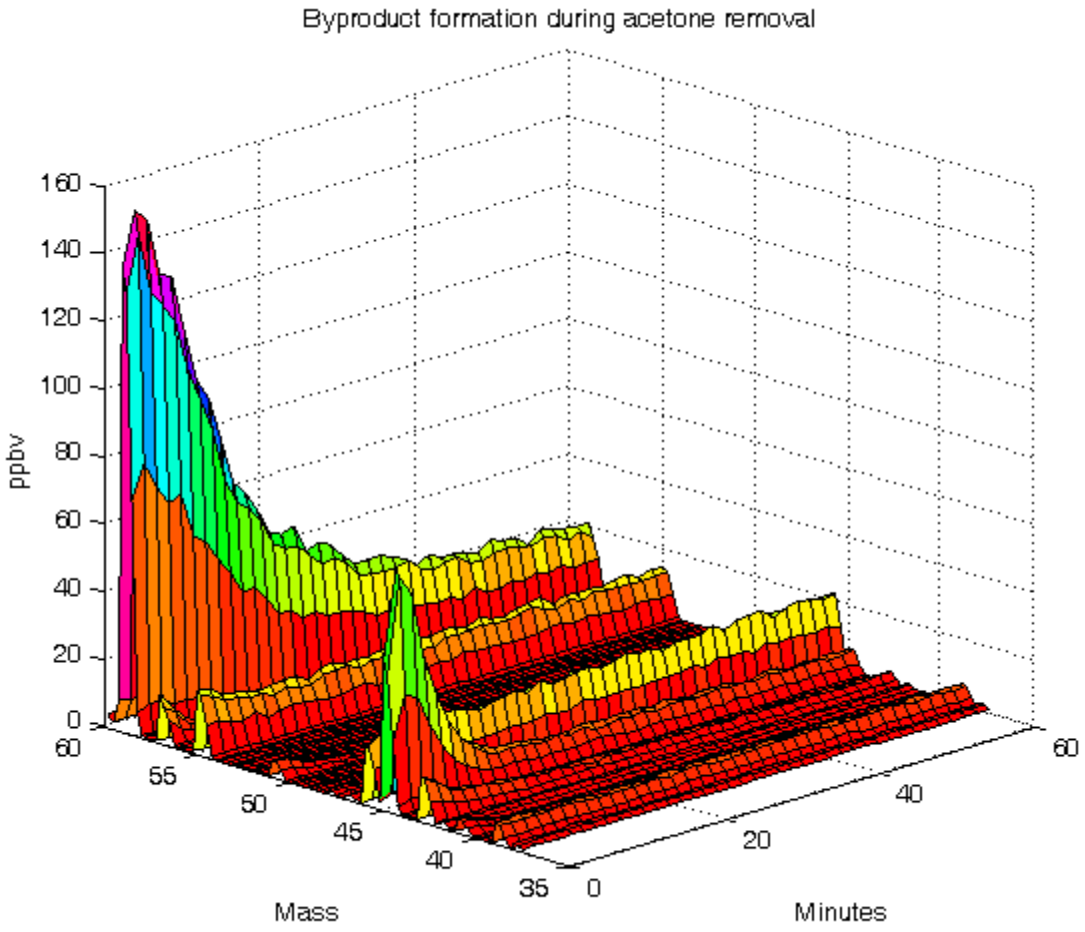

Figure 8: Surface plot of mass spectra during photocatalytic oxidation of acetone

1.2.2.4. Toluene

Oxidation of toluene was not associated with the formation of any reaction intermediates, although several compounds were present at the experiment start (Figure 9). The largest peaks

present correspond to an m/z ratio of 75, isobaric with methyl acetate, and acetaldehyde at 44. The high concentration of these species suggests either contamination or a material incompatibility with a component of the reactor or experimental apparatus.

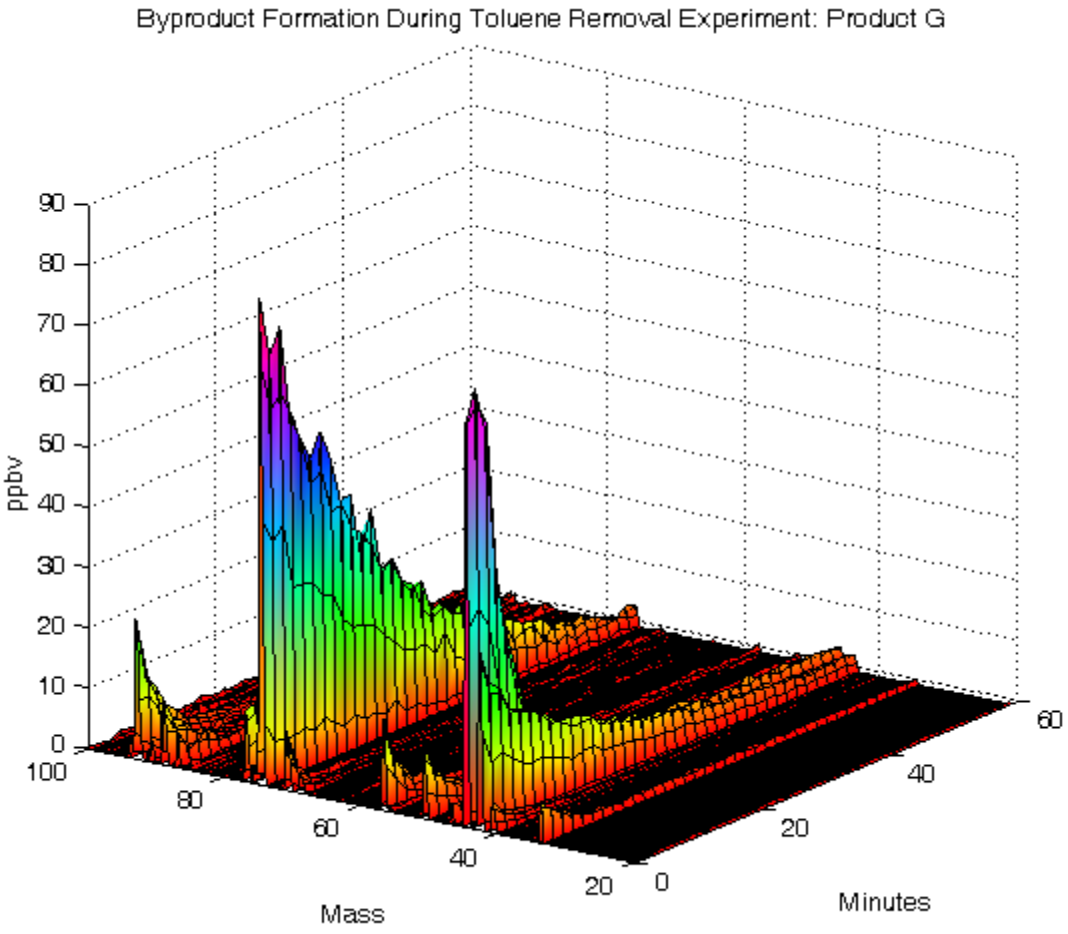

Figure 9: Surface plot of mass spectra during photocatalytic oxidation of toluene

1.2.2.5. d-Limonene

Oxidation of d-Limonene was associated with the formation of monoterpenes (m/z=93) and acetone(m/z=59). The large peak at m/z=81 is due to a known fragment generated during PTR-MS detection of limonene (Figure 10).[139]

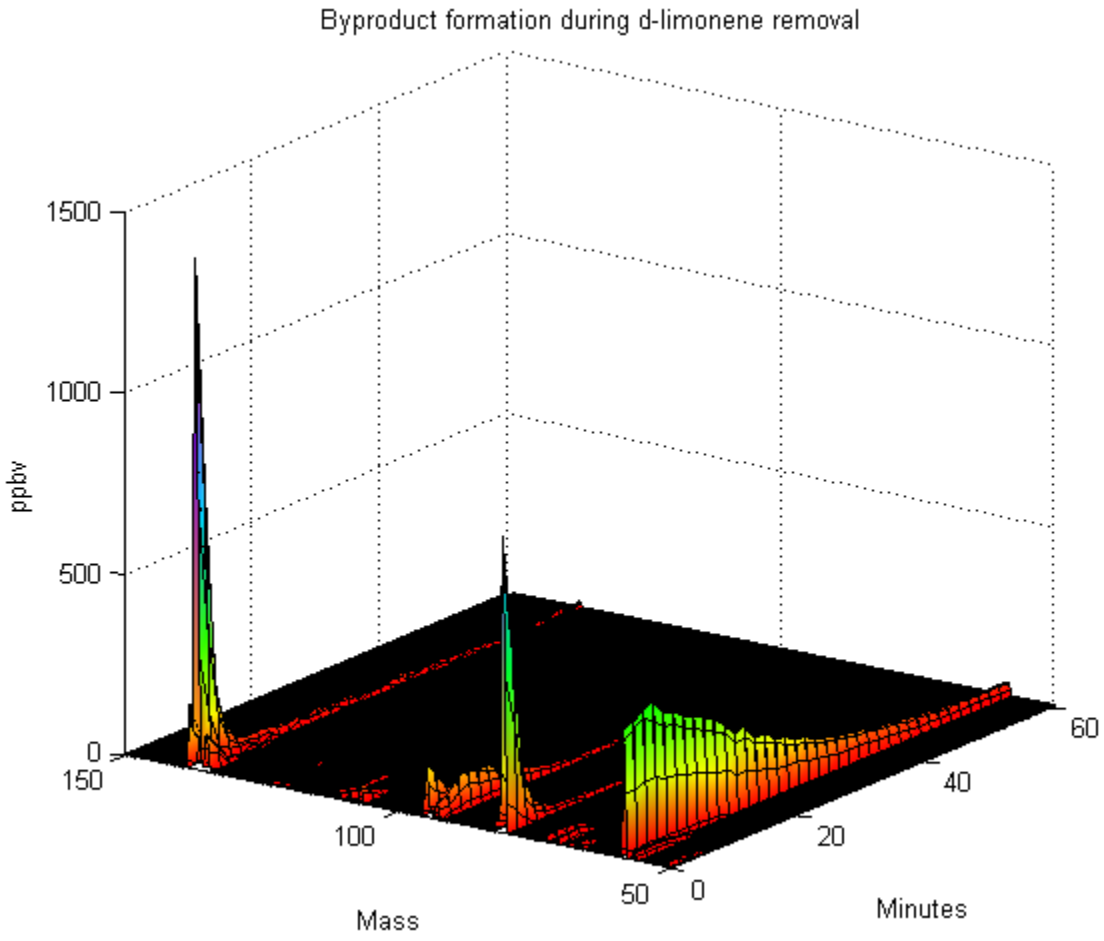

Figure 10: Surface plot of mass spectra during photocatalytic oxidation of d-Limonene

1.2.2.6. 1,2-Dichlorobenzene

Oxidation of 1,2-Dichlorobenzene resulted in the formation of acetaldehyde at low concentration (Figure 11). The lack of a peak at m/z=100 indicates that no phosgene was produced during this reaction. Phosgene has been reported as a possible by-product during photocatalytic oxidation of chlorinated compounds.

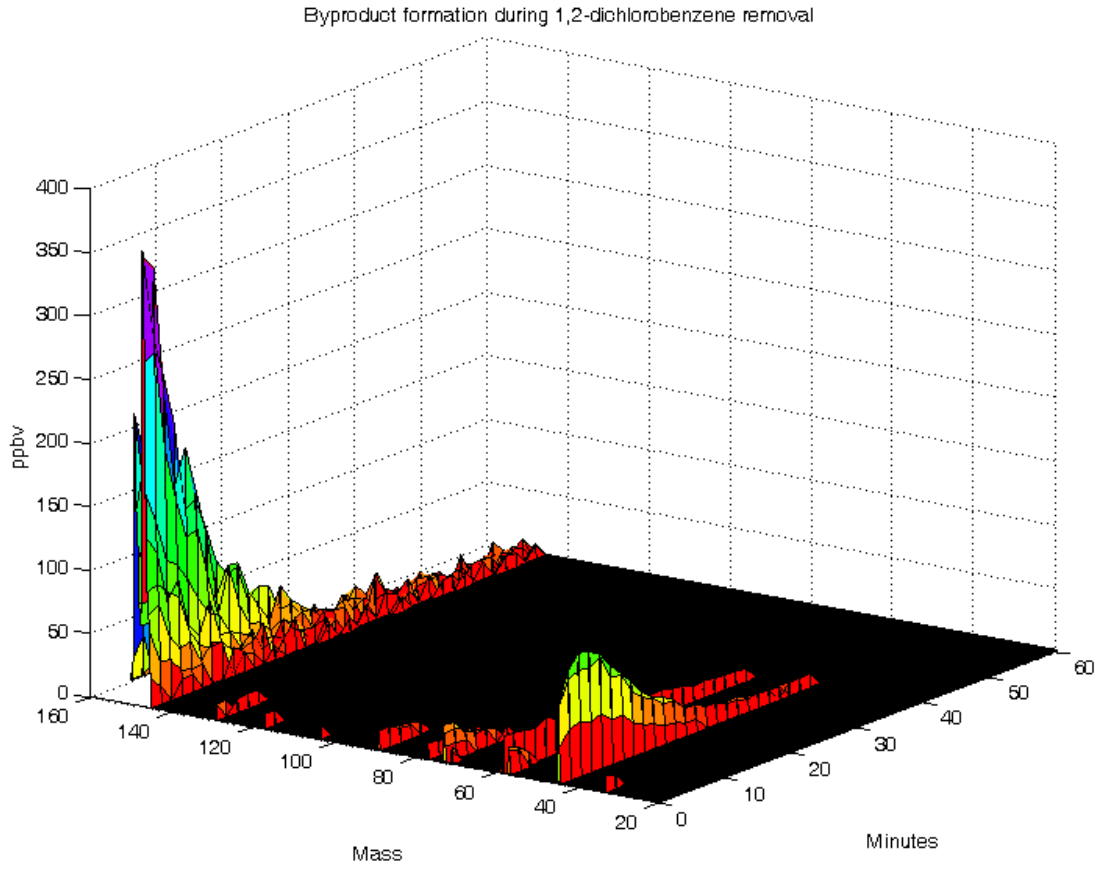

Figure 11: Surface plot of mass spectra during photocatalytic oxidation of 1,2-Dichlorobenzene

1.3. CONCLUSIONS:

Photocatalytic oxidation is currently being developed and sold by a number of commercial vendors. Seven representative units were acquired and tested using a suite of contaminants commonly present in indoor air at relevant concentrations in a 580L test chamber. Of these 5 devices, three failed to remove the challenge compounds during the hour experimental period and a fourth was found to provide no additional benefit over the adsorbent catalyst substrate. The fifth device oxidized the contaminants but required several minutes to decrease concentrations by half in a well-mixed chamber under $1m^3$ in internal volume. This reactor was designed to be fit into building ductwork and handle more than $5m^3$/minute (~200cfm), which dramatically exceeds its single pass conversion capacity.

Reaction mechanisms have been determined for a number of compounds but these mechanisms are typically determined at relatively high concentrations, for single or very few components and for only a few humidity conditions. Reactors intended for use in actual indoor environments will encounter substantially differing operating conditions. This research has shown that conversion of high mass contaminants under conditions relevant to the indoor air environment results in the formation of reaction intermediates including acetone, acetaldehyde, and formaldehyde, but these compounds were relatively low in concentration and quickly further oxidized.

2. PHOTOELECTROCATALYTIC OXIDATION OF AMMONIUM

A problem with aquariums and recirculation aquaculture systems that rely on biofiltration is the accumulation of nitrogenous compounds in the water. Photoelectrocatalytic oxidation (PECO) is a possible solution to this problem, as bench-scale studies have demonstrated that PECO systems can oxidize ammonia directly into nitrogen gas. [140] PECO technology consists of a conductive metal electrode (anode) coated with an ultra-thin layer (300-500 nm thick) of a titania-based photocatalyst. When the photocatalyst is illuminated with light of sufficient energy (near-UV), electrons in the valence band of the titania are excited into the conduction band and produce highly reactive electron/hole pairs that mediate oxidation of ammonia. The efficiency of this photocatalytic process is improved by applying a positive potential ("bias") across the photoanode, which decreases the recombination rate of photogenerated electrons and holes.[141–143] The mechanism by which these photogenerated holes act to oxidize ammonia is not known with certainty, but the most likely possibility is that the holes oxidize chloride ions in the water to form highly reactive chlorine species which diffuse into the water and react with ammonia.[144] Other potential mechanisms include the direct oxidation of ammonia on the anode surface, or the oxidation of water into hydroxyl radicals that, in turn, oxidize ammonia in solution. The PECO system is an electrolytic cell in which the photogenerated electrons flow to the cathode and react with water to produce hydrogen gas (H_2) and hydroxide ions.

This investigation was conducted to evaluate the PECO process as a possible replacement to biofiltration in closed rearing systems (aquariums and recirculation aquaculture systems). The specific objectives were to characterize the effect of varying the following parameters on the ability of a PECO system to oxidize dissolved ammonia into nitrogen gas: (1) photocatalyst thickness and crystalline structure, (2) aeration and water turbulence, (3) salt concentration, (4) pH, and (5) applied potential. In addition, studies were conducted using aquarium-scale, flow-through prototypes to evaluate PECO performance under practical conditions using live fish.

2.1. Materials and Methods

2.1.1. Photoanode preparation

Photoanodes were prepared by coating Ti metal foil (15 cm x 15 cm x 0.050 mm (thick), 99.6+% pure; Goodfellow Corp.; Oakdale, PA) with a proprietary titania-based metal oxide (AquaMOST, LLC; Madison, WI). Prior to coating, the Ti foil was cleaned with a detergent solution, and rinsed with deionized water followed by acetone. The foil was heated at 350°C for 4 hours to char the surface, remove any remaining organic contaminants, and form an oxide layer to improve coating adhesion. Following this pretreatment, the metal foil was dip-coated three or five times with an aqueous suspension of titania prepared using sol-gel processing methods.[145] The foil was withdrawn at a rate of ~3.0 mm/sec to control the thickness of the titania coating on the surface of the electrode. After each coating, the coated foil was air dried for 10-15 min,

then dried in an oven at 70˚C or 100˚C for 45 min. After applying the last coat, the coated foil was fired in an air atmosphere with a 3˚C/min ramp rate to a final temperature of either 300˚C or 500˚C for 4 hours.

Platinized photoanodes were prepared similarly using a platinized sol. Chloroplatinic acid was added to the titania sol to obtain the desired loading of platinum (1 weight %). The adsorbed chloroplatinic acid was then reduced using a sodium borohydride solution.

2.1.2. Static test system

Most experiments were performed using a 3-electrode configuration (photoanode, cathode, and reference electrode). In this set-up, a multi-channel potentiostat (Model VMP2, Princeton Applied Research (PAR); Oak Ridge, TN) was used to control the voltage applied to the photoanode with respect to a silver wire reference electrode (0.5 mm diameter, 15 cm length; Goodfellow Corp.; Oakdale, PA). The silver wire acts as an Ag/AgCl half-cell in water that contains chloride ions and provides a known and essentially constant voltage. All voltages are reported with respect to this reference electrode. There was a potential of ~1V between the reference and the counter electrode (cathode), dependent on the current density and chemical environment near the titania-solution interface, so the PECO system operated at ~2V. The cathode was a Ti wire (0.5 mm diameter, 15 cm length, Goodfellow Corp.). The potentiostat was controlled using EC-Lab V.92 software (PAR), which also recorded the current and voltage.

The photoanode was rolled into a cylinder and placed against the inner wall of a 300-mL glass beaker. A 9-W germicidal UV lamp was positioned within a quartz sleeve (32 mm ID, 35 mm OD, 15 cm long), in the center of the beaker. The distance from the lamp to the photoanode was approximately 2 cm. The cathode and reference electrode were attached to the outer wall of the quartz sleeve and positioned parallel to each other 2 cm apart (Figure 12).

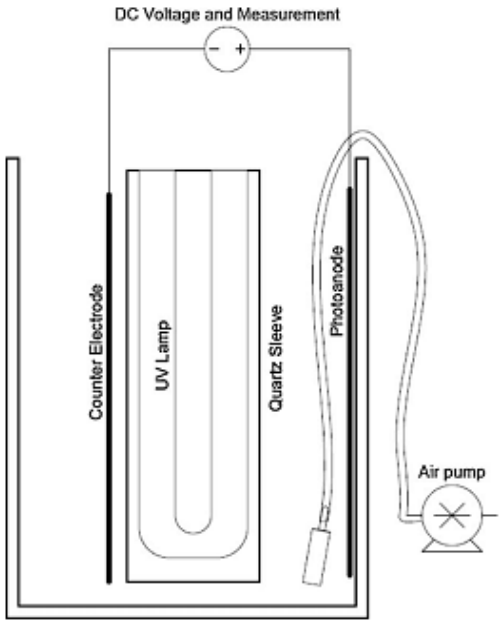

Figure 12: Schematic of the static PECO test system

2.1.3. Experiment procedure

Glass beakers were filled with 250 mL of either 100% seawater made using 40.5 g/L Instant Ocean® or water containing 1 g/L NaCl (low-salt water). The water was spiked with ammonium chloride to provide an initial concentration of 0.5 to ~10 mg/L nitrogen as ammonia. The wetted area of each photoanode was 180 cm^2. In most experiments, air was bubbled into each beaker to

provide aeration and uniform mixing of the water. All experiments were conducted at room temperature (23˚C ± 2˚C). During studies assessing the effects of pH on ammonia removal in low-salt water (1 g/L NaCl), pH was adjusted using NaOH or HCl and measured with a pH meter. The effects of pH on ammonia removal were not investigated in seawater because seawater is well buffered.

The experiments were started by simultaneously energizing the UV lamps and applying the electrical bias to the electrodes. Water samples were collected in 1.5 mL microcentrifuge tubes at set intervals (typically every 2-5 min) to determine ammonia concentrations. In addition, 10-ml water samples were collected at the end of most experiments for analysis of nitrite and nitrate concentrations. Water samples were analyzed within 1 hour after collection or stored at 4°C for later analysis. Preliminary studies indicated that no changes in ammonia, nitrite or nitrate concentrations were observed when the samples were stored for up to one week under these conditions. In initial experiments, we demonstrated that ammonia removal required both the presence of UV light and an applied voltage; therefore, controls were typically test units with UV lights on, but no applied voltage.

Ammonia concentrations were determined using the indophenol method modified for use with a microtitre plate spectrophotometer. The ammonia test reagents were obtained from Tetra (Blacksburg, WV). An ion chromatograph (Dionex; Sunnyvale, CA) was used to determine

nitrite and nitrate concentrations. Chloramines (NCl_3, $NHCl_2$, and NH_2Cl) were also detected via the indophenol method, and total chlorine was measured using the DPD method with a Hach DR/4000U spectrophotometer (Hach Company; Loveland, CO).

2.1.4. Flow-through PECO test system

A flow-through PECO device was fabricated by adding PECO electrodes to a commercial 9-W UV sterilizer (Jebo Co., Inc.; Hong Kong, China). The anode was located peripherally, and the cathode was a Ti wire that ran the length of the quartz sleeve. A Ti wire was spot-welded to the anode and this wire and the cathode were fitted through holes drilled into the body of the UV sterilizer to make the external electrical connections. The holes were sealed with epoxy. No reference electrode was used, and a constant voltage was applied between the anode and cathode. Flow-through experiments without fish were conducted using 7 L aquariums filled with seawater (40.5 g/L Instant Ocean®) and spiked with ~0.7 ppm ammonia-nitrogen. The water flow rate was 0.13 L/min and the residence time in the unit was 1.1 minutes. For the fish experiment, tilapia (Oreochromis niloticus) were purchased from Americulture, Inc. (Animas, NM), and fed a high protein (45%) salmon diet (Nelson and Sons, Murray, UT).

2.1.5. Statistics

Replicate studies were performed using either three or four identical PECO systems. Data are reported as the mean ± standard error of the mean (SEM). All ammonia, nitrite and nitrate data are reported as ppm (mg/L) nitrogen (e.g., ammonia-nitrogen, nitrate-nitrogen).

2.2. Results and Discussion

2.2.1. Effect of photoanode firing temperature and TiO_2 film thickness

In low-salt water (1 g/L NaCl), photoanodes prepared by firing the titania film at 500°C removed ammonia significantly faster than photoanodes prepared by firing the titania film at 300°C (Figure 13). This confirms earlier results showing that rutile thin-films have a higher catalytic activity than anatase films in some applications.[1461] The rate of ammonia removal was unaffected by the number of titania coatings at either firing temperature (Figure 13).

[1] After publication of the manuscript from which this section is based further reading indicated that the rate of the conversion between the anatase and rutile phase is dependent on temperature, particle size, and adsorbed surface species, especially water vapor, and that this conversion is unlikely to have progressed appreciatively during the short time during which the specimens were annealed.[147] It is likely that the increased photoelectrocatalytic activity is due to greater conversion of amorphous titania to the anatase phase, the formation of a mixed crystalline system, or increased oxide layer thickness due to oxidation of the substrate.

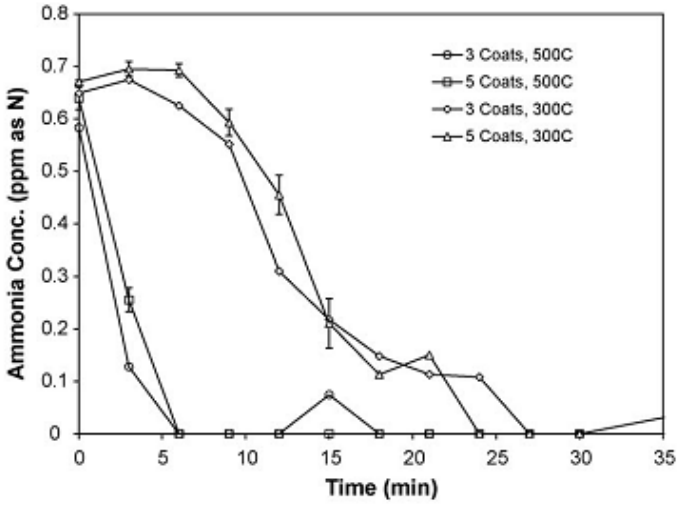

Figure 13: Ammonia removal as a function of photoanode fabrication variables including number of catalyst coatings and sintering temperature. Experiments were conducted in static test reactors (pH 7) with aeration and with an initial ammonia concentration of 1.6 mg/L NH_4Cl in 1 g/L NaCl (freshwater) and an applied voltage of +1.0 V. Data shown are mean ± SEM (n = 4). The symbol 'x' in the lower right corner indicates the concentration of nitrate (in ppm as N) remaining in solution after 30 min of operation in experiments with the electrode that was coated three times and fired at 500°C.

Less than 15% of the ammonia-nitrogen added to the system was converted to nitrate-nitrogen (Table 1). Little to no ammonia-nitrogen was converted to nitrite-nitrogen (Table 1) or chloramines. Together, these observations indicated that the majority of ammonia-nitrogen is converted directly into nitrogen gas by the PECO reactor. Similar observations have been previously reported.[140,148]

Table 3: Formation of nitrate and nitrite after 30 min of testing with non-platinized photoanodes under the same test conditions used to generate data in Figure 2 with standard error.

Photoanode formulation	Initial ammonia conc. (ppm as N)	30-min nitrate conc. (ppm as N)[1]	% nitrogen as nitrate in system	30-min nitrite conc. (ppm as N)	% nitrogen as nitrite in system
3 coats TiO_2, 300˚C	0.65±0.04	0.094±0.001	14.5	0.005±0.009[2]	0.8
5 coats TiO_2,300˚C	0.67±0.04	0.095±0.0002	14.2	0.000	0.0
3 coats TiO_2, 500˚C	0.58±0.12	0.083±0.005	14.2	0.000	0.0
5 coats TiO_2, 500˚C	0.64±0.07	0.088±0.004	13.8	0.000	0.0

[1] The test solution had an initial nitrate concentration of approximately 4 ppb as N.

[2] This value is based on one measurement above non-detectable levels. Two other replicate measurements for this photoanode formulation were non-detectable for nitrite.

2.2.2. Effect of high initial ammonia concentration

A reactor system was tested with an initial ammonia concentration of 9 ppm N as ammonia, and the kinetics of ammonia removal showed no qualitative difference from lower concentrations, suggesting that the technology could be applied to remediate waters more contaminated than natural systems (Figure 14).

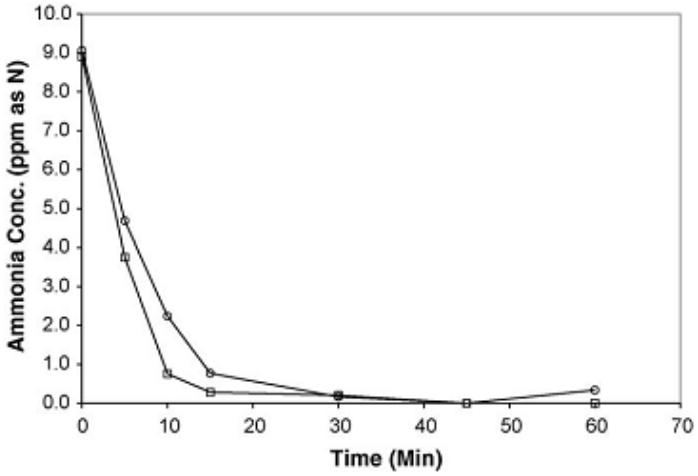

Figure 14: Ammonia removal from aerated water within static test reactor spiked with and initial ammonia concentration of 16 mg/L NH4Cl. Experiments conducted in 40.5g/L Instant Ocean solution with 1.0V applied voltage

2.2.3. Effect of Platinum doping

There was no significant difference in ammonia removal between un-doped and Platinum-doped titania coatings fired at either 300˚C or 500ºC (data not shown). Moreover, there was no

difference in nitrate formation between platinized and non-platinized photoanodes at either firing temperature, with approximately 15% of the ammonia-nitrogen converted to nitrate-nitrogen in all tests (data not shown). The data suggest that there is no advantage of using Platinum-doped titania thin films over pure titania films for converting aqueous ammonia into nitrogen gas in a PECO system.

In contrast, platinized titania is more efficient at converting ammonia-nitrogen into nitrogen gas (N_2) than un-doped titania in a photocatalytic system with no applied electrical bias.[148] A likely explanation for this difference between photocatalytic systems and PECO systems is that platinum acts as a sink for photo-generated electrons in the former, whereas the electrical bias in PECO systems is much more effective at removing electrons.

2.2.4. Effect of aeration and water movement

The rate of ammonia removal was significantly faster if the water in the static experiments was aerated. At least two hypotheses can explain this phenomenon. First, aeration may disrupt a boundary layer at the anode surface that otherwise slows the delivery of reactants (e.g., ammonia) to the anode surface, or the movement of photo-generated oxidants to the bulk solution (e.g., chloride ions, hypochlorous acid). Two, aeration supplies oxygen required for the redox reactions occurring in PECO electrolytic system. An experiment was conducted to test these hypotheses. There were four treatment groups: (1) control, static (no air, no stirring); (2) water mixed with a

magnetic stir bar; (3) aeration with an air stone, and (4) aeration with argon gas (water movement but no oxygen).

Any mixing of the water, even in the complete absence of oxygen (treatment 4), increased the ammonia removal rate compared to static water. The results support the hypothesis that the reaction rate was diffusion limited by a boundary layer. The disruption of the layer will be necessary to maximize reaction kinetics in PECO flow-through systems designed to remove ammonia in commercial aquarium and aquaculture applications.

2.2.5. Effect of salinity

Ammonia removal was significantly faster in 100% seawater (40.5 g/L Instant Ocean®) compared to water containing 1 g/L NaCl (Figure 15). No significant ammonia removal was observed in distilled water without any added salt. There are at least three explanations for these observations. First, water must have a minimum ionic strength for PECO reactions to occur as electrochemical reactions are limited by the ability of the system to conduct current. This idea was not supported, however, by data showing no ammonia removal in high conductivity water in which the chloride ions were replaced with an equimolar concentration of sulfate ions as added sodium sulfate. Second, chloride ions are required for the silver reference electrode to form a silver/silver chloride half-cell and maintain the proper voltage between the anode and cathode. This hypothesis is not supported by data showing no ammonia removal when a saturated calomel

reference electrode replaced the silver wire reference electrode. Third, chlorine (Cl_2) and hypochlorous acid (HClO) are generated in situ from chloride ions in the water according to the following:[144,149]

Equation 2: Conversion of Ammonia to nitrogen gas

$$2\ Cl^- \rightarrow Cl_2 + 2\ e^-$$
$$Cl_2 + H_2O \rightarrow HClO + Cl^- + H^+$$
$$2\ NH_4^+ + 3\ HClO \rightarrow N_2 + 3\ H_2O + 5\ H^+ + 3\ Cl^-$$

In these reactions, hypochlorous acid reacts with ammonia to form nitrogen gas (N_2). The hypothesis that ammonia oxidation is meditated by the electrolytic production of chlorine and hypochlorous acid is supported by data showing that little or no nitrite or nitrate were produced during the PECO reactions (Table 4), and the direct measurement of chlorine production in the flow-through experiments. An additional mechanism that occurs in seawater is the reaction of hypochlorous acid with bromine ion to form hypobromous acid according to the reactions below.[150] Hypobromous acid can also react with ammonia to form nitrogen gas (Equation 3).[151]

Equation 3: Bromine as the halide in ammonium conversion

$$HClO + Br\text{-} \rightarrow HBrO + Cl\text{-}$$
$$2NH_4^+ + 3HBrO \rightarrow N_2 + 3H_2O + 5H^+ + 3Br^-$$

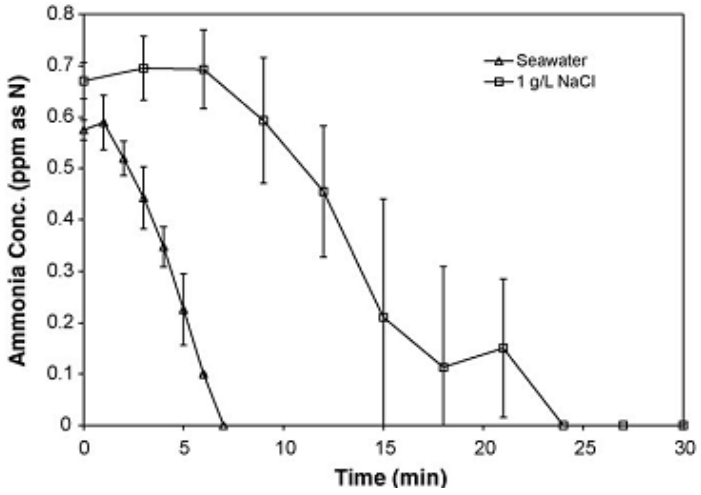

Figure 15: Ammonia removal from water within static test reactors as a function of water salinity. Photoanodes were coated five times with TiO_2 and fired at 300°C. Experiments were conducted in 100% seawater (Instant Ocean®) or freshwater containing 1 g/L NaCl with aeration using an applied voltage of +1.0 V. Initial concentration of ammonia was 1.6 mg/L NH_4Cl. Data shown are mean ± SEM (n=3).

2.2.6. Effect of pH

Ammonia removal rates in low-salt water (1 g/L NaCl) were identical over a range of initial pH values (i.e., 5, 7 and 10), indicating that ammonia oxidation by PECO is independent of pH (data not shown).

Ammonia in aqueous solution exists in equilibrium between the ionized (NH_4^+) and the non-ionized form (NH_3). The pK_a for this equilibrium is 9.3, and approximately 85% of the ammonia is in the NH_3 form at pH 10, whereas over 99% is in the NH_4^+ form at pH 5. We had hypothesized that the positively charged NH_4^+ ion would not be oxidized as efficiently as the neutral NH_3 molecule because NH_4^+ would be repelled by the positive bias on the photoanode surface. This hypothesis was not confirmed.

The lack of reaction pH dependence in the system suggests two possible hypotheses. The first is that ammonia removal does not primarily occur at the interface of the anode, but via a soluble intermediary such as hypochlorous acid, and that the potential bias creates a pH gradient near the surface, one region of which is at an ideal acidity for ammonia removal. An alternative hypothesis is that NH_3 reacts at the electrode surface to form N_2 gas, the NH_4^+/NH_3 ammonia equilibrium shifts to form more NH_3, thus allowing the reaction to continue at the electrode. This seems less likely due to the strong dependence of ammonia removal reaction with chloride ion and the high concentrations of reactive chlorine species in the system as well as the pH dependence of the NH_4^+/NH_3 ratio.

2.2.7. Effect of applied voltage

We observed that (1) no ammonia was removed from water in the absence of an applied potential, and (2) the rate of ammonia removal increased with increasing potential (Fig. 5). These results can be explained by the physics of the PECO process. When light with sufficient energy strikes the surface of the TiO_2-coated photoanode, electron-hole pairs are produced. In the absence of an applied potential, these electrons and holes rapidly recombine, producing few useful chemical reactions. When an electric bias is applied, however, photogenerated electrons are readily transferred from the photoanode to the cathode. This decreases electron-hole pair recombination, and results in a greater oxidative potential at the photoanode surface as the

applied voltage increases.[143] Larger applied voltages also increase current density and the formation of oxidative intermediates.

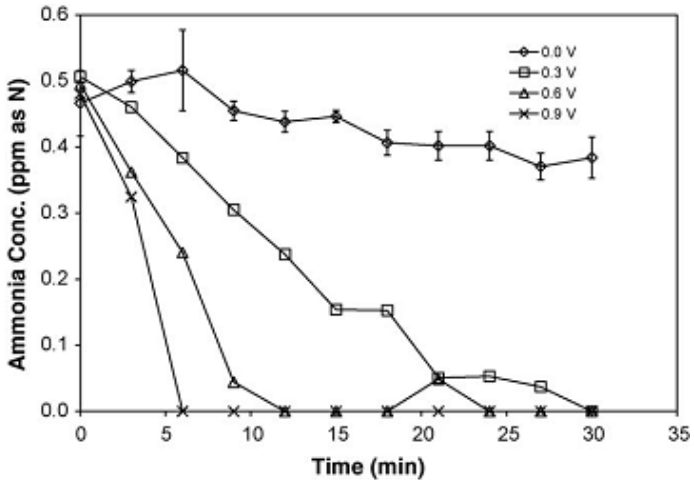

Figure 16: Ammonia removal from water in static test reactors as a function of applied voltage. Photoanodes were fired at 500°C. Experiments were performed in aerated freshwater containing 1.6 mg/L NH_4Cl in 1 g/L NaCl at pH 7. Applied voltage to the photoanode were 0, +0.3, +0.6, or +0.9 V with respect to the silver wire reference electrode. Data shown are mean ± SEM (n=4).

Product formation was not influenced by the applied potential. Little or no ammonia-nitrogen was converted to nitrite-nitrogen at any applied voltage, and approximately 13% of the ammonia-nitrogen was converted to nitrate-nitrogen, regardless of the applied voltage (Table 4). The data suggest that ammonia (oxidation state = -3) is primarily oxidized to nitrogen gas (oxidation state = 0) rather than being oxidized more fully to nitrite (oxidation state = +3) or nitrate (oxidation state = +5). These observations are also compatible with a mechanism of action involving hypochlorous acid oxidation of ammonia to nitrogen gas.

Table 4: Formation of nitrate and nitrite after 30 min of testing at different applied voltages under the same test conditions used to generate data in Figure 6. The standard error for four replicate measurements is given in parentheses below the measured value.

Applied Voltage (V)	Initial ammonia conc. (ppm as N)	30-min nitrate conc. (ppm as N)[1]	% nitrogen as nitrate	30-min nitrite conc.(ppm as N)	% nitrogen as nitrite in system
0.0	0.60±0.13	0.024±0.006	4.0	0.054±0.002	9.0
0.3	0.65± 0.02	0.087±0.008	13.4	0.014±0.028[2]	2.2
0.6	0.64± 0.04	0.080±0.004	12.6	0.000	0.0
0.9	0.62±0.06	0.084±0.006	13.6	0.000	0.0

[1] The test solution had an initial nitrate concentration of approximately 4 ppb as N.

[2] This value is based on one measurement above non-detectable levels. Three other replicate measurements for this photoanode formulation were non-detectable for nitrite.

2.2.8. Effectiveness of 2-electrode PECO device

Three electrode systems may be unnecessary for practical devices utilized in commercial applications, and therefore, we tested the efficacy of a 2-electrode reactor. As predicted, ammonia removal was as effective in the 2-electrode configurations as it was in the 3-electrode configuration when the voltages between the anode and cathode were similar (data not shown).

2.3. DEMONSTRATION STUDIES WITH FLOW-THROUGH PECO PROTOTYPE

The removal of ammonia-nitrogen (0.7 ppm) from 7 L of seawater was investigated using a flow-through PECO device. Complete removal of ammonia was observed in 90 min (Figure 17).

Experiments were conducted with live fish in seawater to compare the production of ammonia, nitrite and nitrate between aquaria equipped with (1) flow-through PECO devices fitted with activated carbon to chemically remove excess chlorine and bromine, and (2)

commercial biofiltration units (Marineland Penguin BIO-Wheel, Model PFO100B). The biofilters were previously cycled and had mature populations of nitrifying bacteria. Replicate 18-L glass aquaria of each treatment (2 PECO systems and 2 biofilters) were stocked with two ~5 g seawater-adapted tilapia. The fish were fed at 3% of body weight once daily. Ammonia, nitrite, and nitrate concentrations were monitored daily for 11 days in each tank. In the aquaria equipped with biofilters, nitrate concentrations (N as NO_3) began to increase steadily after one week, reaching over 14 mg/L by day 11 (Figure 18). In contrast, nitrate levels did not increase in the aquaria equipped with the PECO units. These observations illustrate a principal advantage of using PECO technology for ammonia removal in closed systems – the absence of nitrate accumulation as the ammonia-nitrogen produced by fish metabolism and the breakdown of uneaten feed and feces is converted primarily into nitrogen gas, not nitrate.

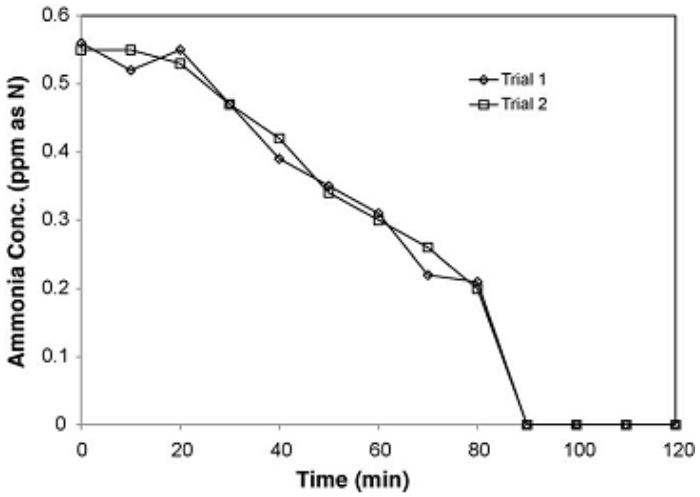

Figure 17: Ammonia removal from seawater in a 7-L aquarium using a flow-through prototype PECO device with a 9-W lamp. Initial ammonia concentration was 1.6 mg/L NH_4Cl. Each curve represents one independent trial. Applied voltage was +1 V between anode and reference electrode (+2.2 V between anode and cathode).

The results suggest that it may be possible to build a practical PECO ammonia removal device for use as a replacement or adjunct to biofiltration in home aquariums and recirculating aquaculture systems. Earlier studies had shown adequate removal in photocatalytic systems only under very specific conditions, i.e. high intensity ultraviolet illumination and at an ideal pH level, but these results hint at a much more robust and low cost application of PECO for aquatic systems. An ammonia removal device that does not rely on bacteria could have important advantages over biofiltration. For example, it will be possible to immediately add fish into new systems without waiting for nitrifying bacteria populations to become established on new filters. Systems could also be used intermittently as there is no requirement to keep bacteria populations alive during system down time. It will be possible to treat sick fish with antibiotics applied to the water without the risk of killing the beneficial bacteria on the biofilters. The lack of nitrate accumulation in the water may reduce the frequency of water exchanges and prevent the growth of nuisance algae. Finally, the energy costs to run the PECO units will be similar to using germicidal UV systems of the same size.

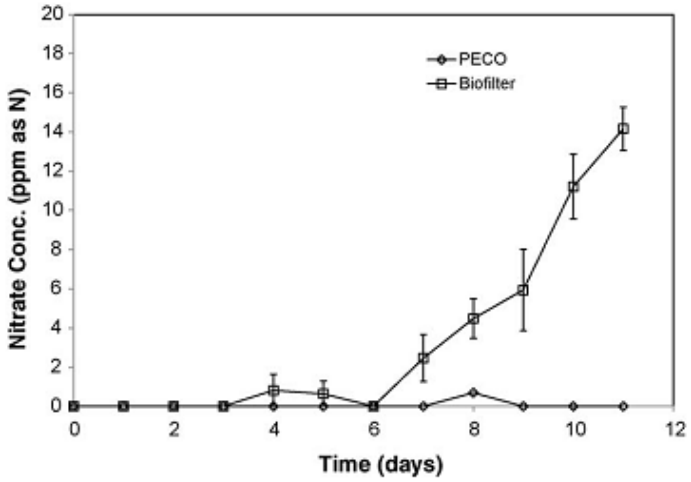

Figure 18: Nitrate concentration in a live fish system, each consisting of an 18-L tank of seawater that holds two 3-inch tilapia (~5g/fish). Tilapia were fed with 45% protein trout feed at 3% of body weight once per day (~0.6 g of feed per day). Each tank is fitted with either the prototype PECO reactor or a commercial biofilter (Marineland Penguin Biowheel). Data shown are mean ± SEM (n = 2)

There are key problems that must be addressed before PECO can become commercially viable. First, it remains to be demonstrated that the technology can be scaled for use in larger aquaculture systems stocked with commercial densities of fish. Second, during prolonged use in hard water or seawater, severe cathode scaling (i.e., the deposition of $CaCO_3$ and $MgCO_3$) can occur.[152] Solutions to this problem include periodically descaling the cathode with acid, and using innovative cathode configurations that resist scaling. Third, the generation of chlorine could be a major problem if "breakthrough" occurs and residual chlorine accumulates in the water. In small aquariums systems, this problem can be solved using activated charcoal, which is very effective at removing chlorine from water. In larger systems, UV light can be used to eliminate hypochlorous acid, and real-time chlorine sensors can be used to control the PECO reactors to prevent chlorine breakthrough. Fourth, as can occur with ozonation and electrolysis of seawater, toxic

by-products such as trihalomethanes might be produced by PECO reactions under some conditions. One advantage of PECO in this regard, however, is that by-product formation can theoretically be controlled by varying the applied potential, although this has yet to be investigated in our system. Moreover, Katayose et al.[151] recently investigated the by-products produced by the electrolysis of seawater and showed that only low levels of trihalomethanes were produced. For example, the electrolysis of seawater to produce residual chlorine concentrations of 4.3 mg/L produced total trihalomethane concentrations that were only 10% of the drinking water standards of the U.S. and Japan (9-12 ppb bromoform).

The PECO method may not only be useful for denitrification, but also for disinfection in various aquaculture applications. For example, as has been demonstrated using electrolytic systems, PECO could be used to generate oxidizing agents in situ to disinfect (1) intake seawater for hatchery systems,[153] (2) aquaculture wastewaters prior to discharge,[154] and (3) tanks, nets and other aquaculture equipment.[155] PECO has several advantages over electrolysis as a method to oxidize impurities in water. PECO combines the disinfection capabilities of both UV and hypochlorous acid generation, it uses far less expensive and longer-lasting electrodes than those typically used in electrolytic systems,[144,156,157] and uses less electricity than electrolysis because the photoactivated anodes used in PECO can produce high currents at relatively low voltages.

2.4. Conclusions

The key variables mediating the catalytic efficiency of the ammonia conversion reaction were anode preparation, applied potential, and salinity of the treated solution. The rate of the ammonia removal reaction was not affected by the pH of the solution. Nitrogen mass balance analysis indicated that at least 85% of the ammonia was converted into nitrogen gas. The remainder was primarily converted into nitrate with low levels of nitrite and chloramines sometimes detected. Additional research is needed to address remaining problems with PECO technology, although the data supports the possibility that PECO could become an alternative to biological filtration for ammonia removal from aquatic systems.

3. Application of Photoactive Thin Films as a Curing Compound

3.1. Overview of Concrete and Curing Compounds

Concrete is the most widely employed construction material, with usage rates exceeding 1m^3/person globally.[158] Global production of Portland cement for concrete has fallen with the downturn in the global economy, but still exceeds 3.06 billion metric tons.[159] Per capita concrete usage rates peak as an economy develops and produces more infrastructure and then decreases as per capita GDP increases. Therefore, emerging economies such as India, China, and Pakistan are expected to dramatically increase their concrete consumption as they develop infrastructure.[158]

Cement production is highly energy intensive and releases approximately 900kg CO_2 for every 1000kg cement, making concrete production one of the primary CO_2 emission sources.[159] The release of CO_2 during cement production is partially due to the high temperature required and partially due to the chemical conversion of the raw materials. As they are a chemical by-product, these emissions are nearly fixed for a given quantity of cement produced, which leaves little room for dramatic improvement. It is vitally important to decrease the global consumption of concrete if CO_2 emissions are to be reduced. Assuming that emerging economies will demand infrastructure similar to that of industrialized nations, the primary avenue of decreasing the consumption rate is by improving the service lifetime of the concrete infrastructure.

The performance of concrete structures depends largely on the mix design used in construction, which relies on the careful balancing of numerous variables.[160] Concrete is a superficially simple material, typically composed of hydraulic cement (typically Portland cement, fly ash, slag, or some mixture of these components), a fine aggregate (sand) fraction, a coarse aggregate (stone, reclaimed material, or other) fraction, reinforcement (steel rebar), chemical admixtures (water reducers, accelerators, etc.), and water. The type and ratio of these

components controls the early age properties of the concrete slurry, such as slump, entrained air content, unit weight, and curing behaviors like time to initial set and heat of hydration. After the concrete has been placed and finished, the initial mix design continues to determine the strength, longevity, and aesthetics of the concrete product.

Ordinary Portland Cement (OPC) serves as the binder in the vast majority of concrete. It is manufactured from quarried or reclaimed limestone and shale processed in large rotary kilns. Each of the many steps involved in the production of OPC consumes large amounts of energy. Quarrying, grinding, and mixing operations each require significant amounts of mechanical energy, but the most energy intensive process is the chemical conversion of these minerals. Finely powdered limestone, shale, and gypsum are introduced into a rotary kiln, where they are heated to *ca.* 1450˚C in a reducing atmosphere. As this heating occurs, several chemical transformations take place. The limestone and clay-like minerals are decomposed into their constituent oxides (principally CaO, SiO_2, and Al_2O_3) and CO_2. These products then react to form the dicalcium and tricalcium silicates and aluminates that largely comprise OPC. Cement manufacture accounts for over 5% of the global anthropogenic carbon dioxide emissions due to the high

demand of concrete, the energy required to produce it, and the presence of CO_2 as a reaction by-product.[161]

A typical composition of OPC with respect to these metal oxides is shown in Table 5:[162]

Table 5: Approximate typical composition of Ordinary Portland Cement

Cement Compound	Weight Percentage	Chemical Formula
Tricalcium Silicate	50%	Ca_3SiO_5 or $3CaO{\cdot}SiO_2$
Dicalcium Silicate	25%	Ca_2SiO_4 or $2CaO{\cdot}SiO_2$
Tricalcium Aluminate	10%	$Ca_3Al_2O_6$ or $3CaO{\cdot}Al_2O_3$
Tetracalcium Aluminoferrite	10%	$Ca_4Al_2Fe_2O_{10}$ or $4CaO{\cdot}Al_2O_3{\cdot}Fe_2O_3$
Gypsum	5%	$CaSO_4{\cdot}2H_2O$

3.1.1. Concrete Curing

The hydration reaction of cement has been studied extensively and can be summarized as shown in Equation 4 and Equation 5. Equation 4 is the hydration of tricalcium silicate to calcium silicate hydrate (CSH) and calcium hydroxide (CH). Equation 5 is the hydration of dicalcium silicate to CSH and CH

Equation 4: TCS to CSH

$$2\ Ca_3SiO_5 + 7\ H_2O \text{ ---> } 3\ CaO{\cdot}2SiO_2{\cdot}4H_2O + 3\ Ca(OH)_2 + 173.6kJ/mole$$

Equation 5: DCS to CSH

$$2\ Ca_2SiO_4 + 5\ H_2O \text{ ---> } 3\ CaO{\cdot}2SiO_2{\cdot}4H_2O + Ca(OH)_2 + 58.6.6kJ/mole$$

Other hydration reactions occur, but do not contribute greatly to the long-term strength of concrete.[163] The reactions outlined in Equation 4 and Equation 5 consume large amounts of water and occur at the interface of the solid phase cement particles and liquid phase pore water. The ratio of water to cement particles (W/C ratio) influences both the early and long-term properties of the concrete. The stoichiometry of the hydration reactions suggests that a W/C ratio of 0.42 by weight provides sufficient water to completely hydrate the cement particles. In practice, other W/C ratios are used to meet regulatory and performance targets.

The amount of liquid water present in the mortar (the mixture of water, sand, and cement) dictates several early-age concrete properties. Workability describes the rheology of the concrete at an early age, before the mortar (sometimes referred to as cement paste) has taken an initial set, and is principally determined by the W/C ratio or addition of chemical admixtures. Highly workable concrete contains mortar with low viscosity, which allows the concrete mixture to consolidate easily in any molds, forms, or placing equipment and also allows concrete workers to bring a thin layer of mortar to the surface for finishing. The slump value of a concrete mix is used as an estimator of workability, and is often prescribed by the end user of the concrete mixture.

Highly workable concrete may be useful when filling a complex form with narrow spacing or for a hand laid slab. However, this type of concrete would not be suitable for continuous paving or curbing machinery.

By increasing the W/C ratio to improve workability, one can induce dramatic effects on the later properties of the concrete product. Cement mortar consists of small particles of the hydraulically active cementitious material, active fine material from the aggregates, inert fine material from the aggregate, and any inert filler, surrounded by water in the pore space. As the hydration reaction occurs and consumes water the pore space becomes a void. This void space contributes nothing to the strength of the concrete and decreases the volumetric density and therefor strength of the concrete. The volume of the hydration products is less than that of the water initially present, so cement mortars shrink autogenously as hydration occurs, primarily at early ages before the initial formation of a gel network. This leads to an internal stress that can increase the percolation (interconnectedness) of the final concrete pore network. Further shrinking occurs when water evaporates from hardened concrete near exposed surfaces, leading to cracking, warping, or other mechanical damage.[164] Percolated voids can fill with water or de-

icing solutions and will substantially decrease the concrete's resistance to freeze/thaw cycling. Water reducing admixtures (plasticizers and superplasticizers) can be added to improve the workability of the concrete slurry without increasing the W/C ratio. However, these admixtures complicate mix design and may affect strength and scaling resistance at high concentrations.[4,165] Additionally, excess water not bound in pores will migrate to the concrete surfaces as "bleed water" and can delay finishing operations and increase the likelihood of forming a percolated network of surface pores.[166]

Finishing operations like trowelling and texturing should begin after bleeding is finished. Finishing operations disrupt the channel network created by bleeding, decreasing the percolation of the pore network and minimizing deleterious effects of porosity. Finishing can force bleed water back into the mortar and cause an increase in the W/C ratio near the surface and a marked loss in concrete durability. Determining the end of the bleeding period is challenging. Highly evaporative conditions can cause the surface to appear dry even though substantial bleeding is still occurring. Application of a membrane to this surface will halt evaporation and result in a thin layer of water underneath the membrane. This leads to membrane separation, membrane

pinhole formation, or crazing of the membrane. Once the surface is finished the concrete shape is defined and will be ready for use after the concrete cures.

Simply adjusting the mass of water in relation to the mass of cementitious materials is not enough to control the hydraulic environment of cement particles in the cement paste. Other concrete components can affect the apparent W/C ratio in the concrete pore volume. Coarse and fine aggregates physically adsorb water from the cement paste, swelling clays present in the aggregate chemically adsorb water, and hydration (pozzolanic) reactions can occur with the microfine fraction of the coarse or fine aggregate. These interactions will decrease the apparent W/C ratio and can lead to internal dessication.[163] In addition to these internal sources of water loss there is the added complication of evaporation. The hydraulic behavior of all of the concrete components and evaporation must be taken into account when considering mix design. Drying that occurs near an interface (between the cement paste and aggregate or at an atmospherically exposed surface) causes the formation of moisture gradients. The surface tension of water in pores causes large stress gradients in response to moisture gradients and can lead to cracking or decreases in scaling resistance. This is particularly a problem in concretes used for paving or

sidewalks that have high surface area to volume ratios, and in concretes with a low W/C ratio (0.4 or less)[164].

3.2. Control of Hydraulic Environment via Organic Curing Compounds

Membrane-forming curing compounds (MFCCs) are used to slow or halt the loss of capillary water to the atmosphere. These compounds are typically hydrophobic membrane forming polymers composed of a polymer fraction and a solvent or carrier fraction. MFCCs are normally composed of an emulsion of wax or resin in water (for low VOC formulations) or a solution of an organic membrane-forming compound in a suitable organic solvent. The most widely used curing compounds are comprised of an emulsion of paraffin wax, poly-α-methylstyrene resin, or mixed virgin and boiled linseed oil in water. Curing compounds used for pavements in Wisconsin are required to include a white pigment to increase the albedo of the pavement surface and thereby reflect heat from the exposed surface. Linseed oil or wax emulsions are widely used due to their low cost, high availability, and considerable historical momentum in the construction industry and among regulators. Recent studies performed for the Minnesota DOT found that these legacy MFCCs are less effective than newer materials, especially in challenging weather.[167] A coating compound containing 100% polyalphamethylstyrene (PAMS)

emulsion in water was found to be most effective at preventing evaporation and has been specified for all pavements in Minnesota. Research performed for the Wisconsin DOT has found that PAMS based MFCCs may not be effective in concretes using large fractions of supplemental cementitious materials like fly ash or slag.

These compounds form a physical membrane that prevents the evaporation of free water in concrete. The effectiveness of these compounds depends on the integrity of the membrane, so membrane application technique is important for proper performance. If the concrete material is still producing bleed water, the membrane may contain pinholes or separate from the concrete surface and fail to prevent evaporation.[6] Concrete surfaces used for roadways are typically finished with an aggressive texture applied to provide adequate traction and decrease roadway noise produced by tires.[168] This increases the surface area and accelerates the rate of water evaporation from the surface. These textures increase the difficulty of forming a continuous membrane, and spraying rates must be adjusted for the actual surface area, which may be several multiples of the simple geometric surface area.[8, 9] The increase in surface area must be considered when applying any type of curing compound, and the sprayer should pass both parallel and

perpendicular to the pavement texture to ensure that the MFCC coating is continuous. This slows concrete finishing operations and increases the capital and marginal expense of pavement operations.

Organic curing compounds on roadways are exposed to solar radiation and other environmental factors that will decrease the lifespan of the membrane. For Ordinary Portland Cements the curing period is typically completed before the membrane loses functionality. However, the loss of the membrane precludes the possibility of providing potentially beneficial long-term sealing of the concrete surface. Sealing can prevent chloride ingress, carbonation reactions, and causes a decrease of surface porosity. Concrete mixes that utilize a different cement or cement mixes, or those which rely on slower pozzolanic reactions for strength, require longer curing times and may not be adequately cured before the MFCC coating is degraded to the point of losing effectiveness. For pavement operations that require white-pigmented MFCCs the white pigment is often powdered titanium dioxide.[10] Titanium dioxide possesses the well documented ability to photocatalytically oxidize organic compounds and may hasten the destruction of the organic membrane. Although these reactions decrease the lifespan of the

membrane they may potentially treat vehicle-sourced VOCs and NO_x (Volatile Organic Carbon and mixtures of nitrogen oxide compounds).[169]

3.2.1. Control of Hydraulic Environment via Inorganic Curing Compounds

Sol-gel derived inorganic membranes are applied as low-viscosity stable suspensions of nanoscale particles of ceramic materials in some carrier, typically water. The stability of the sol suspension is a function of the charge on the surface of the individual particles and the ionic strength of the carrier. The charged surface of the particles forms an electric double layer in solution, thereby preventing interaction between individual particles and subsequent agglomeration or settling. If the double layer thickness decreases past a critical threshold, the sol will form a gel, a semi-solid network of connected particles with a high degree of water entrapped in this matrix. There are several methods by which the sol suspension can be made to form a gel. Removal of the carrier fluid by evaporation or some other method (osmosis, chemical reaction, adsorption) to below a critical concentration of particles forces the particles into close proximity despite their surface charge. Alternatively, changing the pH of the sol to near the isoelectric point of the particle decreases the surface charge and collapses the double layer.

Another possibility is increasing the ionic strength of the solution, as the double layer thickness decreases as seen in Equation 6.[170]

Equation 6: Debye screening length for determining approximate double layer thickness and suspension stability

$$\boldsymbol{\kappa^{-1}} = \sqrt{\frac{\boldsymbol{\varepsilon\varepsilon_0 k_B T}}{\sum_1^i \boldsymbol{n_i z_i^2 e^2}}}$$

Where κ^{-1} is the Debye screening length, n_i and z_i are the concentration and valency of the *ith* ion species (in units of number density m^{-3}), T is the thermodynamic temperature, k_B is the Boltzmann constant, *e* is the natural number, ε is the dielectric constant of the solvent, and ε_0 is the permittivity of free space. Once the ionic strength increases enough to decrease the double layer thickness past a critical threshold the particles are then free to interact and form a gel network.

The particulate nature of sols imbues the membrane with unique properties. The membranes formed are porous or mesoporous thin layers (nanometer to micron thickness) of metal oxide or other ceramic particles. The porosity of the membrane is due to the packing of the particles. Packing density, particle size, particle size distribution, and particle shape control porosity, pore size, and pore size distribution of the resulting membrane. The particle size, size distribution,

chemical nature of the particles, and the shape of the particles in the suspension can be controlled by choosing the proper precursor chemicals, solution chemistry, reaction environment, coating environment, and temperature. Engineering of the pore space can be accomplished by controlling these parameters and affords the researcher the ability to change the behavior of the coating.[171] Additional control of the membrane properties is possible by introducing a sintering step, where high temperature or ultraviolet radiation are used to increase the density and hardness of the membrane, which may increase the pore size and decrease the total pore volume.[172] For concrete applications only UV sintering is realistic, as temperatures sufficient to markedly affect the properties of the membrane would destroy the concrete substrate.

Membranes with small pores and a small pore volume can block the passage of water by primarily physical action, and the evaporation rate should be less influenced by the hydrophobicity of the membrane surface. Considering a spherical particle with a narrow particle size distribution, minimum porosity will occur when the particles are hexagonally close packed.[163] This will result in a material with a percolated network of pores and a void fraction of 0.26. Preparation of this membrane would involve precise deposition of equally sized particles, which

is most likely to occur when particle deposition is quite slow and pore area minimization is thermodynamically favorable. Random packing, as would occur with rapid particle deposition of equally sized particles, will result in increased porosity of a less percolated nature. If the particle size distribution is less tightly controlled, the degree of porosity and pore size distribution can be controlled to a greater degree. An example is a bimodal particle size distribution with very small particles filling the pore space between larger particles. Pore structure can also be controlled by changing the shape of the particles, as would be the case for coatings prepared with nanorods, nanowires, dendritic particles, or other exotic shapes. For instance, a superhydrophobic membrane composed of vertical nanorods might exhibit the self-cleaning "lotus flower" effect, and prove resistant to water migration even with a very high porosity.[173]

In addition to controlling the physical properties of the coating it is possible to control the chemical nature of the membrane surface and the pore space. Every material has an associated chemical potential in bulk, and these potentials are often quite different for different physical phases. At an interface, thermodynamic equilibrium dictates that the chemical potential is equal, which occurs at a level somewhere intermediate to the potential of the two bulk materials.

Typically, the effects of a chemical potential mismatch occur within a few angstroms to several nanometers of the interface and extend farther into the more mobile phase. All interfaces have an energy associated with equalization of the chemical potential of the two materials. As water is a polar molecule, this energy is small for materials with high surface energies and larger for materials with low surface energies (i.e. those solids like Teflon in which the primary cohesive force is due to van Der Waals interactions). It is possible to control the surface charge and therefore surface energy of metal oxide coatings by changing the pH. A pH near the isoelectric point of the material minimizes the surface charge and maximizes the hydrophobicity of the surface, while a surface pH far from the isoelectric point will maximize wetting. Just as there is a potential (analogous to voltage) associated with the interface of a surface, there is a potential field on the walls of a pore. Pore diameters of the same size domain as the interfacial gradient will have a potential extending across the entire pore diameter. If this potential is similar in sign to the potential of an ion the pore will exclude that ion from the pore space and prevent transmission across the membrane. This is the basis for nanofiltration,[174] but in the context of concrete curing may allow highly porous hydrophobic membranes to prevent the transmission of

molecules with a large dipole, such as water vapor. Likewise, hydrophilic pores may strongly interact with water molecules and prevent flux of water across the membrane, decreasing the rate of evaporation by tightly binding water in the pore.

Metal oxide membranes are ceramic materials and are typically as hard or harder than the material on which they are supported. They are not degraded by environmental processes and are stable across a wide range of solution pH and chemistry. They are also strongly bonded to their substrate and can self-harden or harden under ultraviolet exposure. The long environmental life and strong bonding of these materials mean that the beneficial properties of the membrane last much longer than the initial curing period, and may impart beneficial characteristics to the pavement long after traditional MFCCs have degraded. Additionally, the beneficial characteristics of the nanoparticles may extend some distance into the concrete material if the diffusion velocity of the particles in the pore water exceeds the migration rate of bleed water to the surface.

3.2.2. Additional modification of cement properties via nanoparticulate application

There have been numerous nanoparticle sols developed from a variety of ceramic materials. These materials may improve the performance of concrete via pathways other than evaporative control. Metal oxide thin films have been used in photocatalysis for the treatment of volatile organic compounds (VOCs) or other environmentally troubling anthropogenic emissions (nitrogen oxides, ozone).[169] They are self-cleaning under exposure to sunlight. They have been used for corrosion control or as anti-fouling coatings.[175] The high hardness of ceramic membranes is used in cutting tools to increase blade life and decrease wear. They have been used for ion exclusion in nanofiltration processes. They can also be engineered to have a high albedo and decrease the "heat island" effect associated with large paved surfaces.

Extremely high performance (>15000 psi compressive strength) concretes can be manufactured by adding silica fume (high surface area/small particle size silica particles) to the cement fraction.[176] Silica fume consists of sub-micron amorphous silica particles and provides additional strength at an early age by improving the packing of particles in the mortar, especially near aggregate particles.[177] The very small particles fill the space between cement particles and improve density by decreasing the pore space. In addition, it provides long term strength gain by

chemical (pozzolanic) reactions with calcium hydroxide in the pore space.[178] Typical pavements do not require the high compressive strength of silica fume modified concrete but may benefit from the increase in density provided by small silica particles near the exposed surface. Sol-gel derived nanoparticle of silica are much smaller than those in silica fume ($2\text{-}3\times10^{-9}$ m as opposed to $2\text{-}10\times10^{-7}$ m) and have a proportionally greater surface area. At the relevant pH of cement pore water (10.5 to 13) silica is soluble, but the dissolution process is kinetically limited for large particles.[179] Silica can react with CaOH to form CSH paste, decreasing the CaOH concentration and decreasing the pore volume of the concrete. Increasing the surface area of the silica particles will improve the dissolution kinetics and increase the rate of formation of CSH paste in the pore space. If the IMFCC contains a significant amount of silica nanoparticles and is applied while the material is producing bleed water or has not achieved initial set then the CSH gel at the surface will be denser and have lower porosity. This may impart beneficial properties to the near surface, including decreased water infiltration, decreased percolation of the pore network, decreased susceptibility to chloride penetration, and improved wear resistance.

One potential benefit of these materials is preventing the ingress of chloride ion or potentially harmful alkali species. Nanofiltration is a potential technology for desalination of mildly brackish waters that relies on the overlapping surface potential in the pore space of a ceramic thin film. A nanoscale pore with a positive surface charge will exclude positively charged ions from traversing the pore. The opposite is true for negatively charged surfaces. If an ionic compound is in solution the principle of solution electro-neutrality requires that the positive and negative charges cancel completely. Therefore, excluding a positive ion from traversing a membrane necessitates that the negative ion also not traverse the pore. There has been research efforts focused on understanding this effect and using it to exclude moderate concentrations of ions for water purification.[174] If IMFCCs reject chloride ions they may serve to prevent chloride ion associated concrete failure, reducing the corrosion of reinforcing bars and to mitigate surface scaling. By preventing the ingress of chloride, IMFCCs might also exclude alkali metal ions associated with alkali silica reactions (ASR) or other alkali-aggregate reactions (AAR).

It is possible to prepare mixed metal oxide sols that allow for simultaneous evaporative control and modification of the concrete surface to control pollution. Much research has been

devoted to the use of photoactive titania for oxidation of VOCs, NO_x, inorganic carbon, and organic dyes. Photocatalytic reactions can also de-activate bacteria, bacterial spores, or viruses. When a particle of titania is illuminated with a photon of sufficient energy (3.2 eV or more) an electron is promoted from the valence band to the conduction band and an electron/hole pair is created. If the hole interacts with a compatible molecule then a short lived radical species is formed. These species are strongly oxidative and will degrade environmental contaminates including VOCs, NO_x, SO_x, carbon black particulates, and biological molecules. These oxidative reactions are what differentiates self-cleaning glass and justifies the price increase to drive their sales. It is also the basis for several air cleaning products for the home, commercial spaces, and industrial applications. Several research groups and corporate interests are currently investigating the use of these properties, but largely only in the context of adding nanoparticles to the cement paste or applying thin layers of mortar impregnated with titania particles.[175,180] These methods are inefficient uses of expensive nanoparticles, which increases material cost or requires additional construction effort. Applying the active material directly to the surface ensures that the majority of the particles are exposed, illuminated, and active.

3.3. Experimental Study

Concrete specimens were prepared from three cement types and two aggregate sources and cured using membrane forming curing compounds as evaporative control. The specimens were tested for scaling resistance, resistance to chloride ion penetration, and resistance to damage from carbonation reactions. The effectiveness of the curing compounds at preventing evaporation was also tested. An example weighted decision matrix is provided to aid curing compound specification by design engineers.

Concrete used as pavement in continental climate patterns will be exposed to freezing and thawing conditions. During winter months deicers may be used to lower the freezing point of water on the surface to keep the pavement surface free from ice.[181] The high ionic strength of the deicer solution on the surface, the expansive nature of ice formation, and chemical reactivity between the deicer solution and concrete components can lead to substantial internal tensile stresses and result in spalling type failure of the finished mortar layer. In addition to the obvious pavement deterioration, scaling impacts aesthetics, ease of cleaning and snow removal, surface traction, and traffic noise.[182–190]

Scaling resistance testing was performed on specimens prepared from several concrete blends, several coarse aggregate mineralogies, and treated with several MFCC formulations including a novel mixed metal oxide nanoparticulate hydrophilic membrane to quantify suitability for use in mid-latitude environments with annual freeze/thaw events. This testing was supplemented with chloride ion penetration analysis, and carbonation depth analysis. An example weighted decision matrix was populated with these data to systematize curing compound selection.

3.3.1. Materials, Sample Preparation, and Testing Methods

3.3.1.1. Concrete Materials

The concrete prepared for this study consisted of a cementitious binder, a coarse aggregate fraction, and a fine aggregate fraction. The cementitious materials were either Type (I) OPC or a blend of 30% (w/w) Grade 100 ground granulated blast slag or Class C fly ash (FA) in OPC. The total cementitious material content was 470.0lbs/yd^3 (278.8 kg/m^3) and the coarse aggregate/fine aggregate/cementitious material mass ratio was 3.3:2.2:1. The coarse aggregate fraction was graded stone with a maximum diameter of 1in. (25.4mm), either crushed limestone or predominantly igneous gravel. A single source of fine aggregate was used. A water-to-

cementitious material (w/cm) ratio of 0.40 was used for OPC and GGBS concretes but was reduced to 0.37 for FA-cement blends to meet slump requirements. Low range water reducing admixture (LRWRA) was added as needed to meet the slump requirement of 3±1 in. Air entraining agent (a common synthetic polymer type) was added as needed to entrain 6±1% air.

The crushed limestone coarse aggregate had an aspect ratio of approximately 2:1 length to diameter. The gravel aggregate contained several mineral types including granite, basalt and a minor fraction of dolomite with an aspect ratio of approximately 1:1 length to diameter. The fine aggregate was graded sand from a single source. All water used in mixing was municipally treated drinking water at 13˚C (55˚F). A total of 6 mix types were prepared and multiple samples of each mix were treated with 5 curing compounds for a total of 30 treatments.

Table 6 shows the concrete mix designs and properties. Forms were non-absorbent cylinders treated with form release agent.

Table 6 Fresh concrete properties and compressive strength

Mix	SCM Type	Coarse Aggregate Type	w/cm Ratio	Avg. Slump Inches	% Air	28 Day Comp. Strength PSI
1	None	Limestone	0.40	2.44	5.2%	4590
2	Fly Ash	Limestone	0.37	2.50	5.1%	5218
3	Slag	Limestone	0.40	2.19	5.3%	5447
4	None	Gravel	0.40	2.15	5.3%	4707
5	Fly Ash	Gravel	0.37	2.63	5.8%	5097
6	Slag	Gravel	0.40	2.65	6.0%	4948

3.3.1.2. Curing Compounds

The physical and chemical properties of the tested MFCCs are presented in Table 7. Wax (Wax), linseed oil (Lin), and poly-α-methylstyrene (PAMS) were emulsions of membrane forming organic compounds and white pigment in water. Pigmentation was specified by the DOT to increase the reflectivity of the surface, prevent thermal gradients arising from solar forcing, and aid in uniform application. The manufacturer stated that these emulsions are prone to separation during long-term storage and should be used within the specified shelf life.

Clear chlorinated rubber epoxy (CR), and clear acrylic (Acryl) MFCCs were solutions of membrane forming organic compounds in mixed organic solvents. These MFCCs were designed to form a membrane on the surface and also penetrate the pore network of the concrete to harden and seal it to prevent the ingress of air, water, or deicer solution. The organic solvent

evaporates and enters the atmosphere as VOCs. The compounds were solutions instead of emulsions and not expected to separate.

Organic solvents in the solvent based MFCCs introduced several important safety considerations to the application process. The low flash point reported in the MSDS for these compounds (<5˚F (-15˚C)) suggested that ignition is a concern under all realistic application conditions. All potential ignition sources were isolated from flammable vapors in the spraying area. Additionally, acute or extended exposure to organic vapors results in mental and physiological effects (e.g. central nervous system depression, respiratory disorders, or cancer). Spraying operations were performed outdoors to ensure vapor concentrations below flammable or explosive levels and to limit personnel exposure. A respirator approved for organic vapors and other appropriate personal protective equipment was used to further limit exposure.

Table 7: Membrane Forming Curing Compound Properties

Name	Solid Phase	Carrier	Solid Fraction	Color	Specific gravity	Membrane description	Odor intensity	Recommended Application Rate
Wax	Paraffin	Water	15- 25%	Brilliant white	0.97-1.03	Not reported	None	200ft^2/gal
Lin	Linseed oil	Water	40-50%	Yellowish white	0.97-1.03	67% reflect.	Medium	200ft^2/gal
PAMS	Poly-α-methylstyrene	Water	52.5%	Brilliant white	0.97-1.03	68% reflect.	Low	200ft^2/gal
CR	Chlorinated rubber Unspecified epoxy	Mixed xylenes Ethylbenzene	29%	Yellowish clear	0.97	Semi-gloss	High	300ft^2/gal
Acryl	Acrylic monomer Methacrylic monomer	Mixed xylenes Arom. distillates Trimethylbenzene Cumene	25%	Colorless clear	0.91	Gloss	High	300ft^2/gal
Nano	Nanoparticulate mixed metal oxides	Water	<1%	Colorless clear	1.0	Not Detectable	None	200ft^2/gal

3.3.1.3. Specimen Preparation

All concrete used in this study was prepared with a rotary drum concrete mixer in 2.5 ft^3 batches as per ASTM C192 methodology. Slump and air content were determined following test protocols ASTM C-143 and ASTM C-231 for each batch. Four 4 in. diameter by 8 in. cylindrical specimens were prepared for 28 day strength testing for each of the concrete mixes. Three replicate ASTM C672 specimens (12 in. diameter by 3 in. cylinders) and 4 replicate

AASHTO T259 specimens (8 in. diameter by 3.5 in. cylinders) were prepared for each concrete mix and each curing compound. Molds were filled manually in two lifts. Each lift was compacted with a steel tamping rod and consolidated by striking the form several times with a rubber mallet. After the second lift any excess material was struck from the form with a wooden strike off board. Mortar was floated to the surface with a wooden board utilizing the minimum amount of work required to cover all coarse aggregate particles. The specimens were then allowed to rest and bleed in the mold. A bleed period of two hours was specified as a standard that falls in the range of field construction practices. This period of time was insufficient to allow the complete evaporation of bleed water on the surface of some concrete blends prior to finishing emphasizing that different mixes will exhibit bleeding in different ways. The surface was finished with three sawing motion passes of a wooden board and textured with a medium stiffness brush before treatment with MFCC.

The order in which the specimens were treated with MFCC was randomized to minimize systematic artifacts. All MFCCs were applied to the surface using pressurized hand-held sprayers with nozzles chosen to provide smooth, even coverage. MFCC was applied gravimetrically by

placing the specimens on an electronic balance and masking the balance pan to prevent overspray from affecting the mass reading. MFCCs were applied with the nozzle of a hand-held sprayer perpendicular to the concrete surface. The aerosol spray pattern was swept across the surface in alternating directions until the desired mass of curing compound was applied. The mass applied resulted in a coverage rate of 204±13ft^2/gallon (5.01±0.32m^2/L) for all compounds.

ASTM C672 and AASHTO T259 specimens were left exposed to laboratory air at 45±5% relative humidity (RH) and 23±2˚C (73˚F). After 24 hours the specimens were removed from the form and the sides and bottoms were sealed with a low-viscosity, low-modulus epoxy to limit evaporation to only the MFCC treated surface. After a 28 day curing period in the laboratory, the specimens were transferred to a chamber maintaining 50±5% RH and 23±2˚C for 14 days. This second period allows wet cured specimens adequate time to dry and develop pore humidity similar to curing compound treated specimens. The specimens were fitted with a confining rim dam to contain a ¼ in. (6mm) pond of 4% (w/w) NaCl solution.

Compressive strength specimens were demolded after 24 hours and held in a chamber maintaining 25±2˚C and 100% RH until testing. At 28 days, the specimens were capped with

sulfur capping compound. ASTM C156 specimens were prepared by filling cylindrical forms, 6 in. diameter and 1 in. depth, with OPC mortar. Mortar mix design, mixing, and form filling technique were performed in accordance with the test method. Specimens were allowed to bleed for two hours before curing compound was applied.

3.3.2. Test Methods

3.3.2.1. Early Age and Compressive Strength

The early age properties (slump, percent entrained air, unit weight) were measured using test protocols ASTM C-143 and ASTM C-231 and the appropriate equipment. Strength cylinders were tested to failure for compressive strength.

3.3.2.2. ASTM C-672: Standard Test Method for Scaling Resistance of Concrete Surfaces Exposed to Deicing Chemicals.

The reservoirs on the sample surfaces created by the dams were filled to approximately ¼ in. (6 mm) depth with 4% w/w NaCl solution. The specimens were placed in a temperature controlled chamber programmed to provide -16°C (3°F) for 20 hours followed by 34°C (93°F) for four hours. The tops of the specimens were loosely covered with 6 mil polyethylene film to

prevent evaporation. After every fifth freeze/thaw cycle the specimens were removed from the environmental chamber and the deicer solution decanted over a #200 sieve. Any loosely adhering material on the specimen surface was rinsed off with a gentle stream of water and collected in the #200 sieve. The scaled material was dried at 50˚C (122˚F) in a laboratory oven and weighed with a digital balance precise to 0.01 grams. When it was necessary to repair or reinstall the dam, care was taken to ensure that no scaled material was lost and that the dam was reinstalled in the same position. The mass of scaled material was averaged over the three specimens. No standard for an acceptable quantitative mass loss in this test is specified for the USA, but values no greater than 500 g/m^2 (0.922lsb/yd^2) are specified for Canadian roadways, and Sweden specifies a loss rate no greater than 1000g/m^2 (1.84lbs/yd^2).[191]

3.3.2.3. AASHTO T-259 Modified: Method for Testing Resistance of Concrete to Chloride Ion Penetration

The deicer reservoirs were filled with 4% (w/w) NaCl solution to ½" depth. The specimens were stored at 23±2˚C and 50±5% RH and loosely covered with 6 mil polyethylene film to prevent evaporation. Every 7th day the deicer solution was replaced to prevent changes in the

solution concentration. After three months of deicer coverage, specimens were rinsed liberally with fresh water and the top millimeter of the specimen surface was removed by grinding. Pulverized powder samples were collected for each specimen from five locations on the surface by drilling. Material was collected at a depth from 1 mm (0.04 in.) to 13 mm (0.5 in) at 5 widely separated locations. A second sample of material was collected at a depth from 13 mm to 25 mm(1 in.) in the same 5 locations. The powdered samples were passed through a #16 sieve to remove any large particles and stored in polypropylene centrifuge tubes until analyzed.

Powdered concrete from each depth region was digested with boiling nitric acid solution. Any sulfur was removed by addition of a small volume of 30% H_2O_2 to the digesting solution. An aliquot of the digesting solution was diluted and analyzed by ion chromatography. This method is capable of quantitative analysis at sub-ppm resolution, is automated, and more rapid than electrochemical methods.[192–195]

3.3.2.4. ASTM C-156: Standard Test Method for Water Loss from a Mortar Specimen through Liquid Membrane-Forming Curing Compounds for Concrete

Mortar specimens were prepared from OPC and the same fine aggregate as those used for the concrete specimens. Curing compounds were sprayed onto the specimens at a coating rate of 200 ft^2/gallon. The specimens were weighed, coated with curing compound, reweighed, and inserted into an environmental chamber at 100.0±0.5˚F and 32±0.5% relative humidity. After 3 days, the specimens were reweighed and the mass loss was adjusted for evaporation of the MFCC carrier phase.

3.3.2.5. Carbonation Depth

The resistance of the hydrated mortar to damage from carbonation reactions was tested using an accelerated test procedure. The specimens prepared and tested during ASTM C156 experiments were placed in a 100% CO_2 atmosphere for 1 month. The specimens were then broken and a 1% phenolphthalein solution was sprayed on the freshly broken surface. Carbonation depth was measured as the distance from the exposed surface to the depth at which the phenolphthalein solution turned pink due to high pH. This provides a qualitative comparison of the resistance of the concrete mortar to carbonation. The 100% CO_2 atmosphere used in this test was not humidified, and humidity is known to affect the rate of carbonation

reactions.[196] This shortcoming prevents direct comparison of carbonation results with other research projects but provided rapid results.

3.3.3. Results

3.3.3.1. Curing Compound Application

High viscosity formulations required specific nozzle design and greater pressure to atomize sufficiently to provide smooth coverage and an acceptable spray pattern. PAMS based MFCC was the most difficult to atomize. Linseed oil and chlorinated rubber epoxy MFCCs were moderately difficult to atomize. The clear acrylic and wax based MFCCs were easiest to spray. The white color of the pigment in the emulsion type MFCCs aided application of the compound in a homogenous and continuous layer.

In several of the samples treated with wax MFCC the membrane exhibited crazing or a network of cracks that formed as the material dried and the concrete set. No trend in the formation of this crazing was found; its presence or absence was random with respect to cement type or aggregate type. Crazing of this type has been reported after application of the compound to still-bleeding concrete specimens.[197]

3.3.3.2. Deicer mediated freeze/thaw scaling tests

Mean values of and the standard error for the cumulative mass lost during repeated freezing and thawing cycles are presented for each concrete blend. Standard error values are indicative of the nature of the surface failure. High standard errors that revert to lower values correspond to sample populations in which one sample lost a great deal of mass and the other samples failed similarly at a later time.

3.3.3.2.1. OPC concrete with crushed limestone aggregate:

Specimens prepared from OPC with crushed limestone aggregate performed the best of all of the mixes (Figure 19). PAMS and Wax coating showed a steep initial scaling loss and continued to lose mass during the entire test. The CR and acrylic coatings had a rate of mass loss near zero for approximately half of the test. Thin sections of mortar over large aggregate particles near the surface were the only regions damaged by spalling. The linseed treated specimens began to rapidly lose mass near the end of the testing cycle but finished the test with large sections of undamaged surface.

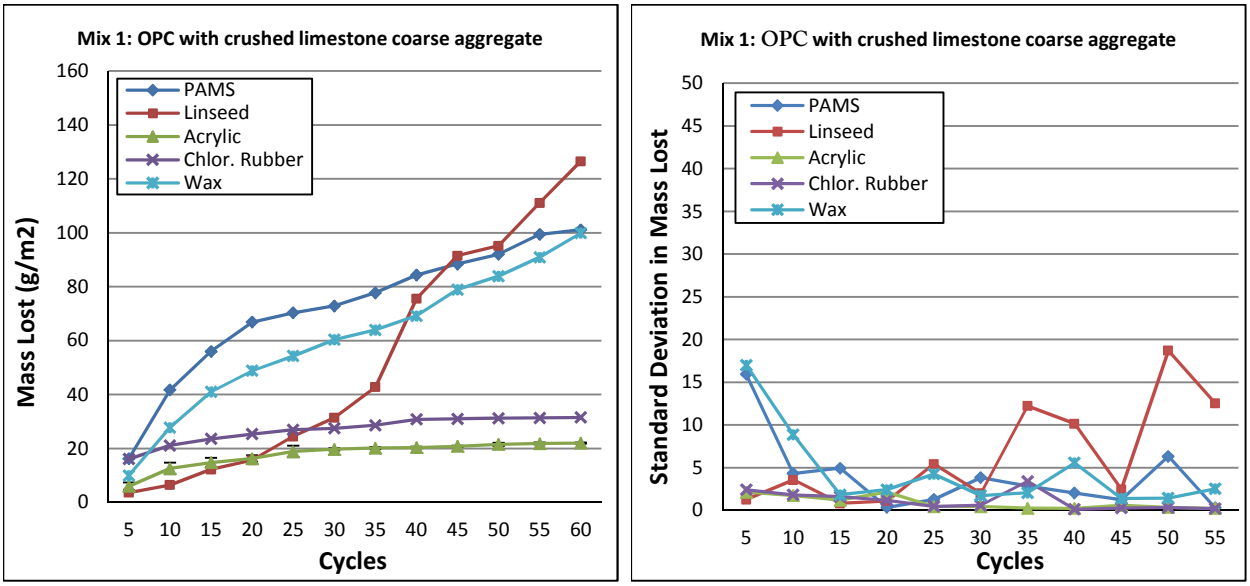

Figure 19: Cumulative mass lost to scaling for OPC concrete with crushed limestone aggregate. Note: Y axis scale is 1/10th that of the other figures in this section

3.3.3.2.2. 30% Fly Ash concrete with crushed limestone aggregate

Replacing 30% of the cementitious material with Class C Fly Ash resulted in mass losses almost an order of magnitude greater than the comparable OPC specimens (Figure 20). Fly ash greatly increased the slump value of the mix and necessitated the use of a lower w/cm ratio. This concrete was still very plastic after two hours. The lower w/cm ratio may have made the specimens more sensitive to surface evaporation. Concretes containing fly ash require longer curing times; the fly ash fraction hydrates via slower pozzolanic reactions. If the OPC fraction of the cementitious material consumes most of the free water, pozzolanic reactions will be limited and the paste will not develop adequate strength and have high porosity.[198,199]

PAMS, CR, and acrylic MFCC treated specimens lost large amounts of finished surface within the first 10 cycles. This represented complete surface failure to a depth of several millimeters. Once the surface had failed the mass loss rate dramatically decreased. This suggests that the curing compound did not adequately control the loss of water to evaporation during the curing period or altered the surface structure of the specimens. Wax specimens performed well in comparison to the other treatment types. Linseed oil treated specimens performed well for the early portion of the test but continued to lose mass during the entire test.

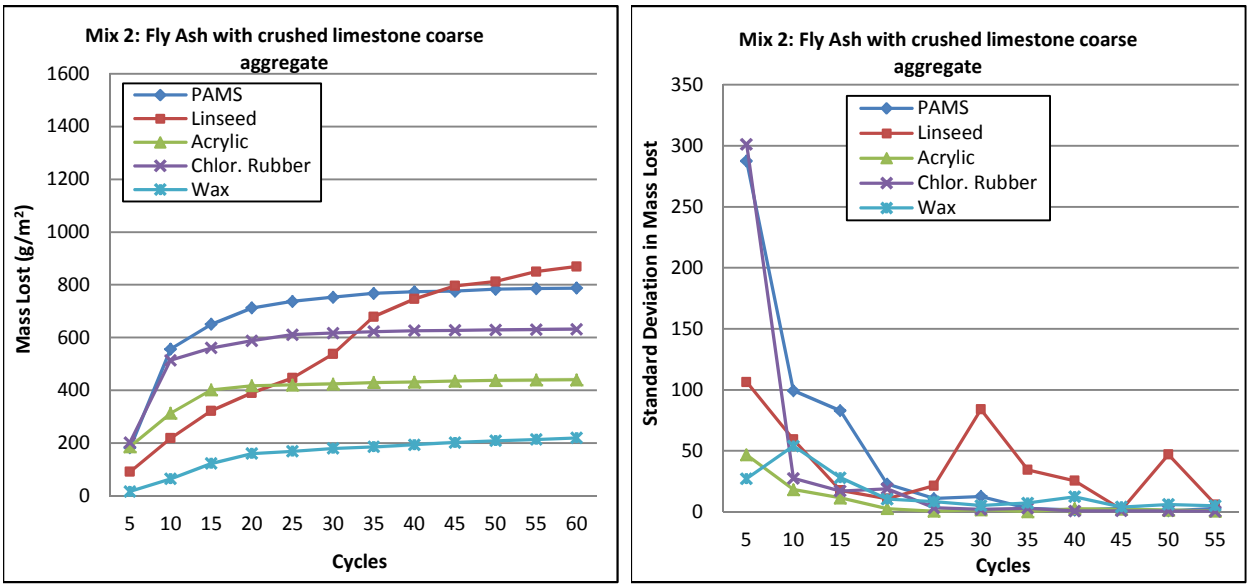

Figure 20: Scaling mass loss for 30% Fly Ash concrete with crushed limestone aggregate

3.3.3.2.3. 30% Slag concrete with crushed limestone aggregate

Specimens prepared with grade 100 ground-granulated blast furnace slag (slag cement) also showed a dramatic decrease in resistance (Figure 21). Slag cement produced concrete that had

distinctly gelled after 2 hours. This gelling decreased the bleed rate of the concrete and the sample surface had lost the "shiny" appearance associated with bleed water after 2 hours. PAMS, CR, ACR, and nanoparticle specimens had regions of an undamaged surface remaining at the end of testing, while Wax and Linseed specimens failed to a depth of several millimeters across the entire surface.

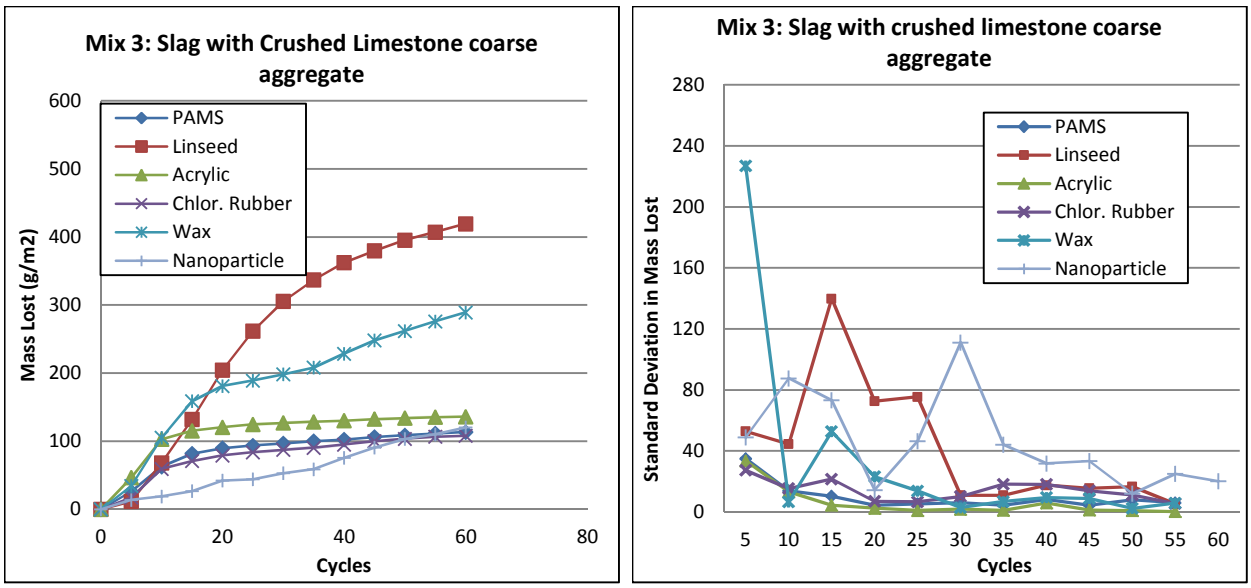

Figure 21: Scaling mass loss for 30% slag concrete with crushed limestone aggregate

3.3.3.2.4. OPC Concrete with igneous gravel aggregate

With the exception of Linseed samples, the OPC specimens with igneous gravel aggregate behaved similarly to the specimens prepared with crushed limestone (Figure 22). There was some sandstone present in the coarse aggregate that failed under the test conditions. When

aggregate particles failed near the surface, this resulted in a loss of the mortar cover over the particle and eventual loss of the entire stone, leaving a negative impression in the mortar. The mass of stone influenced the scaling mass and introduced flaws and stress into the surface. Wax and Acrylic specimens finished testing with large areas of surface undamaged. CR specimens lost an appreciable amount of surface early in testing but stabilized rapidly. PAMS specimens performed well until beginning to lose large areas of surface cover after 50 freeze/thaw cycles. These specimens lost cover completely to a depth of several millimeters.

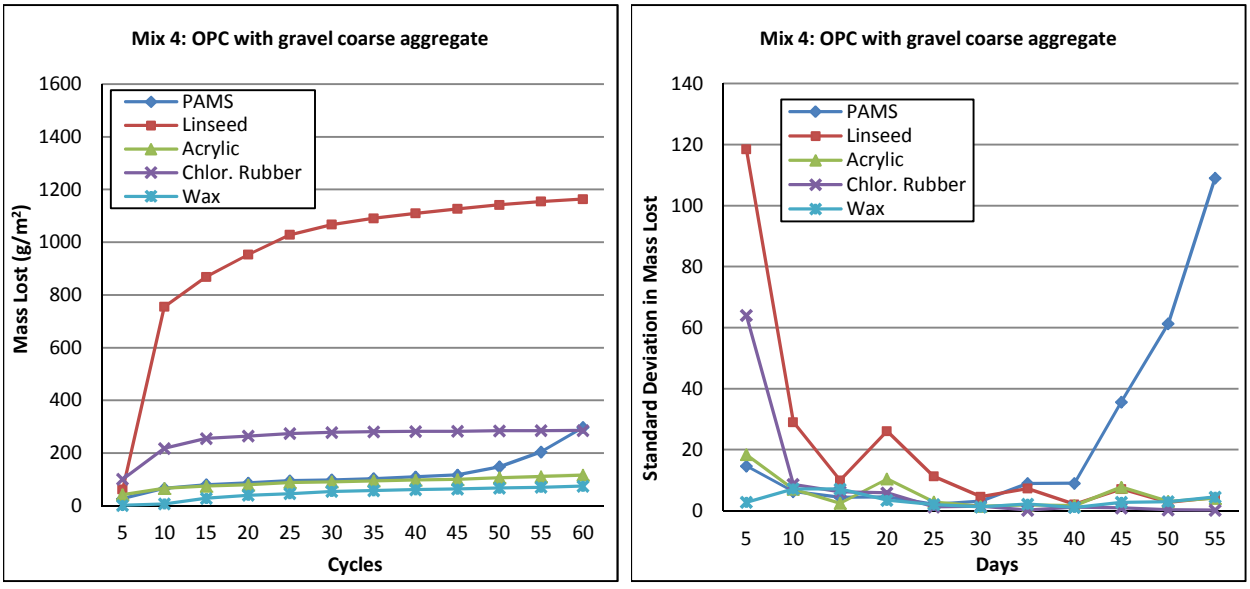

Figure 22: Scaling mass loss in OPC concrete with igneous gravel coarse aggregate

3.3.3.2.5. 30% Fly Ash Cement with igneous gravel aggregate

Specimens prepared from concrete with fly ash and igneous gravel aggregate performed similarly to those prepared with crushed limestone aggregate (Figure 23). Fly Ash dramatically decreased the concrete's resistance to scaling. CR and Linseed specimens lost large amounts of finished surface within the first 10 days of testing. This represented complete surface failure, in which the entire surface crumbled to a depth of several millimeters. PAMS specimens lost surface cover by 30 freeze/thaw cycles. Wax and ACR specimens performed well in comparison to the other treatment types. ACR appeared more effective when used on a 30% FA concrete with gravel aggregate as opposed to crushed limestone aggregate.

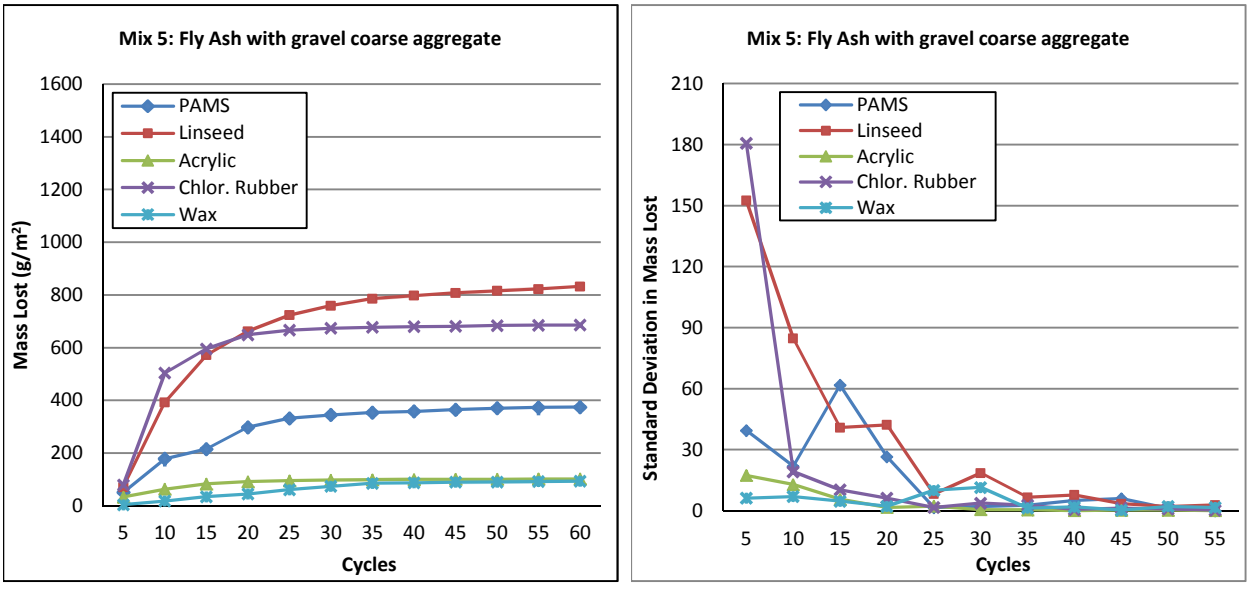

Figure 23: Scaling mass lost for 30% Fly Ash concrete with igneous gravel aggregate

3.3.3.2.6. Slag Cement with igneous gravel aggregate

The performance of slag cement concretes with igneous gravel coarse aggregate was similar to that of those prepared with the crushed limestone aggregate (Figure 24). Wax and Lin specimens rapidly lost several millimeters of surface. CR and Acrylic specimens were moderately resistant to scaling. PAMS specimens performed very poorly in relation to the crushed limestone aggregate. The high standard deviation in the mass lost for PAMS treated specimens shows that the failure occurred in single specimens at 25, 35, and 50 cycles.

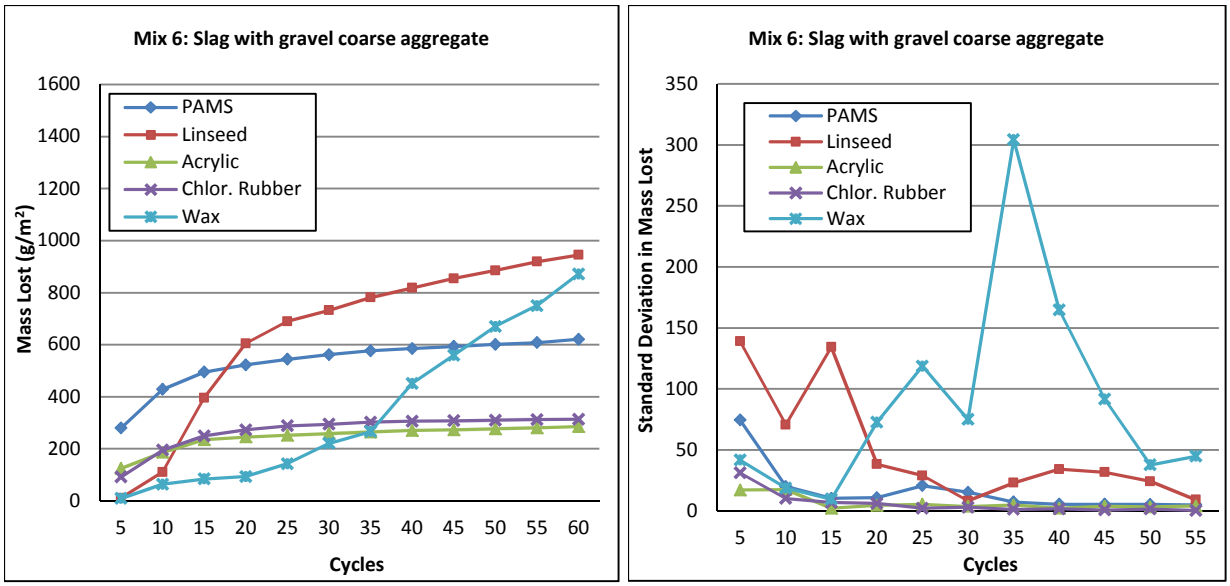

Figure 24: Scaling mass lost for 30% Slag concrete with igneous gravel aggregate

3.3.3.2.7. Observations by curing compound formulation

Linseed oil-based MFCC performed the worst of the five types tested for all concrete mix designs. Wax specimens of OPC and fly ash lost little mass and were resistant to scaling; specimens with slag cement performed poorly in relation. PAMS specimens lost little mass when

the cement was OPC; binary blend samples were less resistant to scaling. Acrylic and CR specimens performed well in relation to the emulsion type except in the specific case of chlorinated rubber on fly ash concrete. Acrylic specimens lost little mass regardless of the cement type or aggregate used.

3.3.3.2.8. Statistical Analysis of Scaling Behavior

A multi-factor analysis of variance (ANOVA) was performed at each sampling point to determine the factors most important to scaling performance during the 60 cycle test. Aggregate type was not correlated with scaling loss at any time. At 5 freeze/thaw cycles the coating type, cement type, and interactions between cement type and aggregate were strongly correlated with differences in performance at $p=0.05$, suggesting that the both concrete mix design and the coating type must be chosen to minimize scaling. At the test midpoint, all effects were significant except aggregate type. At 45 or more cycles interaction between the coating type and the aggregate type were no longer significant. This analysis suggests that MFCC choice is significant, but also that supplemental cementitious material type, interactions between SCM and aggregate, and interactions between MFCC and cement type (e.g. avoiding wax MFCC on

slag blends and avoiding chlorinated rubber MFCC on fly ash blends) are relevant to improving scaling performance.

3.3.3.3. Chloride ion penetration

Chloride ion concentration at each depth is presented in Figure 25. Wax based MFCC treated specimens generally had greater chloride ion penetrations when the coarse aggregate was limestone. There was a slight decrease in chloride ion penetration in specimens prepared with gravel coarse aggregate at both depth ranges. This may be due to the greater angularity and aspect ratio of the limestone coarse aggregate. Aggregate particles with a large aspect ratio extend further into the bulk concrete, and provide a highly porous pathway for water transport along the interfacial transition zone. Reactive microfine material on the aggregate can also affect the aggregate-mortar bond and allowing bulk transport along decoupled interfaces.

At depths between 0.04 in. and 0.5 in. interactions between the coating applied and either cement or aggregate types were not significant at P=0.05 (Table 8); MFCC choice can be independent of concrete or aggregate choice at this depth. All treatments and interactions correlated significantly between 0.5 in. and 1 in. depth, although only wax MFCC performed significantly worse.

Table 8: Probability that treatment factor was not significant for chloride ion concentration at each depth by multi-factor ANOVA analysis

Variance Source	0.5 in.	1 in.
Coating Type	2%	0%
Cement Type	0%	1%
Aggregate Type	0%	0%
Coating×Cement	44%	0%
Coating×Aggregate	100%	0%
Cement×Aggregate	0%	0%

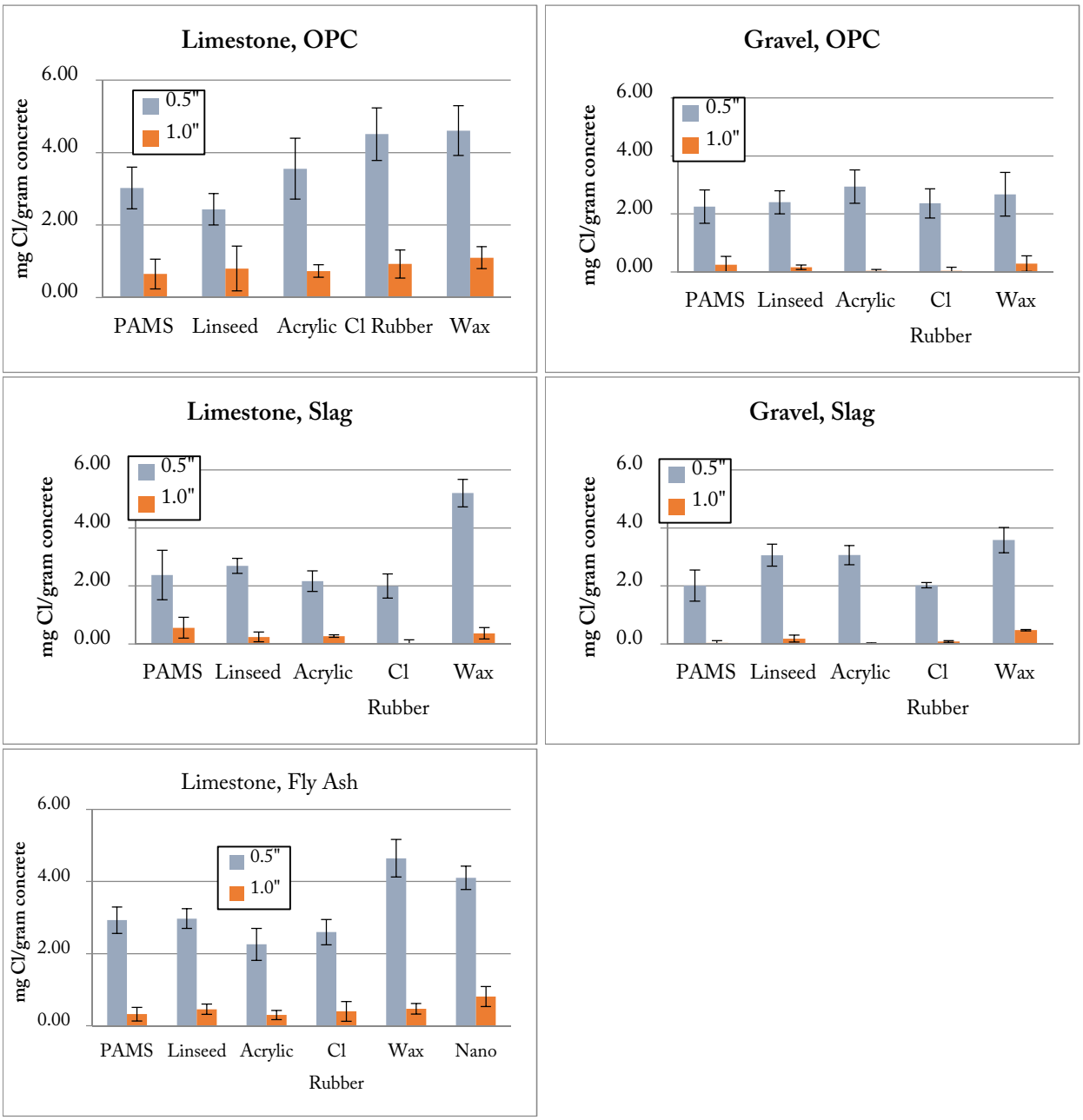

Figure 25: Chloride ion concentration profile for each cement type and aggregate source

3.3.3.4. ASTM C156 and Carbonation Depth Results

OPC mortar specimens were prepared with each curing compound type and the evaporative control performance for each formulation was measured (Table 9). Samples that were untreated were included as a reference point. Wax and Linseed were slightly effective at preventing moisture loss. PAMS was the most effective of the emulsion formulations, decreasing evaporation by 28%. CR and Acrylic specimens were much more resistant to evaporative loss.

Table 9: Evaporative mass loss during 3 day curing period in 37.8°C and 32% RH air and carbonation depth after 28 day exposure to 100%CO_2 atmosphere

Coating Type	Coating Rate	Water Loss Rate	S.D.	% Reduction	Carbonation Depth
	ft^2/gal	kg/m^2	kg/m^2		mm
None	NA	3.69	0.16	Reference	4.0
PAMS	200	2.65	0.14	28%	5.8
Wax	196	3.39	0.22	8%	5.0
Linseed	201	3.11	0.11	16%	8.2
Chlorinated Rubber	199	0.81	0.03	78%	1.9
Acrylic	197	1.16	0.04	69%	2.1
IMFCC	198	4.35	0.09	-18%	4.5

Samples prepared from the emulsion type MFCCS were less resistant to carbonation damage than those prepared with solvent type MFCCs at P=0.05. Linseed MFCC treated specimens had greater carbonation depth than the untreated specimens. The protective behavior of the solvent MFCCs is likely due to the treatment penetrating the mortar pore structure, sealing it,

and excluding the CO_2 atmosphere from the pore structure of the specimen. IMFCC treated specimens lost more mass to evaporation than MFCC or untreated specimens, but did not exhibit dramatically different carbonation reaction rates.

3.3.3.5. Decision matrix from combined data

The numerous second order correlations among the treatments and performance outcomes complicates the selection process for concrete designers. It is therefore useful to present the conclusions of this study in the form of a weighted decision chart in which a design element (curing compound) is rated against other design parameters by choosing numeric values for performance in each design metric. An example is provided below, where the weight of scaling damage is twice that of chloride penetration resistance (Table 10).

This decision table could be expanded to include carbonation resistance, cost, and aesthetic properties as long as the additional performance metrics are given an appropriate numerical ranking and criterion weight. Large numeric rankings for unacceptable performance could also be replaced with go/no go rankings to exclude. As an example, scaling losses greater than 1000g/m^2 could exclude a coating even if it were effective at preventing carbonation and chloride penetration with low cost.

Table 10: General guidance for concrete engineers. Low magnitude represents improved performance. Note: the highlighted section represents the scaling resistance of the Limestone/OPC system, which performed dramatically better and would rate as excellent in comparison.

			Coating Type				
Aggregate Type	Cement Type	Property	PAMS	Linseed	Acrylic	Cl. Ru.	Wax
Limestone	OPC	Scaling	3	3	1	1	3
		Chloride Res.	2	2	2	3	3
	30% Fly Ash	Scaling	4	5	3	5	2
		Chloride Res.	2	2	1	2	3
	30% Slag	Scaling	2	10	2	2	5
		Chloride Res.	1	2	1	1	3
Gravel	OPC	Scaling	2	10	1	2	1
		Chloride Res.	1	1	2	1	2
	30% Fly Ash	Scaling	2	5	1	4	1
		Chloride Res.	1	1	1	1	1
	30% Slag	Scaling	4	5	2	2	5
		Chloride Res.	1	2	2	1	2
		Total	14	29	10	14	16
		Weighted Average	2.1	4.0	1.6	2.1	2.6

Scaling		
Rating	g/m^2	Numeric Rating
Unacceptable	>1000	10
Poor	800<x<1000	5
Fair	600<x<800	4
Good	400<x<600	3
Very Good	200<x<400	2
Excellent	<200	1

Chloride ion penetration		
Rating	$\frac{\text{mg Cl}}{\text{g concrete}}$	Numeric Rating
Poor	>4	3
Good	2<x<4	2
Excellent	<2	1

3.3.4. Conclusions

Curing compounds are designed to support cementitious hydration reactions by preventing evaporative loss of chemically available water from the near surface of exposed emplacements. Proper curing can mitigate damage to concrete from surface scaling, carbonation reactions, and chloride ion penetration by producing a denser and less porous CSH gel matrix. Deicer mediated surface scaling is the most visible of these damage modalities and can occur in a single winter in middle latitudes. Scaling destroys surface textures applied to a pavement for traction and noise modification, changes the aesthetics of the concrete product, and increases the difficulty of removing snow and debris. Linseed oil emulsion type curing compound was least effective at producing durable specimens. Generally, solvent type MFCCs designed to cure and seal the concrete surface produced surfaces that were more resistant to damage associated with cold weather than emulsion type MFCCs. Interactions between curing compounds and cement paste chemistry can lead to surfaces with poor scaling resistance.

SECTION 3: A TECHNICAL NOTE ON PROTON TRANSFER RESONANCE MASS SPECTROMETRY

1. OVERVIEW OF TECHNIQUE

Chemical Ionization Mass Spectrometry (CIMS) is an analytic technique capable of detecting volatile organic contaminant species at extremely low concentration, in real time, with little or no sample preparation requirement. This instrument generates gas phase ions that react with and ionize any species of interest. The ions transfer charge to the target component, producing a secondary ion that is detected by any of several mass spectrometer instrument types. Ion transfer reactions are less likely to result in fragmentation of molecules of interest to the researcher than other techniques, i.e. electron spray. This simplifies data analysis; the m/z signal detected for the ionized compound is typically similar to that of the parent compound. Proton Transfer Reaction mass spectrometry (PTR-MS) uses protonated water, H_3O^+, as the reagent ion, and typically results in the formation of secondary ions with 1 amu additional mass compared to the parent compound (Equation 7). This is an equilibrium reaction with kinetics on the order of 10^9 transfer reactions per second in a volume of $1cm^3$. The readiness with which a particle accepts an additional proton is the proton affinity of that component. When the proton affinity of a component R is greater than that of water (691 kJ/mole) the formation of RH^+ is

thermodynamically favored and the reverse reaction is considered negligible. The proton is not transferred at appreciable rates with compounds with proton affinities lower than that of water.

Equation 7: Proton Resonance Equilibrium Reaction

$$H_3O^+ + R \leftrightarrow H_2O + RH^+$$

Kinetic analysis of Equation 7 with the assumption that the number density of H_3O^+ ion greatly exceeds that of all compounds with proton affinities greater than 697 kJ/mole (that of H_2O) results in the well-known relationship in Equation 8:[200]

Equation 8: The number density of daughter ions produced by the PTR-MS instrument

$$[RH^+] \approx [H_3O^+]k[R]\Delta t$$

Where square brackets denote number density (cm^{-3}), k is the kinetic rate constant of the proton transfer reaction, and Δt is the residence time of the ions in the drift tube. The transmission efficiency τ of a quadrupole-type mass spectrometer is dependent on the mass to charge ratio of the ion detected. Rearranging Equation 8 to solve for the mixing ratio concentration of R in PPB_v (parts per billion, volume), correcting for the mass-dependent transmission efficiency of the quadrupole mass spectrometer and conversion from number density to volume mixing ratio results in Equation 9

Equation 9: Mixing ratio concentration of species R in PPB_v as detected by the PTR-MS instrument

$$[R] = \frac{Hz_{Mass\ of\ R}}{Hz_{Water}} * \frac{\tau}{k\Delta t} * \frac{10^9}{N}$$

Where Hz denotes the signal detected at the m/z ratio of the compound of interest and N is the number density of gas particles in the drift tube as calculated from the operating pressure and temperature.

The high number of H_3O^+ ions generated by the glow discharge chamber results in detector saturation when measuring at m/z=19. To approximate the actual intensity of the water signal the smaller signal at m/z=21 (heavy water) is monitored and adjusted using the isotopic distribution of the source water. Table 11 shows the elemental and molecular isotopic ratios of water in VSMOW as well as the corrected values for Madison, WI.[201]

	VSMOW		Madison Water
Isotope	Isotopic Fraction	Correction Factor δ (‰)	Isotopic Fraction
1H	99.984%		99.986%
2H	0.016%	-73.5‰	0.014%
16O	99.837%		99.763%
17O	0.038%		0.038%
18O	0.201%	-8.95‰	0.199%

Water Mass g/mol	Isotopic Fraction of VSMOW	Madison WI Isotopic Fraction
18.011	9.97E-01	9.97E-01
19.015	3.72E-04	3.80E-04
19.017	3.11E-04	2.88E-04
20.015	2.00E-03	1.99E-03
20.021	1.16E-07	1.10E-07
20.023	2.60E-08	2.08E-08
21.021	6.23E-07	5.73E-07
Total at 20 AMU	2.000E-03	1.987E-03

Table 11: Correcting for fractionation in the elemental and molecular isotopic composition of water in Madison, WI

With these factors determined it is possible to calculate a theoretical concentration for any compound for which a proton reaction rate constant has been reported. These constants are typically near 2×10^{-9} cm^3/s, and can be estimated using several methods (*e.g.* ADO (Average

Dipole Orientation)) with good agreement with the literature, but literature values vary by as much as 50%. Several authors have recommended and published work using 2×10^{-9} cm^3/s as the value of the kinetic rate constant for all compounds due to the large uncertainty in the values. While this may result in concentrations that are adequately accurate in some instances, a simple calibration performed using a certified source is preferred for work demanding high accuracy.

2. DESCRIPTION OF INSTRUMENT

In the CIMS instrument employed for this research, H_3O^+ ions are generated by introducing a flow of 18 SCCM USP air through the headspace of a small tank of deionized water. This humid air enters a glow discharge chamber with approximately 600V of tension applied and injected into a low pressure drift tube with the sampled gas. The drift tube pressure is controlled by adjusting the flow rate of the sample gas entering the chamber with a needle valve, and typically operates at 7.5 Torr with a sample gas flow rate of 118 SCCM. A 3.4kV constant potential is applied along the length of this 10cm drift tube to accelerate the reagent and secondary ions towards the detector and kinetically fragment most ion clusters that form. A quadrupole mass filter is used to separate the produced ions by mass to charge ratio (m/z). The ions that traverse the oscillating field in the quadrupole impact a current counting detector. The output from the detector has units of events per second (Hz) and is directly proportional to the

ratio of the number density concentration of ions in the drift tube to the parent ion signal (m/z=19).

3. Calibration and Transmission Efficiency Determination

The CIMS instrument must be calibrated prior to use. When measuring the concentration of only a few species it is easiest to simply perform several dilutions of a standard calibration standard. A schematic of the apparatus used for calibration of the CIMS used in this research is presented in Figure 26. The mass flow controllers used were capable of providing two stages of accurate 500:1 dilution, allowing for calibration across several orders of magnitude.

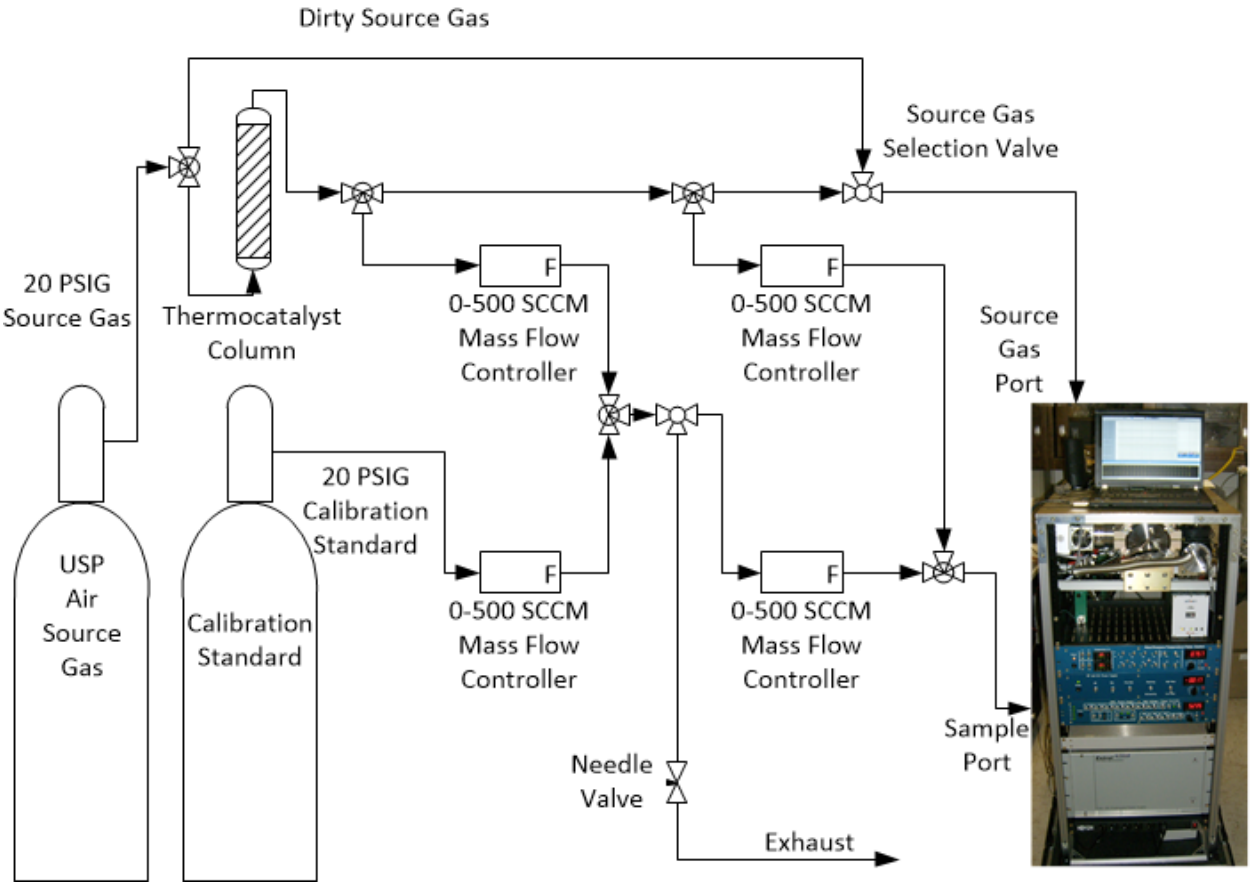

Figure 26: Calibration standard dilution and instrument background determination apparatus

Determining the concentration of an unknown species, or a species for which a calibration standard is not available, requires determining the m/z dependent transmission of the quadrupole mass spectrometer. This is most readily accomplished by sampling the headspace of vials containing compounds with masses spanning the m/z range of interest. The high concentration of the sampled gas will result in a measurable decrease in the signal at 21 amu, corresponding to the water signal. The ratio of the decrease in water signal to the increase in the compound is the relative transmission efficiency at the mass of that compound. The areas between points are

interpolated using a variety of methods. There are several instances in the literature of cubic splines being used, as they are relatively easily calculated and aesthetically pleasing, but there is currently no rigorous justification for their use.[202–204]

SECTION 4: SUMMARY AND DIRECTION OF FUTURE WORK

Photoactive thin films possess unique properties that engender their use in sustainable engineering and chemical production. This dissertation provides several examples and experimental outcomes of their application, but significant work still remains to increase their functionality and adoption outside of the lab. Commercial deployment and application will require improvements in the following categories: decreasing the cost of precursor materials and membrane application, improving catalyst performance, improving catalyst and membrane durability, improving reactor design, and public outreach and education.

Membrane precursors are currently prepared using commercially prepared powders, milling of large particles, sol-gel processing, plasma processing, flame processing, heterogeneous chemical growth, and several other techniques. These precursors are applied to a substrate in a variety of methods, including dip coating, spin coating, slip casting, physical or chemical deposition, slurry processes, and in-situ modification of the substrate. After application, the membrane often requires further processing, *e.g.* thermal annealing, doping, optical sintering, dyeing, *etc.* Each step of this process affords opportunity to improve the membrane for a particular application but requires significant investment in research and development, capital equipment, processing time, energy, and materials. Deployment of thin film photocatalysts will

require optimization of the entire embodied cost, which is an area largely unaddressed in the available literature.

The complete lifecycle of the applied membrane should be considered when evaluating suitability for a given function. Photoactive film performance should be understood in the context of the application, high initial performance with poor longevity is only useful if the economics of replacement are favorable. A lower cost material with poorer performance can suffice if the usable lifespan is significantly greater. Making this determination requires an understanding of membrane evolution and related performance changes. Membranes evolve through several mechanisms, as examples membranes with high surface areas possess significant excess energy, and will decrease surface area when conditions permit and environmental contaminants and reaction intermediates that chemisorb to the surface without further reaction can poison the catalyst and decrease reaction rates and conversion efficiency. Long term performance of these materials, when evaluated at all in the literature, is typically on the order of hours to several tens of hours. Real world applications will require understanding of membrane behavior at much longer time scales.

When used as photocatalysts, effective deployment of these membranes requires complete reactor design. Sufficient light of the correct energy must interact with the catalyst to maximize conversion, but excess light only results in the generation of heat. Reactors with high conversion

rates and volumetric efficiency require the correct balance of light, catalyst surface area, and geometry. Lighting sources are constantly being improved with regards to intensity, efficiency, and available spectrum or wavelength. Solid-state lighting in particular has dramatically improved, with shorter wavelengths and higher intensities at lower cost being introduced at a remarkable pace. Reactor design utilizing solid-state lighting is currently in its infancy and promises to be a fruitful avenue of research.

Finally, adoption will only occur within the correct regulatory and commercial environment. There is substantial momentum in the use of legacy or current technology that must be overcome before these novel materials are widely deployed. Legislators and regulatory bodies must be educated to the promise and limitations of photoactive membranes to provide pathways to the consumer, consumers must be educated to the potential benefits, and both existing and entrepreneurial ventures must overcome the engineering and economic barriers to production. This work is already in progress for many applications and in many markets: as examples several manufacturers offer self-cleaning glass, Japan is currently deploying concrete pavement coatings for the removal of airborne contaminants associated with internal combustion, and companies are developing coatings to treat and remove graffiti. Further work is required to identify potential applications and develop new markets.

SECTION 5: WORKS CITED

1. Kim, S. B. & Hong, S. C. Kinetic study for photocatalytic degradation of volatile organic compounds in air using thin film TiO2 photocatalyst. *Appl. Catal. B Environ.* **35,** 305–315 (2002).
2. Augugliaro, V. *et al.* Overview on oxidation mechanisms of organic compounds by TiO2 in heterogeneous photocatalysis. *J. Photochem. Photobiol. C Photochem. Rev.* **13,** 224–245 (2012).
3. Vildozo, D., Portela, R., Ferronato, C. & Chovelon, J.-M. Photocatalytic oxidation of 2-propanol/toluene binary mixtures at indoor air concentration levels. *Appl. Catal. B Environ.* **107,** 347–354 (2011).
4. Sleiman, M., Conchon, P., Ferronato, C. & Chovelon, J.-M. Photocatalytic oxidation of toluene at indoor air levels (ppbv): Towards a better assessment of conversion, reaction intermediates and mineralization. *Appl. Catal. B Environ.* **86,** 159–165 (2009).
5. Yang, L. & Liu, Z. Study on light intensity in the process of photocatalytic degradation of indoor gaseous formaldehyde for saving energy. *Energy Convers. Manag.* **48,** 882–889 (2007).
6. Teh, C. M. & Mohamed, A. R. Roles of titanium dioxide and ion-doped titanium dioxide on photocatalytic degradation of organic pollutants (phenolic compounds and dyes) in aqueous solutions: A review. *J. Alloys Compd.* **509,** 1648–1660 (2011).
7. Chatterjee, D. & Dasgupta, S. Visible light induced photocatalytic degradation of organic pollutants. *J. Photochem. Photobiol. C Photochem. Rev.* **6,** 186–205 (2005).
8. Li, X. & Jenks, W. S. Isotope Studies of Photocatalysis: Dual Mechanisms in the Conversion of Anisole to Phenol. *J. Am. Chem. Soc.* **122,** 11864–11870 (2000).
9. Salazar, C. & Nanny, M. A. Influence of hydrogen bonding upon the TiO2 photooxidation of isopropanol and acetone in aqueous solution. *J. Catal.* **269,** 404–410 (2010).
10. Wang, S., Ang, H. M. & Tade, M. O. Volatile organic compounds in indoor environment and photocatalytic oxidation: State of the art. *Environ. Int.* **33,** 694–705 (2007).

11. Nakata, K. & Fujishima, A. TiO2 photocatalysis: Design and applications. *J. Photochem. Photobiol. C Photochem. Rev.* **13,** 169–189 (2012).
12. Albini, A. & Fagnoni, M. The greenest reagent in organic synthesis: light. *Green Chem. React.* 173–189 (2008).
13. Cermenati, L. & Albini, A. Titanium Dioxide Photocatalysis for Radical Alkylation. *J. Adv. Oxid. Technol.* **5,** 58–66 (2002).
14. Cherevatskaya, M. *et al.* Visible-Light-Promoted Stereoselective Alkylation by Combining Heterogeneous Photocatalysis with Organocatalysis. *Angew. Chem. Int. Ed.* **51,** 4062–4066 (2012).
15. Gu, Q. *et al.* Photocatalytic reforming of C3-polyols for H2 production. *Appl. Catal. B Environ.* **106,** 689–696 (2011).
16. Higashimoto, S. *et al.* Selective photocatalytic oxidation of benzyl alcohol and its derivatives into corresponding aldehydes by molecular oxygen on titanium dioxide under visible light irradiation. *J. Catal.* **266,** 279–285 (2009).
17. Manley, D. W. *et al.* Unconventional titania photocatalysis: direct deployment of carboxylic acids in alkylations and annulations. *J. Am. Chem. Soc.* (2012). at <http://pubs.acs.org.ezproxy.library.wisc.edu/doi/abs/10.1021/ja306168h>
18. Nguyen, V.-H., Chan, H.-Y., Wu, J. C. S. & Bai, H. Direct gas-phase photocatalytic epoxidation of propylene with molecular oxygen by photocatalysts. *Chem. Eng. J.* **179,** 285–294 (2012).
19. Shiraishi, Y. & Hirai, T. Selective organic transformations on titanium oxide-based photocatalysts. *J. Photochem. Photobiol. C Photochem. Rev.* **9,** 157–170 (2008).
20. Wang, Y., Li, L., Yang, K., Samuelson, L. A. & Kumar, J. Nanocrystalline TiO2-Catalyzed Solid-State Polymerization of Diacetylene in the Visible Region. *J. Am. Chem. Soc.* **129,** 7238–7239 (2007).
21. Yanagida, S. *et al.* Semiconductor photocatalysis. I. Quantitative photoreduction of aliphatic ketones to alcohols using defect-free zinc sulfide quantum crystallites. *J. Phys. Chem.* **94,** 3104–3111 (1990).
22. Fujishima, A. & Honda, K. TiO2 photoelectrochemistry and photocatalysis. *Nature* **37,** 238 (1972).

23. Jing, D. *et al.* Efficient solar hydrogen production by photocatalytic water splitting: From fundamental study to pilot demonstration. *Int. J. Hydrog. Energy* **35,** 7087–7097 (2010).
24. MOHAMED, R. M. & AAZAM, E. S. H2 Production with Low CO Selectivity from Photocatalytic Reforming of Glucose on Ni/TiO2-SiO2. *Chin. J. Catal.* **33,** 247–253 (2012).
25. Tang, J., Durrant, J. R. & Klug, D. R. Mechanism of Photocatalytic Water Splitting in TiO2. Reaction of Water with Photoholes, Importance of Charge Carrier Dynamics, and Evidence for Four-Hole Chemistry. *J. Am. Chem. Soc.* **130,** 13885–13891 (2008).
26. Maeda, K. Photocatalytic water splitting using semiconductor particles: History and recent developments. *J. Photochem. Photobiol. C Photochem. Rev.* **12,** 237–268 (2011).
27. Abe, R. Recent progress on photocatalytic and photoelectrochemical water splitting under visible light irradiation. *J. Photochem. Photobiol. C Photochem. Rev.* **11,** 179–209 (2010).
28. Kawahara, T., Konishi, Y., Tada, H., Tohge, N. & Ito, S. Patterned TiO2/SnO2 Bilayer Type Photocatalyst. 2. Efficient Dehydrogenation of Methanol. *Langmuir* **17,** 7442–7445 (2001).
29. Cutler, T. D. & Zimmerman, J. J. Ultraviolet irradiation and the mechanisms underlying its inactivation of infectious agents. *Anim. Health Res. Rev.* **12,** 15–23 (2011).
30. Hijnen, W. A. M., Beerendonk, E. F. & Medema, G. J. Inactivation credit of UV radiation for viruses, bacteria and protozoan (oo)cysts in water: A review. *Water Res.* **40,** 3–22 (2006).
31. Kowalski, W., Bahnfleth, W. & Hernandez, M. A Genomic Model for the Prediction of Ultraviolet Inactivation Rate Constants for RNA and DNA Viruses. *IUVA News June* (2009). at <http://www.aerobiologicalengineering.com/Genomic.pdf>
32. Fontenla, J., White, O. R., Fox, P. A., Avrett, E. H. & Kurucz, R. L. Calculation of solar irradiances. I. Synthesis of the solar spectrum. *Astrophys. J.* **518,** 480 (2009).
33. Chance, K. & Kurucz, R. L. An improved high-resolution solar reference spectrum for earth's atmosphere measurements in the ultraviolet, visible, and near infrared. *J. Quant. Spectrosc. Radiat. Transf.* **111,** 1289–1295 (2010).
34. Salthammer, T., Uhde, E., Omelan, A., Lüdecke, A. & Moriske, H. J. Estimating human indoor exposure to elemental mercury from broken compact fluorescent lamps (CFLs). *Indoor Air* (2012). at

<http://onlinelibrary.wiley.com.ezproxy.library.wisc.edu/doi/10.1111/j.1600-0668.2011.00764.x/full>

35. Emmanuel, J., Orris, P. & Chartier, Y. Replacement of mercury thermometers and sphygmomanometers in health care. (2011). at <http://balifokus.asia/balifokus/wp-content/uploads/2012/04/WHO-Technical-Guidance_Replacement-of-Hg-Thermometers-and-Sphygmo.pdf>
36. Dalrymple, O. K., Stefanakos, E., Trotz, M. A. & Goswami, D. Y. A review of the mechanisms and modeling of photocatalytic disinfection. *Appl. Catal. B Environ.* **98,** 27–38 (2010).
37. Maness, P. C. *et al.* Bactericidal activity of photocatalytic TiO2 reaction: toward an understanding of its killing mechanism. *Appl. Environ. Microbiol.* **65,** 4094–4098 (1999).
38. Vohra, A., Goswami, D. Y., Deshpande, D. A. & Block, S. S. Enhanced photocatalytic inactivation of bacterial spores on surfaces in air. *J. Ind. Microbiol. Biotechnol.* **32,** 364–370 (2005).
39. Dunlop, P. S. M. *et al.* Inactivation of clinically relevant pathogens by photocatalytic coatings. *J. Photochem. Photobiol. Chem.* **216,** 303–310 (2010).
40. Cho, M., Chung, H., Choi, W. & Yoon, J. Linear correlation between inactivation of< i> E. coli</i> and OH radical concentration in TiO< sub> 2</sub> photocatalytic disinfection. *Water Res.* **38,** 1069–1077 (2004).
41. Benabbou, A. K., Derriche, Z., Felix, C., Lejeune, P. & Guillard, C. Photocatalytic inactivation of< i> Escherischia coli</i>: Effect of concentration of TiO2 and microorganism, nature, and intensity of UV irradiation. *Appl. Catal. B Environ.* **76,** 257–263 (2007).
42. Mitoraj, D. *et al.* Visible light inactivation of bacteria and fungi by modified titanium dioxide. *Photochem Photobiol Sci* **6,** 642–648 (2007).
43. Snider, G. & Ariya, P. Photo-catalytic oxidation reaction of gaseous mercury over titanium dioxide nanoparticle surfaces. *Chem. Phys. Lett.* **491,** 23–28 (2010).
44. Hoffmann, M. R., Martin, S. T., Choi, W. & Bahnemann, D. W. Environmental Applications of Semiconductor Photocatalysis. *Chem. Rev.* **95,** 69–96 (1995).

45. Yu, Q. L. & Brouwers, H. J. H. Indoor air purification using heterogeneous photocatalytic oxidation. Part I: Experimental study. *Appl. Catal. B Environ.* **92,** 454–461 (2009).
46. Yu, Q. L., Ballari, M. M. & Brouwers, H. J. H. Indoor air purification using heterogeneous photocatalytic oxidation. Part II: Kinetic study. *Appl. Catal. B Environ.* **99,** 58–65 (2010).
47. Vijayalakshmi, S. P. & Madras, G. Photocatalytic degradation of poly(ethylene oxide) and polyacrylamide. *J. Appl. Polym. Sci.* **100,** 3997–4003 (2006).
48. Chong, M. N., Jin, B., Chow, C. W. K. & Saint, C. Recent developments in photocatalytic water treatment technology: A review. *Water Res.* **44,** 2997–3027 (2010).
49. Glaze, W. H., Lay, Y. & Kang, J.-W. Advanced Oxidation Processes. A Kinetic Model for the Oxidation of 1,2-Dibromo-3-chloropropane in Water by the Combination of Hydrogen Peroxide and UV Radiation. *Ind. Eng. Chem. Res.* **34,** 2314–2323 (1995).
50. Gao, B., Yap, P. S., Lim, T. M. & Lim, T.-T. Adsorption-photocatalytic degradation of Acid Red 88 by supported TiO2: Effect of activated carbon support and aqueous anions. *Chem. Eng. J.* **171,** 1098–1107 (2011).
51. Tanguay, J. F., Suib, S. L. & Coughlin, R. W. Dichloromethane photodegradation using titanium catalysts. *J. Catal.* **117,** 335–347 (1989).
52. Zainal, Z. *et al.* Removal of dyes using immobilized titanium dioxide illuminated by fluorescent lamps. *J. Hazard. Mater.* **125,** 113–120 (2005).
53. Sharma, S. D., Saini, K. K., Kant, C., Sharma, C. P. & Jain, S. C. Photodegradation of dye pollutant under UV light by nano-catalyst doped titania thin films. *Appl. Catal. B Environ.* **84,** 233–240 (2008).
54. XIAO, Y., DANG, L., AN, L., BAI, S. & LEI, Z. Photocatalytic Degradation of Rhodamine B and Phenol by TiO2 Loaded on Mesoporous Graphitic Carbon. *Chin. J. Catal.* **29,** 31–36 (2008).
55. Sorolla II, M. G., Dalida, M. L., Khemthong, P. & Grisdanurak, N. Photocatalytic degradation of paraquat using nano-sized Cu-TiO2/SBA-15 under UV and visible light. *J. Environ. Sci.* **24,** 1125–1132 (2012).

56. Moctezuma, E., Leyva, E., Aguilar, C. A., Luna, R. A. & Montalvo, C. Photocatalytic degradation of paracetamol: Intermediates and total reaction mechanism. *J. Hazard. Mater.* **243,** 130–138 (2012).
57. Lin, W.-C., Yang, W.-D. & Jheng, S.-Y. Photocatalytic degradation of dyes in water using porous nanocrystalline titanium dioxide. *J. Taiwan Inst. Chem. Eng.* **43,** 269–274 (2012).
58. Rajeshwar, K. *et al.* Heterogeneous photocatalytic treatment of organic dyes in air and aqueous media. *J. Photochem. Photobiol. C Photochem. Rev.* **9,** 171–192 (2008).
59. Kwon, C. H., Shin, H., Kim, J. H., Choi, W. S. & Yoon, K. H. Degradation of methylene blue via photocatalysis of titanium dioxide. *Mater. Chem. Phys.* **86,** 78–82 (2004).
60. Chen, L. X. *et al.* Photocatalytic reduction of heavy metal ions on derivatized titanium dioxide nano-particle surface studied by XAFS. *Nucl. Instrum. Methods Phys. Res. Sect. B Beam Interact. Mater. At.* **133,** 8–14 (1997).
61. Chakrabarti, S., Chaudhuri, B., Bhattacharjee, S., Ray, A. K. & Dutta, B. K. Photo-reduction of hexavalent chromium in aqueous solution in the presence of zinc oxide as semiconductor catalyst. *Chem. Eng. J.* **153,** 86–93 (2009).
62. Ghosh-Mukerji, S., Haick, H. & Paz, Y. Controlled mass transport as a means for obtaining selective photocatalysis. *J. Photochem. Photobiol. Chem.* **160,** 77–85 (2003).
63. Kozlova, E. A. *et al.* Photocatalytic oxidation of ethanol vapors under visible light on CdS–TiO2 nanocatalyst. *J. Photochem. Photobiol. Chem.* **250,** 103–109 (2012).
64. Asahi, R., Morikawa, T., Ohwaki, T., Aoki, K. & Taga, Y. Visible-Light Photocatalysis in Nitrogen-Doped Titanium Oxides. *Science* **293,** 269–271 (2001).
65. Yu, H., Irie, H. & Hashimoto, K. Conduction Band Energy Level Control of Titanium Dioxide: Toward an Efficient Visible-Light-Sensitive Photocatalyst. *J. Am. Chem. Soc.* **132,** 6898–6899 (2010).
66. Shang, J., Yao, W., Zhu, Y. & Wu, N. Structure and photocatalytic performances of glass/SnO2/TiO2 interface composite film. *Appl. Catal. Gen.* **257,** 25–32 (2004).
67. Jaimy, K. B., Baiju, K. V., Ghosh, S. & Warrier, K. G. K. A novel approach for enhanced visible light activity in doped nanosize titanium dioxide through the excitons trapping. *J. Solid State Chem.* **186,** 149–157 (2012).

68. Li, M., Hong, Z., Fang, Y. & Huang, F. Synergistic effect of two surface complexes in enhancing visible-light photocatalytic activity of titanium dioxide. *Mater. Res. Bull.* **43,** 2179–2186
69. Stephen Davidson, R., Morrison, C. L. & Abraham, J. A comparison of the photochemical reactivity of polycrystalline (anatase), amorphous and colloidal forms of titanium dioxide. *J. Photochem.* **24,** 27–35 (1984).
70. Kong, M. *et al.* Tuning the Relative Concentration Ratio of Bulk Defects to Surface Defects in TiO2 Nanocrystals Leads to High Photocatalytic Efficiency. *J. Am. Chem. Soc.* **133,** 16414–16417 (2011).
71. He, H. *et al.* Enhanced Charge Separation in Nanostructured TiO2 Materials for Photocatalytic and Photovoltaic Applications. *Ind. Eng. Chem. Res.* (2012). at <http://pubs.acs.org.ezproxy.library.wisc.edu/doi/abs/10.1021/ie300510n>
72. Tsuchida, S., Ema, K., Sakama, H. & Kunugita, H. Trapping Dynamics of electron in TiO2 investigated by femtosecond transient absorption spectroscopy. in *Eur. Quantum Electron. Conf.* (2011). at <http://www.opticsinfobase.org.ezproxy.library.wisc.edu/abstract.cfm?URI=EQEC-2011-EG_P7>
73. Zhukov, V. P. & Chulkov, E. V. Ab initio approach to the excited electron dynamics in rutile and anatase TiO2. *J. Phys. Condens. Matter* **22,** 435802 (2010).
74. Yamada, Y. & Kanemitsu, Y. Determination of electron and hole lifetimes of rutile and anatase TiO2 single crystals. *Appl. Phys. Lett.* **101,** 133907–133907 (2012).
75. Hsiao, P.-T., Tung, Y.-L. & Teng, H. Electron Transport Patterns in TiO2 Nanocrystalline Films of Dye-Sensitized Solar Cells. *J. Phys. Chem. C* **114,** 6762–6769 (2010).
76. Mendive, C. B., Hansmann, D., Bredow, T. & Bahnemann, D. New Insights into the Mechanism of TiO2 Photocatalysis: Thermal Processes beyond the Electron–Hole Creation. *J. Phys. Chem. C* **115,** 19676–19685 (2011).
77. Katoh, R., Tamaki, Y. & Furube, A. Primary photocatalytic reactions in TiO2 nanoparticles studied by time-resolved laser spectroscopy. 81090O–81090O (2011). doi:10.1117/12.892973

78. Di Valentin, C. & Selloni, A. Bulk and Surface Polarons in photoexcited Anatase TiO2. *J. Phys. Chem. Lett.* **2,** 2223–2228 (2011).
79. Kamat, P. V. Manipulation of Charge Transfer Across Semiconductor Interface. A Criterion That Cannot Be Ignored in Photocatalyst Design. *J. Phys. Chem. Lett.* **3,** 663–672 (2012).
80. Leng, W. H., Barnes, P. R. F., Juozapavicius, M., O'Regan, B. C. & Durrant, J. R. Electron Diffusion Length in Mesoporous Nanocrystalline TiO2 Photoelectrodes during Water Oxidation. *J. Phys. Chem. Lett.* **1,** 967–972 (2010).
81. Schindler, K. M. & Kunst, M. Charge-carrier dynamics in titania powders. *J. Phys. Chem.* **94,** 8222–8226 (1990).
82. Shang, J., Zhu, T. & Xie, S.-D. Investigation on the photophysical processes in nanosized photocatalytic thin films using planar solid-state devices. *Res. Chem. Intermed.* **35,** 667–673 (2009).
83. Luna, A. J., Nascimento, C. A. O. & Chiavone-Filho, O. Photodecomposition of hydrogen peroxide in highly saline aqueous medium. *Braz. J. Chem. Eng.* **23,** 341–349 (2006).
84. Dillert, R., Bahnemann, D. & Hidaka, H. Light-induced degradation of perfluorocarboxylic acids in the presence of titanium dioxide. *Chemosphere* **67,** 785–792 (2007).
85. Tunesi, S. & Anderson, M. A. Photocatalysis of 3,4-DCB in TiO2 aqueous suspensions; effects of temperature and light intensity; CIR-FTIR interfacial analysis. *Chemosphere* **16,** 1447–1456 (1987).
86. Parvulescu, V. I. & Garcia, H. Photocatalysis in green chemistry and destruction of very toxic compounds. *Catalysis* **23,** 204–252 (2011).
87. Fu, X., Zeltner, W. A., Yang, Q. & Anderson, M. A. Catalytic Hydrolysis of Dichlorodifluoromethane (CFC-12) on Sol-Gel-Derived Titania Unmodified and Modified with H2SO4. *J. Catal.* **168,** 482–490 (1997).
88. Hwang, S.-J., Petucci, C. & Raftery, D. In Situ Solid-State NMR Studies of Trichloroethylene Photocatalysis: Formation and Characterization of Surface-Bound Intermediates. *J. Am. Chem. Soc.* **120,** 4388–4397 (1998).

89. Lopes, F. V. S. *et al.* Insights into UV-TiO2 photocatalytic degradation of PCE for air decontamination systems. *Chem. Eng. J.* **204-206,** 244–257 (2012).
90. Ma, C. M. *et al.* Effect of platinum on the photocatalytic degradation of chlorinated organic compound. *J. Environ. Sci.* **23,** 687–692 (2011).
91. Fan, J. & Yates, J. T. Mechanism of Photooxidation of Trichloroethylene on TiO2: Detection of Intermediates by Infrared Spectroscopy. *J. Am. Chem. Soc.* **118,** 4686–4692 (1996).
92. Li, X. Z., He, C., Graham, N. & Xiong, Y. Photoelectrocatalytic degradation of bisphenol A in aqueous solution using a Au–TiO2/ITO film. *J. Appl. Electrochem.* **35,** 741–750 (2005).
93. Farhadi, S., Aminzadeh, B., Torabian, A., Khatibikamal, V. & Alizadeh Fard, M. Comparison of COD removal from pharmaceutical wastewater by electrocoagulation, photoelectrocoagulation, peroxi-electrocoagulation and peroxi-photoelectrocoagulation processes. *J. Hazard. Mater.* **219–220,** 35–42 (2012).
94. Fang, T., Yang, C. & Liao, L. Photoelectrocatalytic degradation of high COD dipterex pesticide by using TiO2/Ni photo electrode. *J. Environ. Sci.* **24,** 1149–1156 (2012).
95. Miyasaka, H., Khan, S. R. & Itaya, A. Photoinduced electron transfer dynamics in aromatic vinyl polymers and related systems: time-resolved detection of primary events. *J. Photochem. Photobiol. C Photochem. Rev.* **4,** 195–214 (2003).
96. Gröllmann, U. & Schnabel, W. Free radical-induced oxidative degradation of polyacrylamide in aqueous solution. *Polym. Degrad. Stab.* **4,** 203–212 (1982).
97. Von Sonntag, C. Free-radical-induced chain scission and cross-linking of polymers in aqueous solution—an overview. *Radiat. Phys. Chem.* **67,** 353–359 (2003).
98. Da Silva Perez, D. *et al.* Photochemical bleaching of chemical pulps catalyzed by titanium dioxide. *J. Photochem. Photobiol. Chem.* **115,** 73–80 (1998).
99. Liu, Y. *et al.* Simulated-sunlight-activated photocatalysis of Methylene Blue using cerium-doped SiO2/TiO2 nanostructured fibers. *J. Environ. Sci.* **24,** 1867–1875 (2012).
100. Paschoal, F. M. M., Anderson, M. A. & Zanoni, M. V. B. Simultaneous removal of chromium and leather dye from simulated tannery effluent by photoelectrochemistry. *J. Hazard. Mater.* **166,** 531–537 (2009).

101. Guin, D., Manorama, S. V., Latha, J. N. L. & Singh, S. Photoreduction of silver on bare and colloidal TiO2 nanoparticles/nanotubes: synthesis, characterization, and tested for antibacterial outcome. *J. Phys. Chem. C* **111,** 13393–13397 (2007).
102. Wu, Q. & van de Krol, R. Selective Photoreduction of Nitric Oxide to Nitrogen by Nanostructured TiO2 Photocatalysts: Role of Oxygen Vacancies and Iron Dopant. *J. Am. Chem. Soc.* **134,** 9369–9375 (2012).
103. Grätzel, M. Dye-sensitized solar cells. *J. Photochem. Photobiol. C Photochem. Rev.* **4,** 145–153 (2003).
104. Tiwana, P., Docampo, P., Johnston, M. B., Snaith, H. J. & Herz, L. M. Electron mobility and injection dynamics in mesoporous ZnO, SnO2, and TiO2 films used in dye-sensitized solar cells. *ACS Nano* **5,** 5158–5166 (2011).
105. Zhao, Y., Li, X., Li, Q. & Deng, C. Enhancement of the Photoelectric Performance of Dye-sensitized Solar Cells by Sol-gel Modified TiO2 Films. *J. Mater. Sci. Technol.* **27,** 764–768 (2011).
106. Hernández-Alonso, M. D., Fresno, F., Suárez, S. & Coronado, J. M. Development of alternative photocatalysts to TiO2: Challenges and opportunities. *Energy Environ. Sci.* **2,** 1231–1257 (2009).
107. Fu, X., Clark, L. A., Yang, Q. & Anderson, M. A. Enhanced Photocatalytic Performance of Titania-Based Binary Metal Oxides: TiO2/SiO2 and TiO2/ZrO2. *Environ. Sci. Technol.* **30,** 647–653 (1996).
108. O'Regan, B. & Grätzel, M. A low-cost, high-efficiency solar cell based on dye-sensitized colloidal TiO2 films. *Nature* **353,** 737–740 (1991).
109. Nelson, B. P., Candal, R., Corn, R. M. & Anderson, M. A. Control of Surface and ζ Potentials on Nanoporous TiO2 Films by Potential-Determining and Specifically Adsorbed Ions. *Langmuir* **16,** 6094–6101 (2000).
110. Somorjai, G. . Atomic and molecular processes at solid surfaces. *J. Colloid Interface Sci.* **58,** 150–168 (1977).
111. Rusanov, A. I. Thermodynamics of solid surfaces. *Surf. Sci. Rep.* **23,** 173–247 (1996).
112. *Interfacial Electrochemistry*. at <http://www.springer.com/chemistry/electrochemistry/book/978-3-642-04936-1>

113. Oh, H. *et al.* Comparison of various sol–gel derived metal oxide layers for inverted organic solar cells. *Sol. Energy Mater. Sol. Cells* **95,** 2194–2199 (2011).
114. Mazali, I. O. & Alves, O. L. Characterization of nanosized TiO2 synthesized inside a porous glass–ceramic monolith by metallo-organic decomposition process. *J. Phys. Chem. Solids* **66,** 37–46 (2005).
115. TAO, J., DENG, J., DONG, X., ZHU, H. & TAO, H. Enhanced photocatalytic properties of hierarchical nanostructured TiO2 spheres synthesized with titanium powders. *Trans. Nonferrous Met. Soc. China* **22,** 2049–2056 (2012).
116. Alemany, L. ., Bañares, M. ., Pardo, E., Martín-Jiménez, F. & Blasco, J. . Morphological and Structural Characterization of a Titanium Dioxide System. *Mater. Charact.* **44,** 271–275 (2000).
117. Dai, Q., Zhang, Z., He, N., Li, P. & Yuan, C. Preparation and characterization of mesostructured titanium dioxide and its application as a photocatalyst for the wastewater treatment. *Mater. Sci. Eng. C* **8–9,** 417–423 (1999).
118. Watson, S. S., Beydoun, D., Scott, J. A. & Amal, R. The effect of preparation method on the photoactivity of crystalline titanium dioxide particles. *Chem. Eng. J.* **95,** 213–220 (2003).
119. Kääriäinen, M.-L., Kääriäinen, T. O. & Cameron, D. C. Titanium dioxide thin films, their structure and its effect on their photoactivity and photocatalytic properties. *Thin Solid Films* **517,** 6666–6670 (2009).
120. Bischoff, B. L. & Anderson, M. A. Peptization Process in the Sol-Gel Preparation of Porous Anatase (TiO2). *Chem. Mater.* **7,** 1772–1778 (1995).
121. Gordillo Delgado, F., Villa Gómez, K. & Mejía Morales, C. Titanium dioxide nanocrystalline bactericidal thin films grown by sol–gel technique. *Microelectron. J.* **39,** 1333–1335 (2008).
122. Hu, Y. & Yuan, C. Low-temperature preparation of photocatalytic thin films from anatase sols. *J. Cryst. Growth* **274,** 563–568 (2005).
123. Jung, K. Y., Park, S. B. & Anpo, M. Photoluminescence and photoactivity of titania particles prepared by the sol–gel technique: effect of calcination temperature. *J. Photochem. Photobiol. Chem.* **170,** 247–252 (2005).

124. Mechiakh, R. & Bensaha, R. Variation of the structural and optical properties of sol–gel TiO2 thin films with different treatment temperatures. *Comptes Rendus Phys.* **7,** 464–470 (2006).
125. Shi, J., Chen, S., Wang, S. & Ye, Z. Sol-Gel Preparation and Visible Light Photocatalytic Activity of Nitrogen Doped Titania. *Procedia Eng.* **27,** 564–569 (2012).
126. Dhumal, S. Y., Daulton, T. L., Jiang, J., Khomami, B. & Biswas, P. Synthesis of visible light-active nanostructured TiOx (x < 2) photocatalysts in a flame aerosol reactor. *Appl. Catal. B Environ.* **86,** 145–151 (2009).
127. Agoudjil, N. & Benkacem, T. Synthesis of porous titanium dioxide membranes. *Desalination* **206,** 531–537 (2007).
128. Heřman, D., Šícha, J. & Musil, J. Magnetron sputtering of TiOxNy films. *Vacuum* **81,** 285–290 (2006).
129. Jõks, S. *et al.* Gas-phase photocatalytic activity of nanostructured titanium dioxide from flame aerosol synthesis. *Appl. Catal. B Environ.* **111–112,** 1–9 (2012).
130. Joyce, C. D. *et al.* Synthesis and electrochemical evaluation of an amorphous titanium dioxide derived from a solid state precursor. *J. Power Sources* **195,** 2064–2068 (2010).
131. Nakaruk, A., Ragazzon, D. & Sorrell, C. C. Anatase–rutile transformation through high-temperature annealing of titania films produced by ultrasonic spray pyrolysis. *Thin Solid Films* **518,** 3735–3742 (2010).
132. Ritala, M., Leskelä, M., Nykänen, E., Soininen, P. & Niinistö, L. Growth of titanium dioxide thin films by atomic layer epitaxy. *Thin Solid Films* **225,** 288–295 (1993).
133. Wong, M.-S., Pang Chou, H. & Yang, T.-S. Reactively sputtered N-doped titanium oxide films as visible-light photocatalyst. *Thin Solid Films* **494,** 244–249 (2006).
134. Zou, J.-J., He, H., Cui, L. & Du, H.-Y. Highly efficient photocatalyst for hydrogen generation prepared by a cold plasma method. *Int. J. Hydrog. Energy* **32,** 1762–1770 (2007).
135. ZHOU, S., ZHONG, Z., FAN, Y., XU, N. & HE, Y. Effects of Sintering Atmosphere on the Microstructure and Surface Properties of Symmetric TiO2 Membranes. *Chin. J. Chem. Eng.* **17,** 739–745 (2009).

136. Karuppuchamy, S., Jeong, J.-M., Amalnerkar, D. P. & Minoura, H. Photoinduced hydrophilicity of titanium dioxide thin films prepared by cathodic electrodeposition. *Vacuum* **80,** 494–498 (2006).
137. Brownson, J. R. S., Lee, T. J. & Anderson, M. A. Surface Re-Esterification and Photo Sintering of Titania Xerogel Thin Films. *Chem. Mater.* **17,** 3025–3030 (2005).
138. Paz, Y. in *Adv. Chem. Eng.* (Hugo I. de Lasa and Benito Serrano Rosales) **Volume 36,** 289–336 (Academic Press, 2009).
139. Maleknia, S. D., Bell, T. L. & Adams, M. A. PTR-MS analysis of reference and plant-emitted volatile organic compounds. *Int. J. Mass Spectrom.* **262,** 203–210 (2007).
140. Kaneko, M. *et al.* Photoelectrochemical reaction of biomass and bio-related compounds with nanoporous TiO2 film photoanode and O2-reducing cathode. *Electrochem. Commun.* **8,** 336–340 (2006).
141. Vinodgopal, K., Hotchandani, S. & Kamat, P. V. Electrochemically assisted photocatalysis: titania particulate film electrodes for photocatalytic degradation of 4-chlorophenol. *J. Phys. Chem.* **97,** 9040–9044 (1993).
142. Kim, D. H. & Anderson, M. A. Photoelectrocatalytic degradation of formic acid using a porous titanium dioxide thin-film electrode. *Environ. Sci. Technol.* **28,** 479–483 (1994).
143. Egerton, T. A. *et al.* Photoelectrocatalysis by titanium dioxide for water treatment. *Int. J. Environ. Pollut.* **27,** 2–19 (2006).
144. Zanoni, M. V. B., Sene, J. J., Selcuk, H. & Anderson, M. A. Photoelectrocatalytic Production of Active Chlorine on Nanocrystalline Titanium Dioxide Thin-Film Electrodes. *Environ. Sci. Technol.* **38,** 3203–3208 (2004).
145. Xu, Q. & Anderson, M. A. Synthesis of porosity controlled ceramic membranes. *J. Mater. Res.* **6,** 1073–1081 (1991).
146. Candal, R. J., Zeltner, W. A. & Anderson, M. A. Titanium-supported titania photoelectrodes made by sol-gel processes. *J. Environ. Eng.* **125,** 906–912 (1999).
147. Hanaor, D. A. H. & Sorrell, C. C. Review of the anatase to rutile phase transformation. *J. Mater. Sci.* **46,** 855–874 (2011).
148. Lee, J., Park, H. & Choi, W. Selective Photocatalytic Oxidation of NH3 to N2 on Platinized TiO2 in Water. *Environ. Sci. Technol.* **36,** 5462–5468 (2002).

149. Snoeyink, V. L. & Jenkins, D. *Water chemistry*. (Wiley, 1980).
150. Wong, G. T. F. & Davidson, J. A. The fate of chlorine in sea-water. *Water Res.* **11,** 971–978 (1977).
151. Katayose, M., Yoshida, K., Achiwa, N. & Eguchi, M. Safety of electrolyzed seawater for use in aquaculture. *Aquaculture* **264,** 119–129 (2007).
152. Kraft, A. *et al.* Electrochemical water disinfection Part I: Hypochlorite production from very dilute chloride solutions. *J. Appl. Electrochem.* **29,** 859–866 (1999).
153. Jorquera, M. A., Valencia, G., Eguchi, M., Katayose, M. & Riquelme, C. Disinfection of seawater for hatchery aquaculture systems using electrolytic water treatment. *Aquaculture* **207,** 213–224 (2002).
154. Kasai, H., Yoshimizu, M. & Ezura, Y. Disinfection of water for aquaculture. *Fish. Sci.* **68,** 821–824 (2002).
155. Watanabe, K. & Yoshimizu, M. Disinfection of equipment for aquaculture by electrolyzed seawater. *Bull. Jpn. Soc. Sci. Fish.* **67,** (2001).
156. Do, J.-S., Yeh, W.-C. & Chao, I.-Y. Kinetics of the Oxidative Degradation of Formaldehyde with Electrogenerated Hypochlorite Ion. *Ind. Eng. Chem. Res.* **36,** 349–356 (1997).
157. Polcaro, A. M., Vacca, A., Mascia, M. & Ferrara, F. Product and by-product formation in electrolysis of dilute chloride solutions. *J. Appl. Electrochem.* **38,** 979–984 (2008).
158. Huntzinger, D. N. & Eatmon, T. D. A life-cycle assessment of Portland cement manufacturing: comparing the traditional process with alternative technologies. *J. Clean. Prod.* **17,** 668–675 (2009).
159. Schneider, M., Romer, M., Tschudin, M. & Bolio, H. Sustainable cement production--present and future. *Cem. Concr. Res.* **41,** 642–650 (2011).
160. Mindess, S., Young, J. F. & Darwin, D. *Concrete*. (Prentice Hall, 2002).
161. Worrell, E., Price, L., Martin, N., Hendriks, C. & Meida, L. O. Carbon dioxide emissions from the global cement industry. *Annu. Rev. Energy Environ.* **26,** 303–329 (2001).
162. Mindess, S., Young, J. F. & Darwin, D. *Concrete*. (Prentice Hall, 2002).
163. Bentz, D. P. & Stutzman, P. E. Curing, hydration, and microstructure of cement paste. *ACI Mater. J.* **103,** 348–356 (2006).

164. Nassif, H., Suksawang, N. & Mohammed, M. Effect of curing methods on early-age and drying shrinkage of high-performance concrete. *Transp. Res. Rec. J. Transp. Res. Board* **1834,** 48–58 (2003).
165. Radlinski, M., Olek, J. & Nantung, T. Effect of Mixture Composition and Initial Curing Conditions on Scaling Resistance of Ternary (OPC/FA/SF) Concrete. *J. Mater. Civ. Eng.* **20,** 668 (2008).
166. Winslow, D. N., Cohen, M. D., Bentz, D. P., Snyder, K. A. & Garboczi, E. J. Percolation and pore structure in mortars and concrete. *Cem. Concr. Res.* **24,** 25–37 (1994).
167. Vandenbossche, J. *A Review of the Curing Compounds and Application Techniques Used by the Minnesota Department of Transportation for Concrete Pavements*. 38 (Minnesota Dept. of Transportation, 1999).
168. Bennert, T., Hanson, D., Maher, A. & Vitillo, N. Influence of pavement surface type on tire/pavement generated noise. *J. Test. Eval.* **33,** 94–100 (2005).
169. Hoffmann, M. R., Martin, S. T., Choi, W. & Bahnemann, D. W. Environmental Applications of Semiconductor Photocatalysis. *Chem. Rev.* **95,** 69–96 (1995).
170. Tadmor, R., Hernandez-Zapata, E., Chen, N., Pincus, P. & Israelachvili, J. N. Debye length and double-layer forces in polyelectrolyte solutions. *Macromolecules* **35,** 2380–2388 (2002).
171. Kung, H. H. *Transition metal oxides: surface chemistry and catalysis*. (Elsevier, 1989).
172. Brownson, J. R. S., Lee, T. J. & Anderson, M. A. Surface Re-Esterification and Photo Sintering of Titania Xerogel Thin Films. *Chem. Mater.* **17,** 3025–3030 (2005).
173. Marmur, A. The lotus effect: superhydrophobicity and metastability. *Langmuir* **20,** 3517–3519 (2004).
174. Skluzacek, J. M., Isabel Tejedor, M. & Anderson, M. A. An iron-modified silica nanofiltration membrane: Effect of solution composition on salt rejection. *Microporous Mesoporous Mater.* **94,** 288–294 (2006).
175. Poznyak, S. K. *et al.* Preparation and corrosion protective properties of nanostructured titania-containing hybrid sol–gel coatings on AA2024. *Prog. Org. Coat.* **62,** 226–235 (2008).

176. Cheng-Yi, H. & Feldman, R. F. Influence of silica fume on the microstructural development in cement mortars. *Cem. Concr. Res.* **15,** 285–294 (1985).
177. Cheng-Yi, H. & Feldman, R. F. Hydration reactions in portland cement-silica fume blends. *Cem. Concr. Res.* **15,** 585–592 (1985).
178. Silica Fume In Concrete. *Silica Fume Assoc.* (2011). at <http://www.silicafume.org/general-concrete.html>
179. Andersson, K., Allard, B., Bengtsson, M. & Magnusson, B. Chemical composition of cement pore solutions. *Cem. Concr. Res.* **19,** 327–332 (1989).
180. Moon, H. Y., Shin, D. G. & Choi, D. S. Evaluation of the durability of mortar and concrete applied with inorganic coating material and surface treatment system. *Constr. Build. Mater.* **21,** 362–369 (2007).
181. Janoo, V. & Shepherd, K. Seasonal Variation of Moisture and Subsurface Layer Moduli. *Transp. Res. Rec. J. Transp. Res. Board* **1709,** 98–107 (2000).
182. Martys, N. S. & Ferraris, C. F. Capillary transport in mortars and concrete. *Cem. Concr. Res.* **27,** 747–760 (1997).
183. Shi, X. *et al.* Deicer impacts on pavement materials: Introduction and recent developments. *Open Civ. Eng. J.* **3,** 16–27 (2009).
184. Zhang, M. H., Bilodeau, A., Shen, G. & Malhotra, V. H. De-Icing Salt Scaling of Concrete Incorporating Different Types and Percentages of Fly Ashes. in **1,** (1998).
185. Cackler, E. T., Harrington, D. S. & Ferragut, T. Evaluation of US and European Concrete Pavement Noise Reduction Methods. (2006).
186. Bennert, T., Hanson, D., Maher, A. & Vitillo, N. Influence of pavement surface type on tire/pavement generated noise. *J. Test. Eval.* **33,** 94–100 (2005).
187. Stark, J. & Ludwig, H. M. Freeze-thaw and freeze-deicing salt resistance of concretes containing cement rich in granulated blast furnace slag. *ACI Mater. J.* **94,** (1997).
188. Chandler, J. W. E., Phillips, S. M., Roe, P. G. & Viner, H. E. Quieter concrete roads: construction, texture, skid resistance and noise. *TRL Rep. TRL 576* (2003).
189. Caestecker, C. Test Sections of Noiseless Cement Concrete Pavements. *Routes/Roads* **299,** 53–65 (1998).

190. Sutter, L., Dakota, S. & Institute, M. T. T. *The deleterious chemical effects of concentrated deicing solutions on portland cement concrete*. (South Dakota Dept. of Transportation, 2008).
191. LaBarca, I., Foley, R. & Cramer, S. *Effects of Ground Granulated Blast Furnace Slag in Portland Cement Concrete – Expanded Study*. 88 (Department of Civil and Environmental Engineering, 2007).
192. Dhir, R. K., Jones, M. R. & Ahmed, H. E. H. Determination of total and soluble chlorides in concrete. *Cem. Concr. Res.* **20,** 579–590 (1990).
193. He, X. & Shi, X. Chloride Permeability and Microstructure of Portland Cement Mortars Incorporating Nanomaterials. *Transp. Res. Rec. J. Transp. Res. Board* **2070,** 13–21 (2008).
194. Mangat, P. S., Khatib, J. M. & Molloy, B. T. Microstructure, chloride diffusion and reinforcement corrosion in blended cement paste and concrete. *Cem. Concr. Compos.* **16,** 73–81 (1994).
195. Stanish, K. D., Hooton, R. D. & Thomas, M. D. A. Testing the chloride penetration resistance of concrete: a literature review. *Dep Civ. Eng Univ. Tor.* (1997).
196. Chi, J. M., Huang, R. & Yang, C. C. Effects of carbonation on mechanical properties and durability of concrete using accelerated testing method. *J. Mar. Sci. Technol.* **10,** 14–20 (2002).
197. Almusallam, A. A., Khan, F. M., Dulaijan, S. U. & Al-Amoudi, O. S. B. Effectiveness of surface coatings in improving concrete durability. *Cem. Concr. Compos.* **25,** 473–481 (May).
198. Abdul Razak, H., Chai, H. K. & Wong, H. S. Near surface characteristics of concrete containing supplementary cementing materials. *Cem. Concr. Compos.* **26,** 883–889 (2004).
199. Gebler, S. H. & Klieger, P. *Effect of Fly Ash on Some of the Physical Properties of Concrete*. (1986).
200. De Gouw, J. *et al.* Sensitivity and specificity of atmospheric trace gas detection by proton-transfer-reaction mass spectrometry. *Int. J. Mass Spectrom.* **223–224,** 365–382 (2003).
201. Bowen, G. J., Ehleringer, J. R., Chesson, L. A., Stange, E. & Cerling, T. E. Stable isotope ratios of tap water in the contiguous United States. *Water Resour Res* **43,** (2007).
202. De Gouw, J. & Warneke, C. Measurements of volatile organic compounds in the earth's atmosphere using proton-transfer-reaction mass spectrometry. *Mass Spectrom. Rev.* **26,** 223–257 (2007).

203. Cappellin, L. *et al.* On Quantitative Determination of Volatile Organic Compound Concentrations Using Proton Transfer Reaction Time-of-Flight Mass Spectrometry. *Environ. Sci. Technol.* **46,** 2283–2290 (2012).
204. Hewitt, C. N., Hayward, S. & Tani, A. The application of proton transfer reaction-mass spectrometry (PTR-MS) to the monitoring and analysis of volatile organic compounds in the atmosphere. *J Env. Monit* **5,** 1–7 (2003).